University of Nottingham
UK | CHINA | MALAYSIA

Design of a multi-sensor in-situ inspection system for additive manufacturing

Andrew Dickins

Advanced Manufacturing Technology Research Group
PhD Mechanical Engineering

December 2017 – May 2022

Supervisors: Dr Simon Lawes & Prof Richard Leach

ABSTRACT

Metal powder bed fusion systems have been rapidly gaining interest from high-value manufacturing sectors, such as aerospace and biomedical, due to the unique benefits the technology can offer in terms of part design flexibility and bespoke manufacturing. In-process monitoring techniques for metal powder bed fusion have become increasingly popular as the technology continues to mature. However, adequate methods of handling data collected from the manufacturing process have yet to be explored in depth. Due to the large quantities of potential data and the temporal constraints when monitoring the PBF process, automated data interpretation is essential to allow for real time defect detection to be achieved. In this thesis, a novel measurement method for PBF systems is proposed that uses multi-view fringe projection to acquire high-resolution surface topography information of the powder bed. Measurements were made using a mock-up of a commercial powder bed fusion system to assess the system's accuracy and precision in comparison to conventional single-view fringe projection techniques for the same application. Featured based characterisation methods were applied to the measured topography to extract salient information about spatter and particles with the data being compared against a higher resolution reference measurement (focus variation). Results show that the multi-view system is more accurate, but less precise, than single view fringe projection on a point-by-point basis. The multi-view system also achieves a high degree of surface coverage by using alternate views to access areas not measured by a single camera. Measurements from the multi-view fringe projection system achieved similar reconstruction fidelity to the reference focus variation, in particular at the scales required for the largest targeted features (200 µm size and up). Topography partitioning and feature identification results achieved by feature based characterisation were comparable between fringe projection and focus variation.

Keywords:

Metrology, Fringe projection, Topography, Powder bed fusion, Feature based characterisation

ACKNOWLEDGEMENTS

I would like to acknowledge the Engineering and Physical Sciences Research Council, Centre for Doctoral Training in Ultra Precision Engineering and the Manufacturing Metrology Team for their support during my time working on this thesis. More specifically I would like to thank Simon Lawes and Richard Leach as my supervisors through the duration of this project, and my co-authors, Taufiq Widjanarko, Danny Sims-Waterhouse, Adam Thompson, Nicola Senin, Grasso, Afaf Remani, Bianca Maria Colosimo and Lewis Newton for their contributions.

I would further like to thank the lifelong friends I have made during my time working at the University of Nottingham, who have not only supported me academically and professionally, but also created an extremely pleasant environment to work in and many great memories along the way. Without them, my time working on the thesis would have been a much more stressful, and overall, less enjoyable experience.

I would also like to thank my family, who have supported and encouraged me through my entire academic career, and who without I would not be in the position I am today.

TABLE OF CONTENTS

LIST OF FIGURES

LIST OF TABLES

LIST OF ABBREVIATIONS

AM	Additive manufacturing
ASMA	Additive manufacturing surface artefact
CAD	Computer-aided design
CI	Confidence interval
CNN	Convolutional neural network
CT	Computed tomography
DSLR	Digital single-lens reflex
EB-PBF	Electron beam-powder bed fusion
ESD	Equivalent spherical diameter
FBC	Feature based characterisation
FoV	Field of view
FP	Fringe projection
fps	Frames per second
FV	Focus variation
ICP	Iterative closest point
IR	Infrared
L-PBF	Laser-powder bed fusion
MsCNN	Multi-scale convolutional neural network
mv	Multi-view
NIR	Near infrared
PBF	Power bed fusion
PCA	Principle component analysis
RoI	Region of interest
SOR	Statistical outlier removal
SVM	Support vector machine
XCT	X-ray computed tomography

1 Introduction

Additive manufacturing (AM) is defined as a "process of joining materials to make parts from 3D model data" [1]. In many additive processes, this is achieved by building horizontal layers on top of each other until the desired component is complete. The technology has attracted the attention of high value manufacturing sectors such as aerospace, automotive and biomedical, causing the industry to grow rapidly. Many advances being made across AM technologies continue to push for different materials [2], more complex geometries [3,4], reduced material waste [5], and greater financial benefit for low volume or bespoke manufacture [6,7]. The geometrical freedom permitted by AM's layer-by-layer build process [3] allows for unique features to be manufactured such as lattice structures and complex single component builds with internal features. Complex structures fabricated by AM have already been shown to provide additional functionality to parts such as integrated thermal heatsinks [8], vibration isolating lattice structures [9], and increased cellular activity for biomedical applications [10].

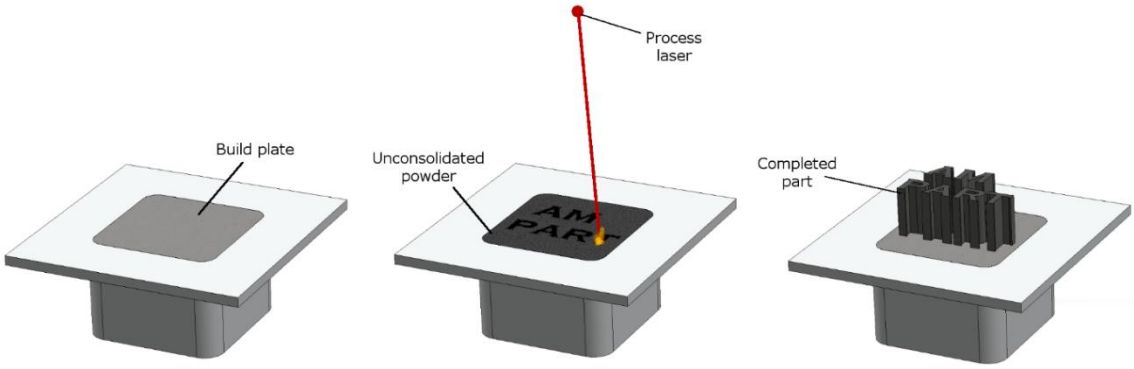

Figure 1.1.a The laser powder bed process. Starting on the left with a clear build plate before powder is spread across the build area and a high-power laser or electron beam melts selected regions into a solid component. This is repeated across many layers of powder until the desired part is complete.

Metal AM methods, such as powder bed fusion (PBF) have gained strong interest due to the ability to build parts with high-grade metals such as steels and titanium alloys. PBF processes begin with powder being introduced to the build chamber through either a feed cartridge or a powder hopper. The powder is then spread evening over the build area by a wiper blade before a high-powered beam is scanned across the surface, creating a

meltpool that fuses the powder in the desire regions of the layer. Once a layer has been completed, the build plate will be lowered and a new layer of powder is applied on top and the process is repeated (shown in Figure 1.1.a). The most common methods of PBF for metals are laser-PBF (L-PBF), which uses a scanning laser to fuse each layer, and electron beam-PBF (EB-PBF), in which an electron beam is used for fusing. Both metal PBF methods are compatible with materials that have a high melting point due to the high power the systems can deliver to the meltpool. L-PBF is typically performed in an inert gas environment [11] whereas EB-PBF is performed in vacuum. Both methods of manufacture provide a high quality of build in modern machines with comparable outcomes in terms of part properties, typically accuracies in these systems vary more significantly from manufacturer to manufacturer than between the two methods of PBF.

Although there are many benefits to metal PBF technologies, the processes are poorly understood when compared to traditional subtractive manufacturing methods, resulting in a relative lack of confidence in the quality of parts being built [12,13]. A significant cause for the lack of confidence in additive components stems from the complex phenomena present during the build process [13–16], such as the meltpool mechanics, as well as cost concerns associated with wasted time and discarded raw materials when a build process fails [13,17–19]. In an effort to improve understanding of the complex phenomena that occur during the PBF build process, many have turned to metrology solutions to analyse not only components that have been built through PBF methods, post manufacture, but also the process itself in real-time as the build is happening. Layer wise manufacturing allows new process monitoring methods to be used, capable of observing every section of the part, including internal regions, along with the machine's condition that created it. Through extensive monitoring, a greater understanding of the technology can be gained, along with implemented defect detection and closed loop monitoring systems to assess build quality in real time. Publications by Tapia and Elwany [20] and Mani et al. [21] have pointed out that there are many aspects of additive processes that are yet to be monitored and understood. Their reviews highlight the measurement needs of AM technologies to access the large amount of in-process information that could be captured through various sensors. Further studies have reviewed the literature devoted to in-situ sensing and monitoring methods [22–24], summarising and comparing various possible solutions to make sense of large amounts of data measured layer by layer. Interest

in in-process monitoring solutions for AM technologies has continued to grow as the methods gain popularity with a range of manufacturers, with various commercial tools having been made available by almost all PBF system developers, and several novel patents related to in-situ sensing, measurement and monitoring techniques being released over the last few years.

1.1 Aims and objectives

The aim of this work is to develop an in-situ monitoring system for metal PBF methods that is capable of identifying sub 500 µm defects such as elongated pores, balling [25], lattice deviations [26] over the entire powder bed area. For such a system to work, it is key that a high resolving power is achieved over a relatively large field of view (FoV) within a timely fashion to avoid significant interruption to the manufacturing process and increase production times. As such, previous research on in-situ processing techniques will be reviewed to determine what methods have proved capable, and where improvements could potentially be made. For this work to be achieved, the following objectives will be met:

- An out-of-machine prototype measurement system will be developed with the limitations of a real PBF system taken into consideration.
- Repeatability studies and measurement comparisons against a significantly higher resolution commercial system will be performed to determine the systems resolving limitations.
- A feature detection algorithm will be applied to the data to assess the feasibility of automatic detection of defects generated by the L-PBF process in real-time.

1.2 Description of work

Chapter 2 provides an overview of existing in-process monitoring methodologies that have been developed for metal AM. This review covers a wide range of monitoring methods and categorises them into types of measurement depending on what type of data is collected, and what the data can tell us about the manufacturing process. This review has been published in the journal Measurement Science and Technology [27].

Chapter 3 presents the design and development of a multi-view fringe projection (FP) system to be used as an out-of-machine prototype of an in-process AM monitoring system. An introduction to FP applications is presented, the requirements for an in-process topography measurement system is outlined, and initial data from the prototype is presented to assess the suitability of a multi-view FP system for in-process applications. Work from this chapter has been published and presented on at the conference ASPE/euspen Advancing Precision in Additive Manufacturing [28].

Chapter 4 addresses some of the issues found in the initial prototype of the multi-view FP system and hardware modifications are explained. Repeatability and uncertainty of the measurements are assessed using Additive Manufacturing Surface Artefacts (AMSA) [29] fabricated through L-PBF and EB-PBF. System resolution and limitations are discussed in the context of expected PBF surface features from the lasing process. Work from this chapter has been published in the Journal of the Optical Society of America A [30] and presented at the Solid Freeform Fabrication Symposium [31].

Chapter 5 further addresses issues with the system and some final hardware modifications. An introduction to automated defect detection in additive monitoring systems is presented, followed by findings from a feature based characterisation (FBC) algorithm that has been applied to the multi-view FP system. These findings highlight what information is present in the multi-view FP data that could potentially be automatically flagged by a defect detection system in a real manufacturing machine. Work from this chapter is currently in preparation for journal submission.

Chapter 6 outlines the current findings from the out-of-machine prototype system, the contribution of work covered in this thesis, and the future work that is require for the project to continue. Potential applications of a machine integrated version of the system are discussed, and the aims and objectives of this thesis are addressed in the context of the work done.

2 Literature review

2.1 Definitions and terminology

2.1.1 Terminology

Several terms referring to measurement and monitoring techniques are used in the literature and reviewed in this document. In some cases, there is inconsistency in the use of such terms, not only in the reviewed literature but also in different scientific fields. This section provides a glossary of terms to avoid confusion on how different measurement and monitoring methods can be classified. The most relevant terms, for which a definition is provided below, are summarised in Figure 2.1.a. The definitions that were developed during a recent roadmap exercise in the UK [32] have been adopted.

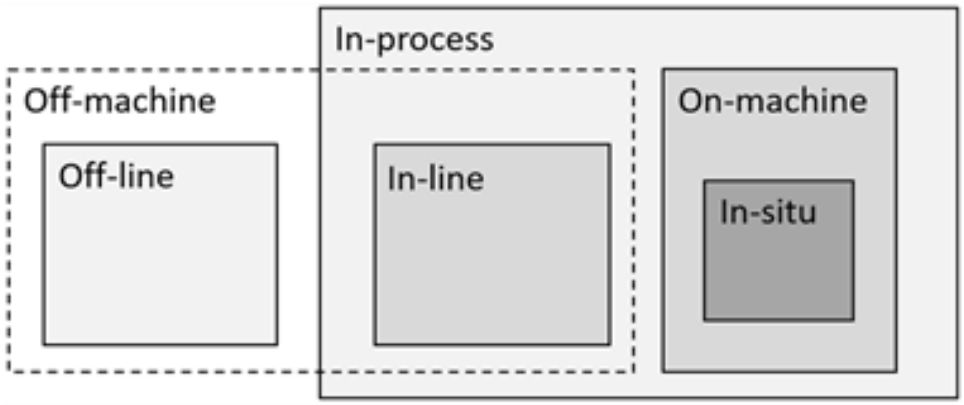

Figure 2.1.a Graphical representation of different terms associated with measurement and monitoring techniques (from Leach and Carmignato [33])

The term *"in-process*" refers to any measurement gathered during the process or between successive manufacturing steps within the same production line. In-process measurements are synchronised with the different stages of the manufacturing process so that the process can be monitored. When in-process measurements are performed right before, right after or between manufacturing stations, they are referred to as "in-line" measurements. In-line measurements are taken on separate measurement systems along the standard production line where manufacturing is not occurring. Therefore, they belong to the category of "*off-machine*" measurements, i.e., measurements carried out outside the machine where the manufacturing process occurs. When in-process measurements are performed using sensors that are installed on the machine where the

process is occurring, they are referred to as "*on-machine*" measurements. On-machine measurements that primarily record data directly from the location where the process is occurring are referred to as "*in-situ*" measurements. The term "in-situ" is the most widely used in the AM literature to indicate sensing and monitoring techniques aimed at gathering information about the process stability and the product quality while the part is being produced. Finally, when measurements are not performed in-process, they are referred to as "*off-line*". They belong to the category of off-machine measurements as they are commonly performed outside the manufacturing environment, either on a measurement station in the factory that is separate from the production line or in a laboratory.

2.1.2 Classification of measurement levels in PBF

The term "process signature" refers to one or more quantities that can be measured during the process to gather relevant information about the process stability, underlying physical phenomena and the onset of possible defects and errors [21]. In this review, the five level system of classification of of in-situ methods in adopted from Grasso et al. [27], as shown in Figure 2.1.b.

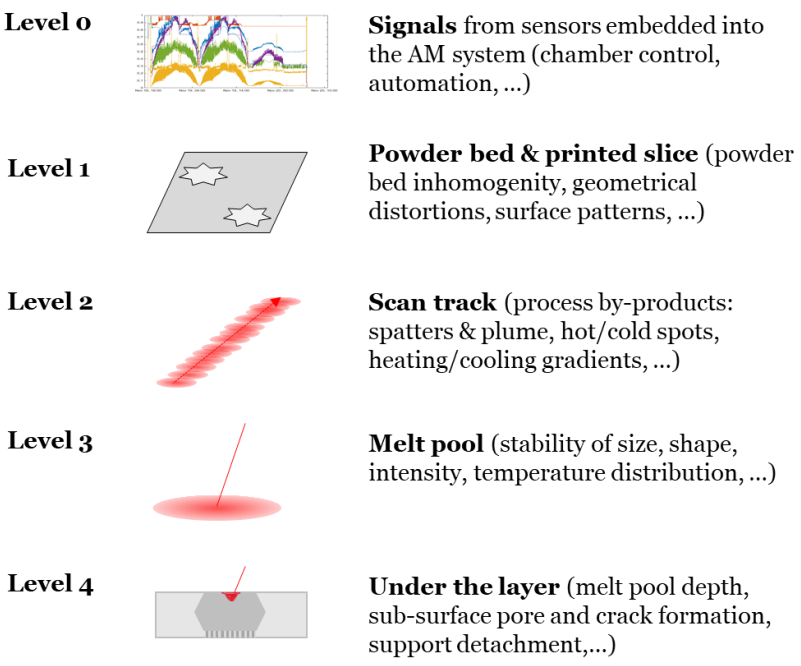

Figure 2.1.b Five in-situ measurement levels applicable to PBF processes

Level 0 involves quantities that can be measured with sensors that are already available and embedded into the PBF system, typically related to machine states and environmental conditions in the process chamber. Level 0 measurements include chamber pressure, ambient temperature and oxygen content, current and torque signals from linear axis motors, inert gas flow, build plate temperature, status of installed filters, and other parameters. Such quantities are used to guarantee a normal machine functionality and stop the process in case of unproper operating conditions, avoiding defects or faults. Level 0 methods mentioned here refer to a different perspective that allow a more advanced use of such signals to automatically detect anomalies and unstable process states that could possibly cause non-conforming part properties without activating machine state alarms.

Level 1 involves measurements gathered once (or more than once) per layer, with a field-of-view that covers the entire build area or a region of interest (RoI). Two families of process signatures can be envisaged at this level. The first involves quantities that are representative of the homogeneity of the powder bed and/or related to the presence of powder bed contaminations. The second involves both geometrical and dimensional features of the printed slice or its surface topography.

Level 2 includes quantities that can be measured with temporal resolutions considerably higher than those used in Level 1. Level 2 involves process signatures that can be measured while the laser or the electron beam is displaced within the build area to produce the current layer. This entails the capability to observe the interaction between the beam and the material, the fast cooling history of the solidified area after the beam has moved to another location and the by-products of the process, such as spatters and plume emissions.

Level 3 involves measurements of process signatures that are representative of the highest level of detail at which the PBF process can be observed in the current layer, the melt pool. The melt pool is known to be a primary feature of interest in any process that involves a beam-material interaction aimed at achieving a local fusion of the material.

Level 4 finally regards the capability of gathering information about phenomena occurring under the currently processed layer. It includes measurements that can be obtained with ad-hoc prototype machine configurations that enable transverse X-ray

imaging, but also ultrasound and acoustic emissions caused by the release of elastic energy and plastic deformations in the solidified material.

In addition to the above mentioned levels, it is possible to divide in-situ measurements into two further categories based on the location of the sensor. "*Co-axial measurement*" refers to the use of sensors that are integrated directly into the laser's optical path (a configuration that is enabled only in L-PBF), whereas "*off-axis measurement*" refers to the use of sensors that are placed outside the optical path of the beam, which is suitable in both L- and EB-PBF.

2.2 In-situ sensing and measurement methods

2.2.1 Level 0 methods – Use of embedded sensors

PBF systems require embedded sensors to keep the build chamber environment under control and to guarantee proper performance. In EB-PBF systems, some publications have suggested methods of using these embedded sensors for in-situ defect detection [34–36]. Embedded sensor signals in EB-PBF are also known as "log signals" and include column and chamber temperature and pressure signals, filament current and voltage, grid current and voltage, pulse signals representative of powder dosing, duration of each process phases, and many more. Steed et al. [35] pointed out that many of these EB-PBF log signals are correlated with process errors and variations in process conditions. They are commonly used for troubleshooting purposes in the current industrial practice. However, due to the large number of signals and their complex dependencies, both data visualisation and automated detection of out-of-control patterns need the development of novel solutions. Steed et al. [35] introduced "Falcon", a tool developed at the Oak Ridge National Laboratory for visualisation and analysis of large multivariate time series data generated by embedded sensors in EB-PBF. The tool was used in studies to investigate correlations between log signals and actual defects in parts produced via EB-PBF [37]. Chandrasekar et al. [36] showed that in-situ analysis of powder rake position and rake sensor pulse signals, used to measure when powder falls through the sensor as the powder is being spread, could provide in-depth information about the powder spreadability. The use of rake pulse sensor signals was also investigated by Grasso et al. [34], who

successfully developed a statistical process monitoring tool for automated detection of detects related to powder spreading conditions.

These seminal studies open up either to further possible solutions in the framework of in-situ process monitoring that require no additional sensors, or to new data fusion methods to take advantage of multiple signals coming from both embedded and external sensors [33].

2.2.2 Level 1 methods – Powder bed and printed slice

In-situ measurement and characterisation of layer properties has become the primary method of defect detection in PBF systems. By observing the layer, either after the recoating operation or after the melting phase, a large amount of information about process stability and part quality can be gathered. Measurements performed before laser or electron beam scanning inform about the presence of raw powder inhomogeneities, defects produced by the recoating system (rippling, bouncing effects, etc.) and the presence of so-called super-elevated edges that may not be fully covered by the new powder layer. Measurements performed after scanning, instead, enable the characterisation of the printed slice as well as the powder bed contamination caused by the beam-material interaction and process by-products.

As far as the analysis of the printed slice is concerned, two major streams of research can be identified. One regards the characterisation and detection of out-of-plane irregularities in the printed area and its surface topography. Irregular surface patterns may produce local regions of varying powder thickness, which may result in a varying energy density provided to the material by the beam. Surface irregularities may also interfere with the recoating operation, generating a propagation of defects within the build area. The other stream of research regards the reconstruction of the contours of the printed area to identify geometrical and dimensional deviations from the nominal shape, together with irregularities in the slice contours. In this case, the goal is to detect major deviations from the expected shape, as they can be representative of defects that are difficult or impossible to recover in post-processing steps.

Table 1 In-situ measurement performances for level 1 methods (includes only references where resolution values were specified).

Sensing method	Process	Spatial (lateral) resolution µm/pixel	Vertical resolution µm/pixel	References
Off-axis imaging in visible range	L-PBF	7	NA	Aminzadeh and Kurfess, 2019 [38]
		10 - 13		Lu et al., 2020 [39]
		20		Caltanisseta et al., 2018 [40]
		24		Kleszcynski et al., 2012 [41], Jacobsmulhen et al., 2013 [42] & 2015 [43]
		20 - 30		Zur Jacobsmulhen et al., 2019 [7]
		15 - 50		Foster et al., 2015 [45]
		50		Gobert et al., 2018 [46]
		45 – 88		Abdelrahman et al., 2017 [47]
		125		Pagani et al., 2020 [48]
		20 - 290		Scime et al., 2020 [49]
		290		Scime and Beuth, 2018 [50,51]
Off-axis NIR/IR imaging	L-PBF	25	NA	Mahmoudi et al., 2019 [52]
		100		Bamberg et al., 2016 [53]
		830		Schwerdtfeger et al., 2012 [54]
	EB-PBF	100		Yoder et al., 2018 [37] & 2019 [55], Nandwana et al., 2018 [56]
		170		Ridwan et al., 2014 [57]
		350		Rodriguez et al., 2012 [58]
Fringe projection	L-PBF	6.8	-	Zhang et al., 2016 [59,60], Land et al., 2015 [61]
		60	-	Zhang et al., 2015 [62]
		100	<10	Kalms et al., 2019 [63]
	EB-PBF		<20	Liu et al., 2019 [64] & 2020 [65]
Blade mounted sensor	L-PBF	5.3	NA	Phuc and Seita, 2019 [66]
		20	-	Barrett et al., 2018 [67]
Inline coherent imaging	L-PBF	30	7	Fleming et al., 2020 [68]
		100	25	Depond et al., 2018 [69]
Electronic imaging	EB-PBF	33.33	NA	Wong et al., 2020[70]
		320 – 358		Wong et al., 2019 [71,72]
		60		Arnold et al., 2018 [73] & 2019[74]
		50 - 100		Pobel et al., 2019 [75]

Level 1 methods include a variety of sensing techniques, which produce different data formats and lead to different measurement performances and capabilities. They can be divided into the following major categories: off-axis mounted cameras in the visible or infrared (IR)/near IR (NIR) range, FP combined with single or stereo cameras, blade-mounted sensors, in-line coherent imaging and electronic imaging (suitable in EB-PBF only). It is worth noting that in most reviewed studies, the term "spatial resolution" is commonly used in place of "instantaneous field of view", whereas the true spatial resolution depends on the inherent optical blur [76]. Going forward in this chapter, the term "spatial resolution" will be used to indicate the width of an individual pixel on the measurement surface. A summary of Level 1 methods and the reported resolutions is provided in Table 1.

2.2.2.1 Off-axis imaging in the visible range

Powder bed cameras are already available in most L-PBF systems, hence the development of camera based in-situ measurement and monitoring methods has become commonplace due to few, or no, modifications being require. Seminal works demonstrated the feasibility of layerwise imaging techniques for the detection of powder bed irregularities [41,43,45,77] and powder bed monitoring algorithms have already been implemented by L-PBF system developers (a summary of commercial monitoring toolkits is reported in Colosimo and Grasso [33]).

The capability to detect local inhomogeneity in the powder bed and/or irregular surface patterns requires a machine vision setup involving a sufficient spatial resolution and appropriate lighting conditions. The importance of lighting conditions has been pointed out by different authors, and different approaches have been used both in research studies and in industrial implementations [41,43,45,47]. Caltanissetta et al. [40] and Gobert et al. [46] investigated and compared different illumination sources, showing that significantly different layerwise image processing performances could be achieved by varying the lighting conditions. Figure 2.2.a shows examples of layerwise images with different lighting conditions Gobert et al. [46].

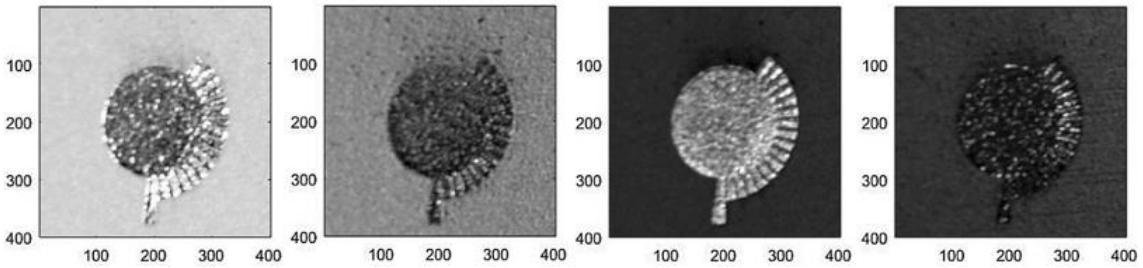

Figure 2.2.a In-situ powder bed images using different single lighting conditions, adapted from Gobert et al. [46].

In most studies, high spatial resolution cameras where installed on L-PBF machines available viewports, but in a few cases, powder bed cameras and illumination conditions already available in industrial systems were used, without any modification of the original setup [48,49]. Recent studies focused on the automated extraction of features from powder bed images for the classification of irregularities within both loose powder regions and previously melted areas [38,39,46,50]. The generation of layerwise image datasets comprising both regular and irregular powder bed surfaces was needed in most studies [38,78]. Registration between in-situ gathered images and the nominal shape of the printed slice from the sliced STL model of the part was used by different authors to identify and isolate the melted region from the surrounding loose powder [79,80]. Despite being a relatively mature solution in L-PBF, powder bed homogeneity monitoring via off-axis optical imaging has been investigated in only one study in EB-PBF [81]. The high temperature differences within the powder bed in EB-PBF after powder recoating, and the difficulty to install additional sensors on EB-PBF machines, makes this kind of in-situ monitoring more challenging than in L-PBF.

Layerwise optical imaging allows not only the identification of possible surface irregularities, but also the reconstruction of slice geometry. Aminzadeh and Kurfess [38] investigated the accuracy of in-situ image segmentations by comparing the identified contours with manual segmentation applied to the same images. A different approach was proposed by Caltanissetta et al. [40] who first compared different active contour segmentation methods under different lighting conditions, then investigated the sources of variability of in-situ measurements in terms of repeatability, part-to-part and build-to-build variability. Caltanissetta et al. [40] showed that, by combining appropriate image pre-processing and segmentation algorithms with suitable lighting configurations,

sufficient measurement accuracy and repeatability to detect major geometric deviations could be achieved. Pagani et al. [48] extended the study of Caltanissetta et al. [40] by presenting a tuned image segmentation approach that is robust to non-optimal illumination conditions. Other methods for in-situ slice contour detection have been proposed by Gaikwad et al. [82], He et al. [83] and zur Jacobsmuhlen et al. [44].

2.2.2.2 Off-axis imaging in the NIR/IR range

In L-PBF, some authors have used NIR layerwise imaging for surface pattern analysis. Bamberg et al. [53] presented a method called "optical tomography", currently implemented by EOS in the EOSTATE monitoring toolkit. The surface pattern of the printed area was reconstructed by translating off-axis NIR video frames, acquired during the the melting phase, into a layerwise image. A NIR filter was used to block the reflections of the laser beam and the emissions from ionised gases. Mahmoudi et al. [52] generated layerwise images by combining thermal images of the melt pool acquired via a co-axial two-wavelength thermal camera with a spatial resolution of 25 μm/pixel.

Layerwise NIR and IR imaging have been more commonly used in EB-PBF. In the seminal works of Schwerdtfeger et al. [54], Rodriguez et al. [58], Ridwan et al. [57] and Mireles et al. [84], layerwise IR vision was used to characterise the surface pattern of printed areas to detect flaws and surface anomalies. More recently, Yoder et al. [37,55] and Nandwana et al. [56] used a layerwise imaging system called "LayerQam", developed by Arcam for integration in its EB-PBF machines. The system consists of a NIR camera that acquires an image of the layer after the melting phase. Local pixel intensity variations and the presence of bright spots were used as proxies of possible volumetric flaws and material discontinuities in studies that correlated in-situ and ex-situ inspection results. Figure 2.2.b shows an example of layerwise patterns reconstructured via the optical tomography method discussed by Bamberg et al. [53].

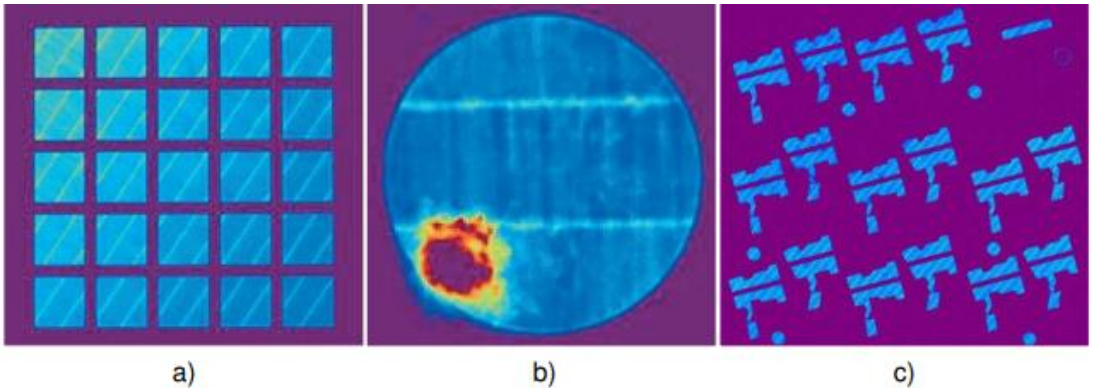

Figure 2.2.b Examples of optical tomography images for cubic samples with variation of energy density (a), a cylinder produced under shielding gas flow variation (b) and defect-free complex shapes [53].

2.2.2.3 Fringe projection

Off-axis imaging methods previously discussed are suitable to provide a 2D reconstruction of the powder bed and the printed slice. Local pixel intensity variations represent the only suitable driver to determine possible surface irregularities. Other methods have been applied in PBF processes to obtain a 3D reconstruction of the height map of the powder bed. One technique proposed by different authors is FP, which enables a combination of layer imaging and topographical analysis. The technique requires one or multiple cameras and a projector: various configurations have been proposed in the literature, mainly for L-PBF.

The simplest configuration uses a single camera. With this approach, Zhang et al. [60] upgraded a method previously presented by the same authors [59,61], demonstrating the possibility to achieve a lateral resolution of 6.8 μm/pixel over a limited FoV of (28 × 15) mm. The vertical resolution was quantified in terms of a single point repeatability equal to 0.47 μm. Land et al. [61] pointed out that the most important factors in determining the resolution of the height map are the spatial frequency of the projected fringes onto the build plane (that depends on the pixel density of the projector) and the geometric arrangement of the imaging hardware, which, in L-PBF applications, is constrained by the chamber size and the location of available viewports. Other authors proposed and tested multi-view configurations, with two cameras, suitable to achieve higher resolution and accuracy [63] and an example of surface reconstruction based on these methods is shown in Figure 2.2.c.

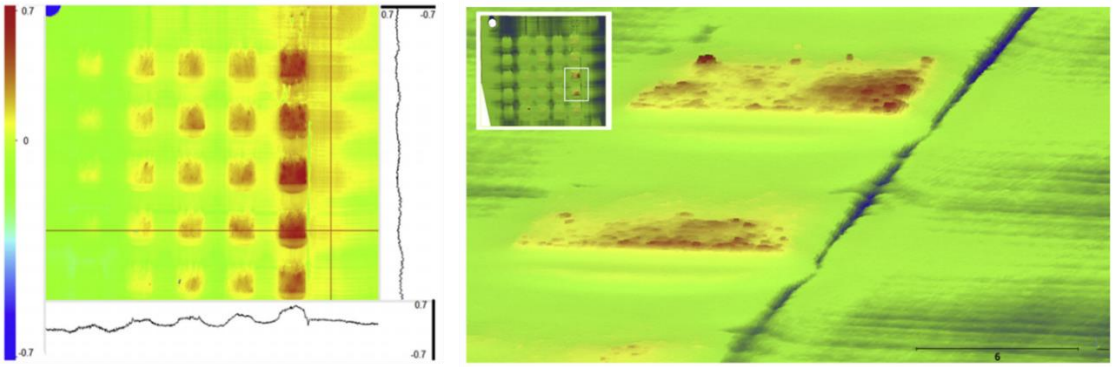

Figure 2.2.c Example of height map and height surface profiles gathered through a multi-view FP approach (values in millimeters, FoV of (150 × 150) mm)[63].

The use of FP in EB-PBF was investigated by Liu et al. [64,65] and used on commercial machines from Weyland Precision. The FP measurements were taken during the time window between powder recoating and fusion and after EB melting. The proposed system was a single-view system including a (3016 × 4016) pixels CCD camera and a DLP projector installed on a commercial EB-PBF machine. Liu et al. [65] reported a vertical resolution below 20 μm with a maximum repeatability of 6.8 μm and a measurement accuracy of 15.8 μm enabled by a dedicated calibration approach.

2.2.2.4 Blade mounted sensors

A few authors explored the idea of using sensors mounted on the recoater to gather a full-field and high spatial resolution 2D scan of the powder bed surface. Tan Phuc and Seita [66] installed a linear optical sensor on the recoater and equipped the L-PBF system with a microcontroller to synchronise the recoater speed with the image acquisition. With an optical resolution of 4800 dots-per-inch over a length of 210 mm, a spatial resolution of 5.3 μm/pixel was achieved. The line-scanning approach avoids any perspective distortions and issues related to non-homogeneous illumination conditions within the build area. Tan Phuc and Seita [66] showed that their proposed approach could be used not only for 2D surface pattern characterisation of the entire powder bed, but also to detect irregularities along the vertical direction. Due to the small depth-of-field of the linear sensors, super-elevated edges and variations in the powder layer thickness were shown to fall out of the focal plane, resulting in "blurred" areas in the acquired images. By locally mapping the focus levels across the entire scan, it could be possible to detect local height variations. Figure 2.2.d shows an example of a powder bed image obtained with the line-

scanning methods presented by Tan Phuc and Seita [66] and the corresponding estimate of the height map.

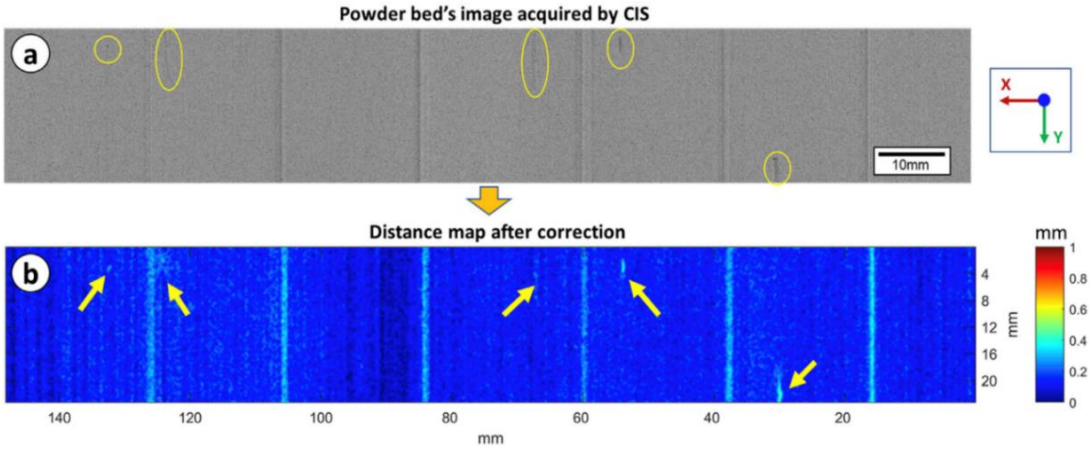

Figure 2.2.d Example of high spatial resolution powder bed line-scan optical imaging (top) and corresponding reconstruction of irregularities based on focus level mapping (b) [66].

In a previous work, Barrett et al. [67] mounted a high-resolution laser triangulation line-scan system on the recoater arm of an L-PBF machine to perform surface mapping of the powder bed before and after the melting phase. A similar concept was first proposed by Erler et al. [85]. The advantage of this approach, compared to that presented by Tan Phuc and Seita [66], is the effective capability of reconstructing the powder bed topography via a height map. However, the obtained lateral resolution was lower than that reported by Tan Phuc and Seita [66] (the commercial triangulation system used by Barrett et al. [67] was characterised by a profile data interval of 20 μm and the laser scanner spans only a small fraction of the powder bed along a 15 mm scan width).

2.2.2.5 In-line coherent imaging

Rather than using an optical point or line triangulation instrument, some authors proposed a technique known as low-coherence interferometry or in-line coherent imaging, where the L-PBF laser beam itself is used, at the end of the melting phase to reconstruct the surface topography of the layer [68,69,86]. This approach exploits a co-axial sensing configuration to collect local height measurements by raster scanning the area with an imaging beam, collecting the backscattered radiation and interfering it with a reference beam. The imaging beam is directed through the same lens used for the processing beam, which prevents the need for perspective corrections [68]. The seminal work of Neef et al.

[86] demonstrated the feasibility of the method. The powder bed surface was exposed to a broadband light source integrated into the sensor within a (3 × 3) mm area. The RoI was raster scanned at nearly constant speed, with pulses generated at defined pixel positions to trigger the optical sensor. With such a high lateral resolution, the resulting height map could be used to detect single powder particles and defects of lateral size lower than 50 μm.

Two more recent studies further investigated the potential of this approach. Fleming et al. [68] used a sensing apparatus enabling a vertical resolution of 7 μm and a lateral resolution of 30 μm, with a sampling frequency of 50 kHz. Fleming et al. [68] also proposed a method to combine the in-line coherent imaging measurement with an in-situ surface topography correction method that exploits the same L-PBF laser for ablation of the layer surface. In Depond et al. [69], measurements were gathered at a sampling rate of 100 kHz, capturing the surface topography of a (44 × 44) mm square region with a lateral resolution of 100 μm and a vertical resolution of 25 μm. The vertical resolution is theoretically limited by the coherence length of the light source (with the setup used by Depond et al. [69], the theoretical limit was about 5 μm). The lateral resolution is limited by the beam diameter and the sampling strategy along the raster scanning direction. This method also requires a raster scan of the area after the melting phase, increasing the overall build time. Figure 2.2.e shows an example of in-situ topography reconstruction via in-line coherence imaging from Neef et al. [86].

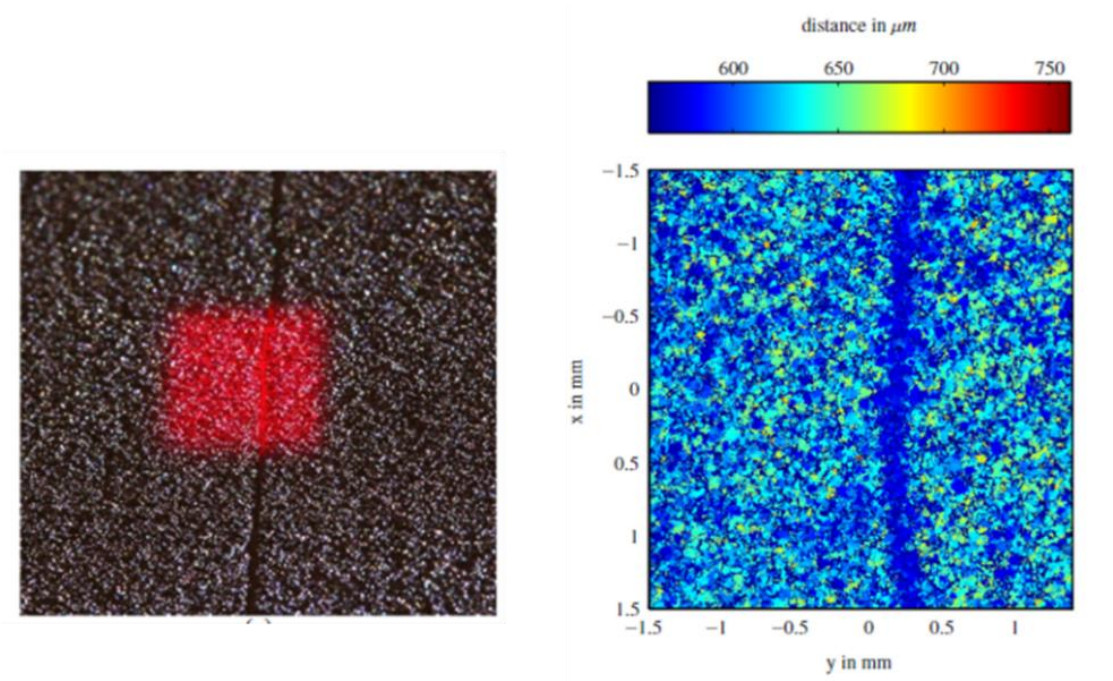

Figure 2.2.e RoI covered by the inline coherent imaging (left) and corresponding in-situ topography reconstruction (right) [86]

2.2.2.6 Electronic imaging

In EB-PBF the electrons produced as by-products of the beam-material interaction can be used to generate an electronic image of the layer. This idea has been explored and tested by various researchers. Wong et al. [71] presented a pilot study involving an in-house developed electronic imager comprising an electron detector, a differential signal amplifier, a data logger and software for image generation. The system was installed on an Arcam A1 machine. The electron beam was used to scan the layers and metal surfaces while the heat shield was used as an electron collector. A raw image was produced, where each pixel value was proportional to the signal strength of backscattered and secondary electrons. In following work, the same researchers [72] investigated the spatial resolution enabled by electronic imaging. They reported a spatial resolution of 320 μm/pixel to 358 μm/pixel with a FoV of (180 × 180) mm or (60 × 60) mm, respectively. In a more recent work, the same authors showed the layerwise generation of bitmap images of the printed areas, for comparison against the nominal shape from the sliced CAD model [87] and investigated the possibility of detecting different materials within the build area [70].

Arnold et al. [74] used the same approach, but only using backscattered electrons, and installed a circular backscattered electron detector above the build chamber of an Arcam S12 machine. Arnold et al. [74] demonstrated that this configuration enabled a much higher spatial resolution (60 µm/pixel). In this study, and in all previously mentioned studies, the electronic image was generated at the end of the melting phase by performing a raster scan of the entire build area with the electron beam. Arnold et al. [74] demonstrated, instead, that the same image could be generated during the melting phase. Along the direction orthogonal to the scan tracks, the resulting image resolution was equivalent to the hatch spacing (between 50 µm/pixel and 100 µm/pixel in the published work). Along the scan direction, the resolution was limited by the scan speed and the sampling rate of the measurement system, and was significantly higher than that in the other direction. In order to get square-shaped pixels, the data was downsampled to the lowest resolution. Figure 2.2.f shows some examples of electronic images in EB-PBF from Wong et al. [71] and Arnold et al. [74].

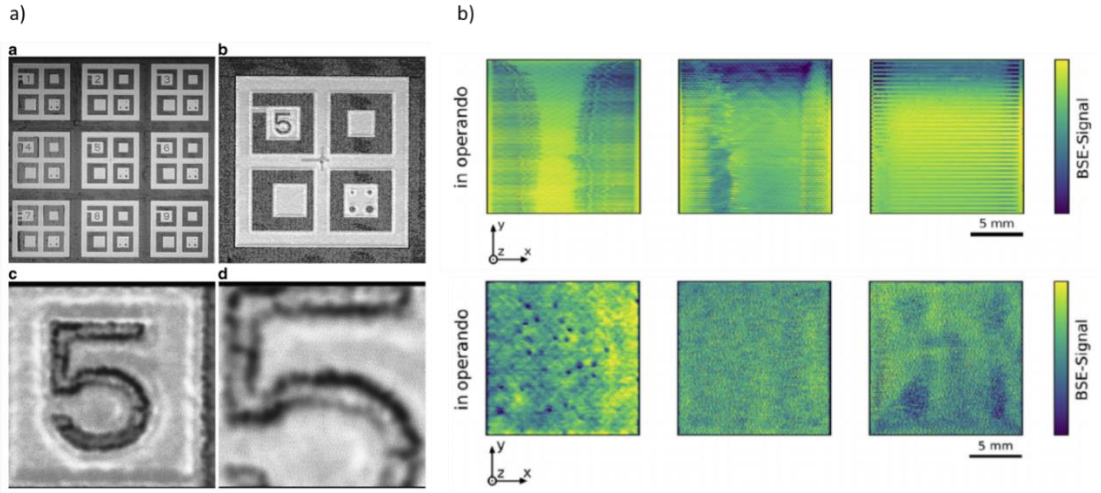

Figure 2.2.f Examples of electronic images in EB-PBF: a) images with different magnification factors from Wong et al. [71], b) images of squared printed areas generated via in-operando backscattered signal acquisition from Arnold et al. [74] for different materials (top panels: X15CrNiSi20-12, bottom panels: Ti6Al4V) with hatch spacing increasing from left to right (50 µm, 100 µm, 200 µm).

2.2.3 Level 2 methods – Scan track

In-situ process monitoring at track level involves in-process measurements of fast transient phenomena and high-speed emissions during laser or electron beam scanning.

Studies in the literature can be divided into two major streams of research. The first regards measurements related to the local or global cooling history of the slice, either for the characterisation of spatio-temporal thermal gradients in each slice or for the detection of anomalous heat exchanges and cooling patterns. The second research stream involves the in-process measurement of quantities related to the by-products of the L-PBF process such as spatters and plume emissions. The aim is either to understand underlying physical phenomena through the study of process by-products or to detect unstable process conditions and improper energy inputs.

A third field of research in L-PBF is the in-situ measurement of acoustic emissions associated with air density variations caused by plasma formation and plume emissions during the laser scanning of the part. According to the nomenclature commonly used in laser welding [88], these acoustic emissions are called air-borne emissions and can be captured by microphones or other sensors in the vicinity of the melting area. These acoustic emissions are different from the so-called structure-borne emissions, which require contact sensors.

Level 2 monitoring methods involve off-axis mounted sensors, mainly cameras in the visible range or thermal cameras. Unlike in level 1 methods, high temporal resolution is needed to capture fast and transient phenomena, whereas high spatial resolution is needed to characterise the spatial features of interest extracted from video or image data in terms of location, size, area and other relevant properties.

2.2.3.1 Measurement of process heatmap and heating/cooling profiles

AM allows the "seeing" of the thermal history of the process, in time and in space. Almost all major quality characteristics of the final part and its mechanical performance depend on the thermal history [89]. Local and global variations of heating and cooling patterns may indicate either a lack of fusion or excessive heat accumulation with resultant effects on material solidification at volumetric, microstructural and geometrical levels.

Looking at adopted temporal resolutions, it is possible to distinguish between two major streams of research. One aimed at reconstructing a heatmap of the layer combining information gathered at low speed (up to 50 frames per second (fps)), while another aimed at capturing fast heating and cooling transients, with temporal resolutions from 300 fps

to more than 10000 fps. In terms of spatial resolution, it is also possible to identify two major categories of measurement approaches. In-situ measurement setups with a FoV limited to a small portion of the build area enable resolutions in the range 8 µm/pixel to 100 µm/pixel, whereas with using a FoV covering the entire build area enables lower spatial resolutions, typically above 100 µm/pixel.

Thermal cameras have been used in both L-PBF and EB-PBF in either the short wave IR (~0.9 µm to 2.5 µm), medium wave IR (2 µm to 5 µm) or long wave IR range (7.5 µm to 14 µm or more). In L-PBF, Montazeri and Rao [90], Gaikwad et al. [91] and Heigel et al. [92,93] used short wave IR video imaging to capture thermal signature variations throughout the build of overhang features and bridges. The choice of a narrow short wave IR bandwidth (from 1.35 µm to 1.6 µm) was motivated by Heigel et al. [92,93] to filter out the laser wavelength and to minimise possible temperature measurement errors related to wavelength-dependent emissivity values. Short wave IR video imaging was used by Lough et al. [94,95] differently. Lough et al. used features extracted from the thermal map to generate a voxel-based representation of the part, to be correlated with its local and global quality characteristics. Lane et al [76] used a MWIR camera with a short wavelength filter to reduce the temperature measurement uncertainty due to inaccurate emissivity estimations, since this uncertainty can be reduced at short wavelengths.

Despite their higher sensitivity to emissivity values for absolute temperature estimation, thermal cameras operating in the medium or long wave IR range can be calibrated in a wider temperature interval than that of short wave IR cameras, with high sensitivity even at high temperatures. This makes them the most utilised sensors for in-situ thermal video imaging applications in both L-PBF and EB-PBF.

In some cases, thermal maps of the layer were generated by selecting frames acquired during different phases of the process [96,97] or by averaging video frames [98]. Whereas most studies focused on the analysis of the thermal map of each layer, Williams et al. [89] focused on the temperature evolution along the build, analysing the impact of the inter-layer cooling time on the final quality and mechanical properties of the parts. They showed that the number of parts in the build and the way in which they are spatially located have a significant effect on the quality of the manufactured part because of its thermal history.

Other authors used high temporal resolution IR video imaging in L-PBF to enhance the reconstructing of temperature profiles in space and time, additionally capturing transient and fast phenomena. Foster et al. [99] used high-speed IR videos to estimate local peak IR intensities within the scanned areas and correlate their maximum value with different processing parameters. Mohr et al. [100] applied a feature extraction approach to high-speed thermographic data to determine the time that a surface element was at an apparent temperature above a certain threshold, also called "time over threshold"; the same indicator was used by Paulson et al. [101]. An image from the study presented by Paulson et al. [101] and the local estimation of the time over threshold indicator is shown in Figure 2.2.g. Mohr et al. [100] also showed that combining synchronous video imaging at high spatial resolution (NIR camera) and high temporal resolution (medium wave IR camera) increased the capability of detecting volumetric defects compared to imaging with a single sensor.

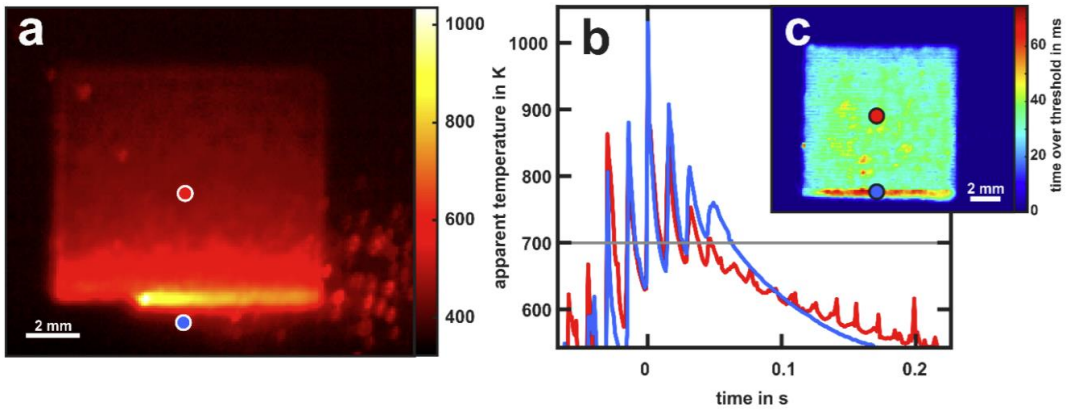

Figure 2.2.g An example of in-situ reconstruction of local cooling profiles via high-speed IR video imaging and the "time over threshold" index computation by Paulson et al. [101].

In EB-PBF, in-situ video imaging methods need to be adapted to face specific characteristics of the process. Both conventional and thermal cameras need to be protected from X-ray emissions and metallisation. Available viewports can be equipped with leaded glass and a rolling Kapton film to prevent metal vapour from adhering to the window. The Kapton film has an IR transmission of about 79%, whereas a 10 mm thick leaded glass window has an IR transmission of 1.08% [102]. However, due to the high temperatures involved in the process, detailed IR images were captured despite such reduced transmission. Other researchers [103] used a mechanical shutter to protect the

viewport from metallisation, enabling image acquisition within a brief interval only. After the seminal studies that investigated the use of IR video imaging in EB-PBF [84,103], in-situ thermography was further used by Cordero et al. [104], Raplee et al. [105] and following studies by the same researchers [106].

Although IR cameras enable measurements of thermal gradients in space and time, the estimation of absolute temperatures is difficult to achieve. PBF processes involve fast phase transitions from powder to liquid then to solidified material, in addition to continuous changes in surface properties and emissions of the vapourised material, which limit the feasibility of accurately estimating the emissivity needed to convert raw signals into temperature values. In several in-situ monitoring applications, the variation of the thermal signature over time is more relevant than the estimation of the absolute temperature. In those cases, data processing and monitoring algorithms can be directly applied on raw signals, i.e., measured radiance values in arbitrary units. When accurate estimates of the true temperature are needed, different methods can be used. A simple but less accurate approach used by some authors [107] consists of selecting the emissivity value to set the temperature measured within the melt-pool region at the known liquid–solid transition temperature of the material. Other studies described calibration procedures using heated calibration artefacts, which enable more accurate estimates. These include the methods presented by Williams et. [89], Dinwiddie et al. [102] and Rodriguez et al. [103].

The calibration procedure described by Williams et al. [89] was applied in L-PBF. A calibration component was manufactured using the same L-PBF machine, process parameters and material used in the in-situ measurement study. The calibration component included a cartridge heater at the bottom and a K-type thermo-couple at the top surface and was placed in the chamber and heated in an inert atmosphere. The surface temperature was measured by means of both the thermal camera (mounted in the same configuration used for in-situ measurements) and the thermo-couple during both heating and cooling, to check for any hysteresis in camera intensity due to oxidation. The same calibration was repeated by covering the calibration surface with powder, leading to two distinct calibration curves, one for solidified material and one for loose powder.

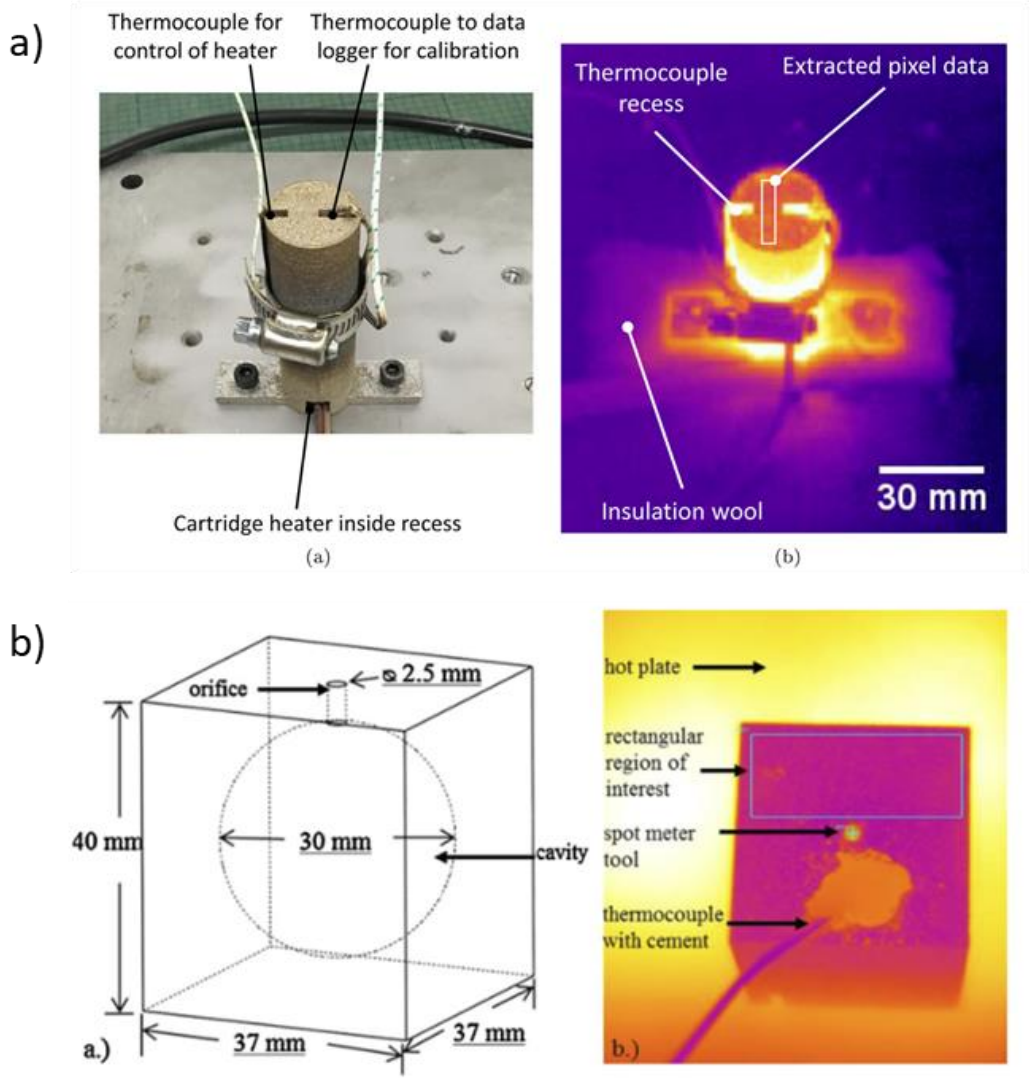

Figure 2.2.h Examples of calibration components used in L-PBF (top panel) [89] and in EB-PBF (bottom panel) [103] to enable true temperature estimation via in-situ IR video imaging.

Similar calibration procedures in EB-PBF were presented by Dinwiddie et al. [102] and used in following studies (Raplee et al., [105] and Rodriguez et al. [103]). In this case, the electron beam itself was used to preheat the calibration sample instead of using embedded heaters. Figure 2.2.h shows the calibration components used by Williams et al. [89] in L-PBF (a) and the one used by Rodriguez et al. [103] in EB-PBF (b).

Thermal cameras are large in size, expensive and typically require a modification of the machine hardware and viewports for installation on industrial systems. Conventional cameras are much cheaper and easier to integrate than thermal cameras, and high temporal

resolution can be made available with compact equipment. Although they do not allow actual temperature measurements, pixel intensity gradients in the visible range can be used as proxies for actual thermal gradients to identify anomalies and defects in some applications. In this framework, some studies focused on the detection of local over-heating phenomena known as "hot-spots" via high-speed video imaging in the visible range [24,108,109]. A hot-spot is a local over-heating of the layer caused by out-of-control heat exchanges with the surrounding material. A region affected by a hot-spot stays hot (bright) for a longer time with a slower cooling drift than in normal conditions. Because of this, a conventional camera with sufficient temporal resolution is suitable to capture the anomaly. High-speed vision in the visible range was also used in EB-PBF for hot-spot detection [81] and to support the development of a novel scan strategy that splits the melting beam, referred to as "ghost beam", by monitoring the dynamics of the meltpool [110].

As a compromise between standard optical systems and thermal cameras, video-imaging in the NIR range (0.7 µm to ~1 µm) has been used by various researchers [107,111–114]. The main advantage is to filter out some deleterious effects at specific wavelengths and to reduce the dynamic range of the measurement with respect to that of optical video imaging, since a narrower spectral band mitigates pixel saturation in the presence of large temperature variations. NIR video imaging for level 2 in-situ measurements has been used mainly in EB-PBF. The leaded glass used to shield X-ray emissions has a transmission larger than 90% in the NIR range, much higher than in the IR range [112].

2.2.3.2 Measurement of process by-products

Due to the different beam-material interactions in L-PBF and EB-PBF, different kinds of by-products are generated in the two processes. In L-PBF, a large quantity of spatters is ejected together with partial material vaporisation, also known as plume. The number of publications devoted to the in-situ measurement of process by-products in L-PBF has considerably increased in the last few years, as various researchers demonstrated the correlation between the information enclosed by such by-products and the process states that can have detrimental effects on part quality. Different by-products are generated in EB-PBF, including secondary and backscattered electrons and X-rays, but they are more appropriate for level 1 in-situ measurements rather than for capturing fast transient

phenomena during the electron beam scanning of the part. Therefore, this Section is devoted to methods applied to L-PBF only.

Large numbers of process by-products can partially deflect and absorb the laser beam energy, or even deviate the laser focus position, leading to a modification in the laser beam geometry and the energy input. Spatter deposited on the powder bed may also produce contaminations in the part and discontinuities in the powder bed [115]. Unstable and out-of-control process by-product generation may have a detrimental effect on material properties. Figure 2.2.i depicts the plume emission and spatter ejection mechanisms in L-PBF, including droplet and hot powder spatters. The schematic example in Figure 2.2.i shows a forward plume emission, but, as shown by Bidare et al. [116], upwards and backwards plume emissions may occur, depending on process parameters, with different effects on powder bed denudation and spatter ejection.

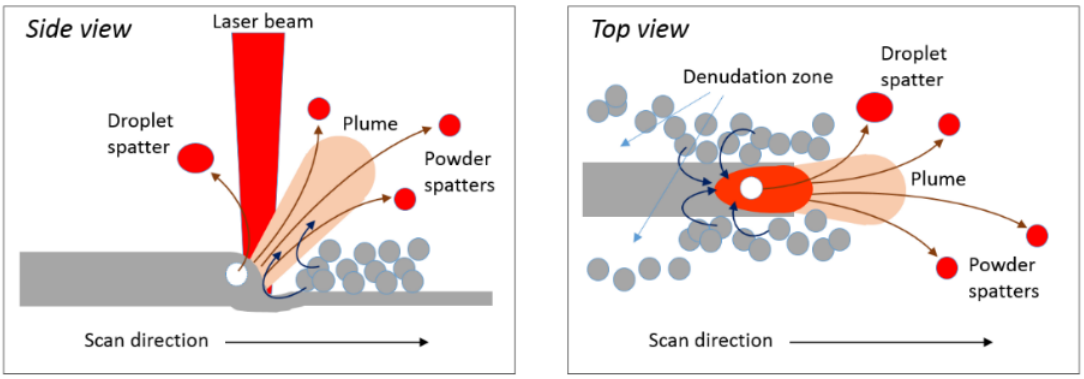

Figure 2.2.i Schematic representation of spatters and plume emissions in L-PBF.

Various studies in the literature demonstrated the possibility to gather information about spatter and plume salient properties via visible and IR video imaging methods. Figure 2.2.j shows some examples from the in-situ measurement of process by-products.

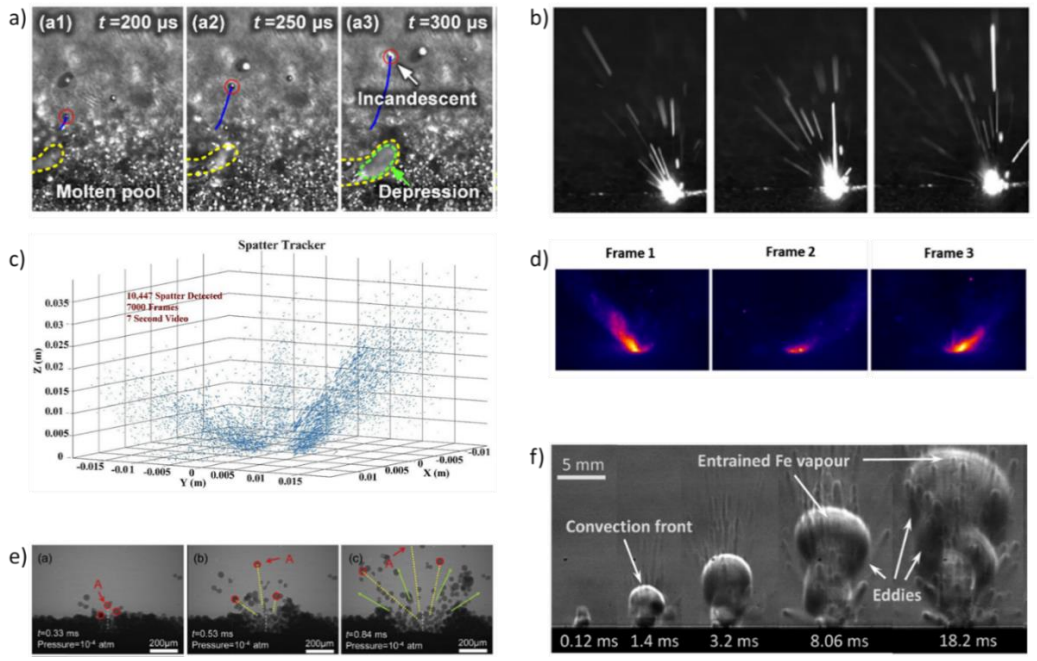

Figure 2.2.j Examples from the in-situ measurement of process by-products in L-PBF: a) ultra high-speed video frames with cameras synchronised to a pulsed high-power diode laser light source [117]; b) high speed video frames where only hotter objects are visible [118]; c) 3D spatter localisation via high-speed stereo vision [119]; d) plume emissions captured with long wave IR video imaging [108]; e) high-speed X-ray video frames [120]; f) Schieleren imaging video frames [116].

In most cases, focus was on the characterisation of the by-product ejection mechanism and its correlation with different process parameters. To achieve this, the FoV was reduced, enabling high spatial resolution. A clear example can be found in Yin et al.'s [117] study which used a self-developed L-PBF system, equipped with a high-speed video imaging setup with a FoV of about (2 × 2) mm (spatial resolution 3.92 to µm/pixel 5.70 µm/pixel). An even higher spatial resolution was obtained by Bidare et al. [116] on a self-developed L-PBF system using a high-speed vision setup with a 7:1 zoom and a FoV of (2 × 1.5) mm. In other studies, a similar high-speed vision setup was applied on industrial L-PBF systems. However, the in-situ measurement involved a larger FoV, possibly including the entire build area, and a lower spatial resolution. For example, Repossini et al. [121] achieved a spatial resolution of about 250 µm/pixel with a FoV of about (250 × 250) mm, corresponding to the build area of the Renishaw AM250 used for the experimental study.

Recent studies proposed a high-speed stereo vision setup to identify and track individual spatters in the 3D space above the layer [119,122–124]. Spatter tracking along its trajectory may improve the characterisation of process by-products and provide additional insights about their mechanism of origin and the influence of process parameters (an example is shown in Figure 2.2.j c)). Eschner et al. [123] used two ultrahigh-speed cameras with an angle between the two camera axes equal to 30° and both cameras inclined by 10° relative to the base plate. This setup provided a temporal resolution of 60,000 fps and a spatial resolution of 40 µm/pixel (FoV: (20 × 10) mm). Eschner et al. [123] showed that this approach, combined with a particle detection and tracking algorithm, was suitable to determine the 3D position and velocity of spatter. The same approach was used in a more recent study [122] to correlate spatter signatures with the penetration depth measured ex-situ. Barrett et al. [124] demonstrated the use of low-cost, high-speed stereo vision methods on an industrial L-PBF machine (EOS M290).

Some researchers used pulsed high-power diode laser light sources [117] or tungsten filament lamps [116] to enable the visualisation of the powder bed, melt track and the hot ejections from the melted area (as shown in Figure 2.2.jF e)). High-speed videos, where only hot objects such as spatter, plume and the laser heated zone are bright enough to be observable, facilitate the image segmentation and feature extraction of process by-products (Figure 2.2.j b)). This was obtained by many other researchers without any external illumination [121,125–127]. In other cases, similar videos were recorded with external light sources to cope with limited sensor sensitivity or with too short integration times [118,128]. Some authors [108,129] used an IR camera to monitor hot plume emissions in L-PBF (Figure 2.2.j d)). For the characterisation of the spatter origination mechanism, various researchers used high-speed high-energy X-ray video imaging system [120,130–132]. The laser scan path is typically limited to a single continuous scan perpendicular to the X-ray beam (Figure 2.2.j e)). The scan occurs on a powder bed held in place by two transparent side walls. With this measurement set up it is not only possible to observe spatter dynamics, but also the melt pool behaviour in the currently melted layer and below the layer, providing information about melt pool penetration depth and sub-surface porosity formation. Bidare et al. [116] combined high-speed video imaging in the visible range with a high-speed Schlieren video imaging method, which enabled the

visualisation of the Ar gas flow and its interaction with the plume and the affected spatters (Figure 2.2.j f)).

2.2.3.3 Measurement of air-borne acoustic emissions

Air-borne acoustic emission sensors have already been used in laser welding applications [88] and a few studies have tested this approach in L-PBF. The underlying principle consists of capturing air density variations during the laser scanning of the part by placing the sensor in the vicinity of the melted area. Therefore, the measured signature is related to the process by-product in terms of plume emissions and plasma formation.

In Wasmer et al. [133] and Shevchik et al. [134], the airborne acoustic emission signal was acquired by means of a fibre Bragg grating optoacoustic sensor installed into the build chamber at about 200 mm from the process zone. In both studies, the sensor was installed on an industrial L-PBF machine and the sampling frequency was 1 MHz. The sensor was placed so that the longitudinal axis of the fibre was perpendicular to the acoustic wave to increase its sensitivity. In Ye et al. [135] a microphone was installed into the build chamber at a 30° angle above the build area. The frequency response of the sensor was in the range 0 to 100 kHz and the signal was acquired with a sampling frequency of 200 kHz. A similar approach was used in Kouprianoff et al. [136]. The information in these measurements can be viewed as signatures of the laser-material interaction during the laser scanning of the part.

2.2.4 Level 3 methods – Melt-pool

In-situ measurements of the melt pool properties have been investigated only in L-PBF, although some EB-PBF level 2 methods attempted to extract features at both track and melt pool level via off-axis video imaging. The significant advantage provided by L-PBF is the possibility of using the laser optical path in co-axial sensing mode. On this basis, the majority of the literature in this field relies on co-axial spatially integrated pyrometry measurements, co-axial spatially resolved video imaging methods or combinations of the two. The novelties presented in most recent studies are mainly related to the analysis of melt pool measurements via machine learning techniques. Nevertheless, a few studies proposed novel sensing solutions such as co-axial dual wavelength video imaging [89,137,138] or co-axial optical emission spectroscopy [94].

2.2.4.1 Spatially integrated methods

In-situ co-axial measurements of melt pool properties represented the core of research in L-PBF process monitoring in the first published studies (between 2010 and 2015, and in a few cases earlier). The melt pool properties of interest include melt pool size or geometry, intensities of the integrated radiation, spatial patterns and emission spectra.

Spatially integrated pyrometry, by means of one or multiple photodiodes, is suitable to measure melt pool radiation intensity with high temporal resolution. Among the most important factors affecting the quality of the measured data, the measurement wavelength range and the sensor FoV play a central role. In all the studies reported [90,139–147] the wavelength range was slightly above or below 1000 nm, whereas some researchers used dual-wavelength measurements in the ranges 700 nm to 1050 nm and 1100 nm to 1700 nm [148–150].

The wavelength region below the laser beam wavelength (typically 1064 nm) allows the capturing of the light emitted by the melt pool (between about 700 nm and 1050 nm). In certain cases, plasma emissions, below 1050 nm, could also be captured [148,149]. However, the radiation energy at the melting temperature has its peak in the NIR region. Measuring melt pool radiation above 1000 nm was prevented, in some cases, by the optical chain [143], but this limit was overcome in other studies [139,141].

Co-axial photodiodes are nowadays available in most industrial L-PBF systems, and, in most cases, a 2D map of melt pool intensities is provided by synchronising the photodiode signal with the laser spot coordinates. A different use of a co-axial photodiode was discussed in Montazeri et al. [90], where the authors showed that the chemical composition of the material can be determined via melt pool radiation measurement, leading to possible material cross-contamination detection. In this case, the detection range of the sensor was 350 nm to 1100 nm, with the aim of measuring the radiation intensity of the plume.

Some researchers proposed in-situ melt pool measurement methods relying on off-axis mounted photodiodes. For example, Nadipalli et al. [151] and Bisht et al. [152] used an analogous approach for melt pool intensity measurements during the production of tensile specimens. The FoV of the sensor covered the entire build area, which enabled the

collection of not only melt pool radiation signals, but also radiation emitted by surrounding hot areas and by-product emissions. Due to this, the characterisation of melt pool properties is limited and imprecise, compared to co-axial methods. Instead of measuring the integrated radiation intensity emitted by the melt pool, Lough et al. [94] used a co-axial optical emission spectroscopy approach to measure the spectral content of the collected radiation and determine the chemistry and relative intensities of the excited species vaporised within the plume. To this aim, the measurement spectral range was 400 nm to 700 nm.

2.2.4.2 Spatially resolved methods

Richer information about melt pool properties and stability over time can be gathered via co-axial video imaging methods, and several studies proposed this approach. In most cases [139,142,143,145,153–159], a high-speed camera (with sampling rate between 1000 fps and 50,000 fps) equipped with a narrow band NIR filter was used to enhance the dynamic range and capture predominant melt pool emissions at the melting temperature. The spatial resolution enabled by this measurement setup ranges between 8 μm/pixel and 21 μm/pixel, due to the limited FoV.

Some researchers used off-axis video imaging methods for melt pool measurements. This approach was made feasible by using high-magnification optics combined with a limited FoV. Zhirnov et al. [160] and Lane et al. [161] used an off-axis high-speed camera combined with a mirror that allowed close-range observation of the melt pool without obstructing the laser, achieving a spatial resolution in the order of 3 μm/pixel. Lane et al. [161] also used an off-axis thermal camera for melt pool thermography at lower resolution (36 μm/pixel). Similarly, Heigel et al. [92,93] used an off-axis IR camera for melt pool length and cooling rate estimations, whereas Scime and Beuth [162] and Bruna-Rosso et al. [163] used off-axis mounted high-speed cameras in the visible range to study the morphology of the melt-pool and its variation along the track.

Only a few researchers reported calibration procedures for melt pool video imaging analysis. Lane et al. [161] calibrated their off-axial high-speed camera, equipped with a NIR filter, by using a light emitting diode-driven integrating sphere, leading to a non-linear calibration curve between blackbody temperature and camera signal. A different approach was adopted by other researchers who proposed the use of dual wavelength

video imaging which involved the acquisition of video image streams at two different wavelengths (700 nm and 950 nm) to enable a temperature estimate via two-colour thermography [89,137,138]. The method allows the avoidance of the difficulties related to melt pool emissivity estimation by calculating the ratio of the radiances measured at the two separate wavelengths, under the assumption of a constant emissivity at these wavelengths. Figure 2.2.k shows some examples of melt pool images and melt pool surface temperature estimations.

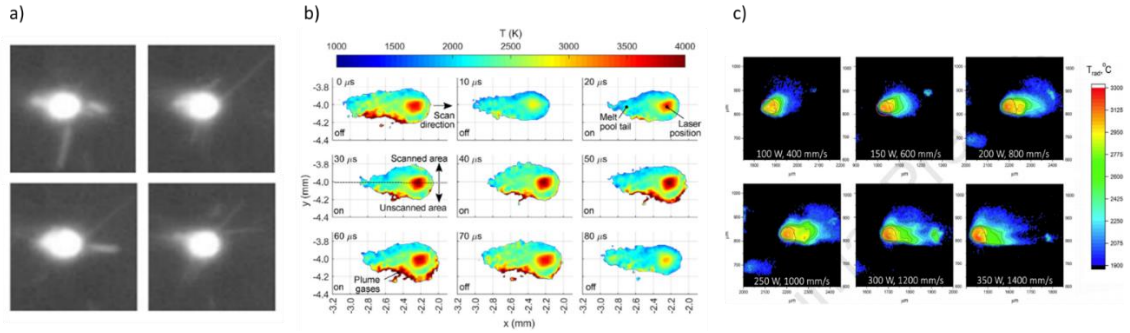

Figure 2.2.k a) Co-axial melt pool images in four sequential video frames in the visible range [164], b) melt pool surface temperature estimation via dual wavelength co-axial video imaging [138], c) melt pool surface temperature estimation via off-axis video imaging for different process parameters [160].

A different spatially resolved approach was used by Kanko et al. [165]. They used a co-axial in-line coherent imaging method to measure the melt pool and surrounding area morphology changes. Unlike from the methods discussed above, which focused on melt pool signatures within the build plane, the in-line coherent imaging approach enables a local reconstruction of the height profile within the melt pool and along the track. This approach has been applied to single tracks only but it could be extended to three-dimensional builds.

2.2.5 Level 4 methods – under the layer

All the in-situ sensing and measurement methods presented in the previous sections involve a measurement of the patterns and phenomena that occur in the layer during production, either before, during or after the melting phase. However, as the next layer is being printed, the material characteristics underneath it are modified as well, due to the partial remelting of top layers and heat exchanges within the build volume. Some in-situ

sensing and measurement methods have been proposed with the aim to gather information about what goes on under the current layer. One major stream of research regards methods that uses high-speed high-energy X-ray imaging systems to observe subsurface melt pool dynamics, the penetration depth and pore formation. Other researchers investigated the use of a similar sensing setup for X-ray diffraction measurements, which allows the characterisation of strain and stress formation and phase transformations [132,166–168]. One study also explored the feasibility of in-situ micro-tomography [169]. A completely different perspective characterises a second mainstream of research where acoustic emissions (from audible sound to ultrasounds and emissions in the megahertz bandwidth) are used to gather information about elastic energy releases under the layer, such as cracks and delamination. A few researchers also studied in-situ measurements of the baseplate [170,171]. All these methods have been applied only in L-PBF so far.

Although X-ray video imaging methods can provide insights about the origin of process by-products, their main use presented and discussed in the literature regards the capability of observing the melt-pool cross-section in a plane perpendicular to the layer. Figure 2.2.l shows an example of the apparatus used for this kind of in-situ measurement [172], and an example of an in-situ X-ray video frame [101]. The high-energy X-ray beam penetrates the material along a direction orthogonal to both the scan and build directions. Laser scanning is performed along a narrow powder bed, spread between two transparent walls (usually glassy carbon sheets). A downstream detection system converts the X-ray signal into visible light by means of a scintillator, and the converted signal is finally recorded by a high-speed camera.

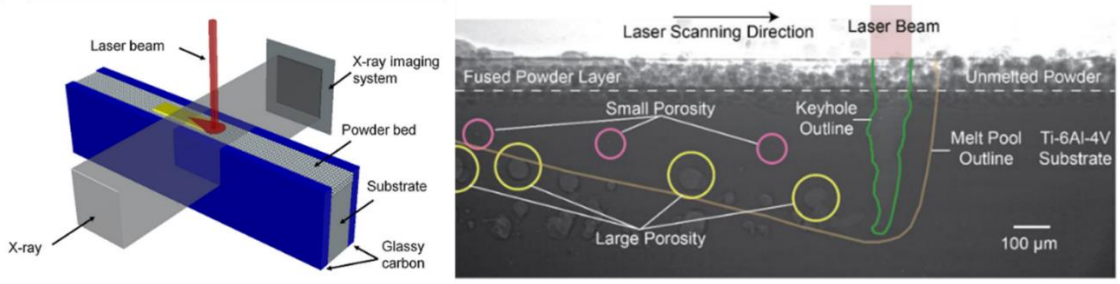

Figure 2.2.l Scheme of the apparatus for in-situ X-ray video imaging in L-PBF (left) [172] and an example of an in-situ X-ray video frame (right) [101].

Figure 2.2.l shows that X-ray imaging for in-situ measurements can be used only at laboratory level using L-PBF prototype systems. Despite not being applicable on

production machines for industrial use, this approach turned out to be convenient to reveal complex dynamical changes in the melt pool and depression zones during laser scanning. This is enabled by the capability to look under the layer and by the very high spatial and temporal resolutions that can be achieved with this method. A spatial resolution of 1 µm/pixel to 2 µm/pixel can be achieved, with a sampling rate higher than 100,000 fps. Calta et al. [168] and Zhao et al. [132] combined in-situ X-ray video imaging with in-situ X-ray diffraction to observe not only subsurface melt pool dynamics but also phase transformations in the material and changes in the strain and stress states. In these studies, two different detectors were used for X-ray imaging and X-ray diffraction. In-situ X-ray diffraction was also studied in Schmeiser et al. [166] and Uhlmann et al. [167]. A completely different configuration was proposed by Lhuissier et al. [169], where the aim was to demonstrate the feasibility of in-situ X-ray micro-tomography for the volumetric reconstruction of the part during the process. Figure 2.2.m (top panel) schematically shows how the apparatus presented by Lhuissier et al. [169] operates. Figure 2.2.m (bottom panel) shows the resulting 3D reconstruction of a wall measured at different consecutive layers (the 3D volume reconstruction was post-processed to remove particles of the powder bed and visualise the bulk wall).

In Lhuissier et al. [169], the build plate was mounted on a piston that is raised up to a "shadow-free" imaging position after powder spreading. A microtomography scan of the deposited powder bed is first acquired. Laser melting is applied at the same imaging position and, once completed, a second microtomography scan is performed. Eventually, the build plate returns to its layering position and a new powder layer is deposited. During the microtomography scan, 1500 projections were acquired resulting in a scan time of 45 seconds. The measurements presented in Lhuissier et al. [169] were gathered with a spatial resolution of 3.64 µm/pixel and a FoV of (8.8 × 6.2) mm.

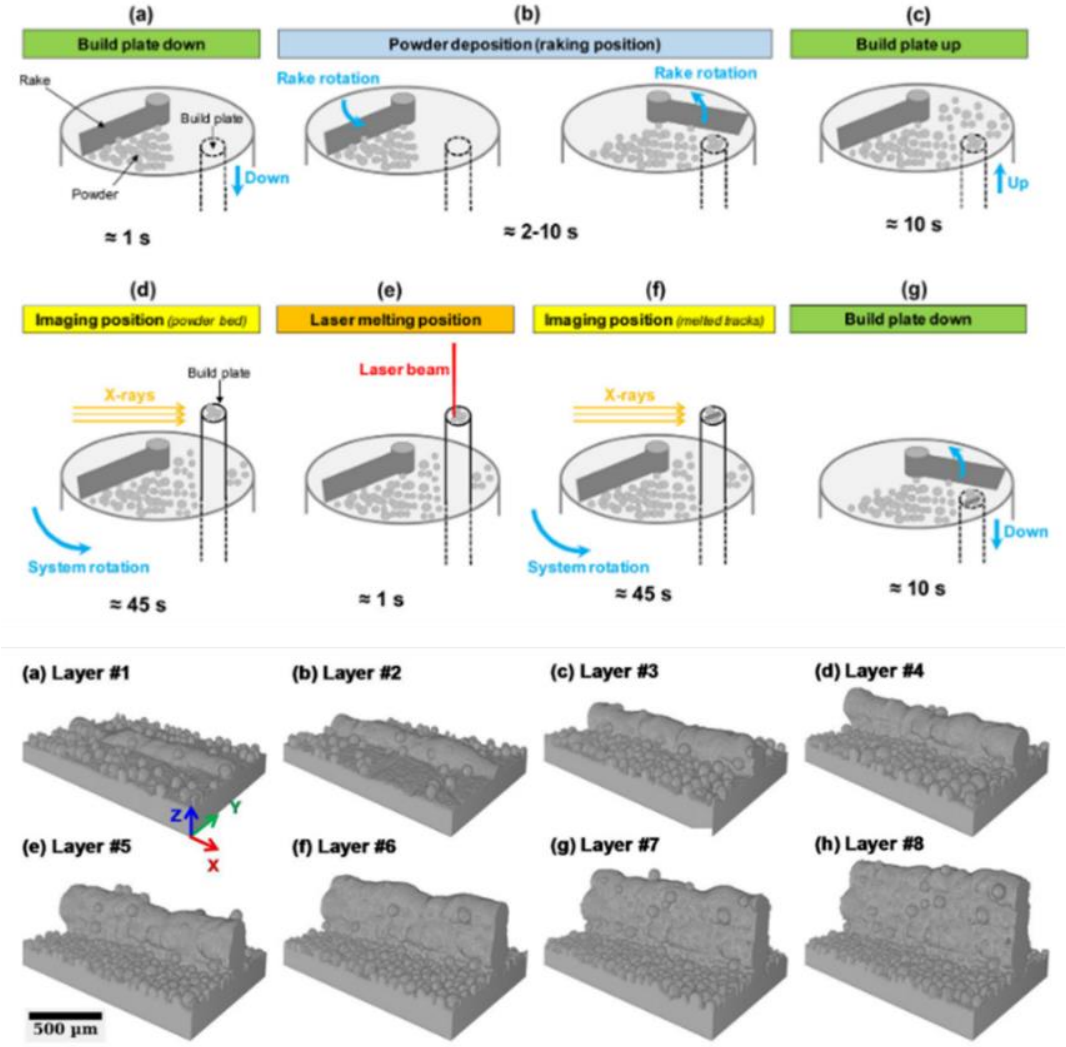

Figure 2.2.m Schematic representation of the working principle of the in-situ X-ray micro-tomography approach presented by Lhuissier et al. [169] (top panels); in-situ 3D reconstruction of a wall measured at different consecutive layers (powder bed particles were removed in 3D data post-processing to visualise the bulk wall).

A different field of research with more direct application potentials in industry regards the in-situ measurements of acoustic emissions. Acoustic emissions can be divided into air-borne and structure-borne emissions. The latter are suitable to detect sudden releases of elastic energy that propagate within the material. This enables the possibility to detect crack formations, detachments of overhang areas from supports or delamination phenomena. The use of multiple sensors placed at different locations could also provide information about the location within the build where the energy release originated. The

structure-borne signal is also influenced by other laser-material interactions and hence they can provide additional insights about changes in process conditions.

The use of structure-borne acoustic emission sensors has been proposed by various authors since the first seminal works of Rieder et al. [173,174] and patented by some major L-PBF system developers [175,176]. Rieder et al. [173,174] proposed an ultrasonic monitoring device in L-PBF mounted on the underside of the baseplate. The bandwidth range was 400 kHz to 30 MHz, with an acquisition frequency of 250 MHz. The researchers measured ultrasound emissions, focusing on the bottom plate interface echo and the backwall echo patterns as proxies of discontinuities in the material, while the specimen build-up height increased. More recently, a similar approach was presented in Eschner et al. [177] but the spectrogram of the signal was used to characterise the acoustic emission signature of the process rather than the recorder echo. Plotnikov et al. [98], instead, monitored the RMS of the signal.

Finally, a couple of studies presented methods for baseplate distortion measurements during the process. In Dunbar et al. [171], a displacement sensor was attached to the underside of the baseplate. A more recent study [170] presented a smart baseplate for L-PBF with an embedded optical fibre strain measurement sensor. Rather than measuring the baseplate deformation, Hehr et al. [170] demonstrated the feasibility of the proposed approach to detect plastic deformations like a delamination from the baseplate.

2.3 In-situ monitoring and in-situ defect detectability

This section is devoted to in-situ monitoring methods, i.e., to the capability of signalling process anomalies that could indicate the onset of defects in the part or undesired changes in the process. For the design of in-situ monitoring methods, two types of correlation could be investigated. The first regards the influence of input variables and controllable factors on in-situ measured quantities, including powder properties, process parameters, part and build geometry and chamber atmosphere. In the recent years, an increasing number of studies has investigated such influences and proposed data analytics and machine learning techniques to classify the process behaviour into different states based on in-situ measured data.

The second type of correlation regards the correspondence of events and anomalies detected during the process and the final quality and performances of the manufactured part. Studies belonging to this second category can be divided into two main classes, one focused on the quality of single tracks or single layers, and one exploring the final properties of three-dimensional parts, including their microstructure, porosity, geometrical errors, residual stresses, presence of cracks or delamination, and mechanical performances.

In many cases, authors varied important process parameters to purposefully introduce flaws in the part. Other studies focused on the effect of geometrical features on process signatures and detectable anomalies, whereas only few authors addressed other sources of process signature variability such as different properties of metal powders (e.g., powder oxidation level or powder feedstocks from different vendors) or different chamber atmosphere conditions (e.g., ambient pressure, inert gas types or gas flow uniformity).

The link between in-situ measured quantities and the final quality of manufactured parts has attracted a wide interest in the recent years. About 50% of studies published since 2017 investigated such a link, either for sake of comprehension of underlying process dynamics or with the aim to develop and test novel in-situ defect detection solutions. One third of them involved single track (or single layer) experiments. Although the analysis of individual track properties is not sufficient to demonstrate actual in-situ defect detection capabilities in three-dimensional parts, it provides relevant information about defect onset mechanisms and the suitability of process signatures to identify variations in the process. This approach has been used mainly in level 2 methods focusing on process by-products and level 3 methods focusing on melt pool properties. The remaining portion of studies was devoted mainly to the in-situ detection of local porosities or the distinction between different density levels, whereas various authors investigated the capability of predicting the final microstructural properties of the part or detecting possible geometrical distortions, and/or the correlation between process signatures and mechanical properties.

2.3.1 Influence of input variables on in-situ signals

Varying process parameters and scan strategies represents the most common way adopted by researchers to intentionally introduce flaws in the final quality and functional

properties of the part and observe consequent anomaly and defect onset mechanisms through in-situ measurement of process signatures.

Various authors showed that different energy density levels in L-PBF generate different surface topographies of each printed slice [38,39,68,69,79,80,178]. Deviations from a uniform and smooth surface were shown both at low energy density (resulting in irregular and porous patterns or even balling effects in more severe cases) and high energy density (resulting in uneven surfaces and superelevated edges). Similar effects have been studied in EB-PBF too, where porous and uneven surface patterns captured by in-situ electronic imaging were observed for different combinations of beam power and scan speed [74,74,75]. An irregular surface topography is more likely to generate defects in the part but it is not a sufficient condition, because partial remelting in following layers may mitigate or even avoid the onset of defects in the part.

Many authors tested different sets of process parameters both in L-PBF and EB-PBF to investigate variations in the thermal history of the process measured in-situ via NIR or IR video imaging and pyrometry. In L-PBF, a variation of the energy density was shown to cause not only an increase of average and peak IR intensities [99], but also the occurrence of local outlying temperatures [96], a variations of the time a pixel temperature stays above a given threshold [95,100], a modification of cooling profile patterns [101] and a shift in emission spectral characteristics associated to specific chemical elements [179]. In EB-PBF, attention has been devoted to the effect of different process parameters on the temporal evolution of the average temperature of the layer [104], and to temporal and spatial thermal gradients in different locations of the part passing from line to point scan strategies [105,106].

A research field that has attracted a wide and recent interest is the analysis of process by-product dynamics as a consequence of different process parameters and energy densities in L-PBF. Various authors showed that an excessive energy input to the material causes large and unstable plume emissions with a large amount of spatters characterized by high speed and spreading at large distances from the melting area [116,121,126,129,180,181]. In these conditions, large droplets of spatter were observed to be more likely ejected from the meltpool [126,180]. Some authors also reported an increase of the backward ejection angle of spatter as the laser power increases [117,181], although the orientation of spatter

ejections can range from forward to backward depending on the combination of laser power and scan speed [116]. In the presence of an insufficient energy input causing lack-of-fusion defects or balling irregularities along the tracks, low plume and spatter emissions were observed [116,121,126,180,181]. However, some authors showed that excessive energy inputs have a much more evident effect on the spatter behaviour than insufficient energy inputs compared with optimal process conditions [121,126]. The effect of varying either the laser power or the scan speed may be different even if the energy density is the same [127].

In-situ X-ray video imaging confirmed these findings and enabled further insight to the by-product properties and origination mechanisms [130,132,182]. Young et al. [130] also showed the generation mechanism of power agglomeration spatters (formed through coalescing of multiple powder particles and spatters) and so-called "defect induced spatters". The latter were observed in correspondence of large pores within previously built layers: the interaction between the melt pool and the depression zone with the localized pore under the surface was shown to cause a sudden eruption out of the melt pool with a consequent liquid material ejection. All the aforementioned studies investigated the spatter generation in single laser L-PBF. Only one study has been devoted to the analysis of process by-products in multi-laser L-PBF [128], showing that when multiple lasers work simultaneously in the same area a larger amount of spatter is produced and their area is larger than the one observed when a single laser beam is used.

A large number of studies has been devoted to the effect of different process parameters on melt pool properties. An increase of the energy input to the material was shown to cause an increase of the melt pool thermal emission (average and standard deviation), the size and peak radiance of melt pool temperature isotherms, melt pool area, lengths and width [139,150,153,160,164,183]. The amplitude of co-axial pyrometer signal varies could be used to identify transitions between conduction and key hole mode laser processing conditions [139]. The analysis of the melt pool shape and size at different energy densities enabled additional insights about stable and unstable process conditions and variations along the scan track, turning point effects and other dynamics related to the complex flow of molten material [132]. Other authors investigated the effect of continuous and pulsed modes on melt pool properties [151,154,155]. Vasileska et al.

[154] showed the melt pool area increase as a consequence of the increase of duty cycle in pulsed mode, whereas Demir et al. [155] showed the feasibility of assigning different emission types in different regions of the same part to keep the melt pool size stable during the entire process. In particular, pulsed mode was suggested for thin walls and continuous mode for bulk regions. Demir et al. [155] also showed that the energy density is not sufficient to describe the melting behaviour, as under the same energy density continuous and pulsed mode emission regimes resulted in different melt pool dimensions. Kolb et al. [153] showed that the melt pool properties are affected also by the surface roughness of the consolidated material beneath the current layer. The most significant mechanisms of laser-material interactions, convective motions, penetration depth variation, powder consolidation and pore formation for different sets of process parameters were highlighted in depth via in-situ X-ray video imaging [182,184,185].

Eventually, both air-borne and structure-borne acoustic emissions were shown to be affected by process parameters. Wasmer et al. [133] and Shevchik et al. [134] showed that different scan speeds caused different wavelet spectrograms patterns of the air-borne acoustic signal. The influence of process parameters on time and frequency domain features of the air-borne signal were discussed by Ye et al. [135] and Kouprianoff et al. [136], whereas Eschner et al. [177] and Plotnikov et al. [98] showed similar effects on structure-borne acoustic signals too.

2.3.2 In-situ detectability of defects and prediction of final part properties

2.3.2.1 In-situ estimation of single track quality

Among the studies involving single track experiments, only few proposed machine learning methods suitable to determine the quality of the track based on in-situ measurements.

Ye et al. [186] proposed a deep belief network classifier that exploited in-situ video image data on process by-products. The algorithm was trained in two different modes: i) using in-situ images as direct inputs for the network, which led to a classification accuracy of about 83% and ii) using extracted spatter and plume descriptors (including areas, lengths, widths, orientations, perimeters, etc.), which led to a classification accuracy of about 81.9%. The same authors applied the same type of classifier to air-borne acoustic signals

[135]. In this case, the raw acoustic signal was pre-filtered and processed via fast Fourier transform before being provided as input to the deep belief network. The results showed a classification accuracy of 93.63%. Zhang et al. [187] compared different classification algorithms, either applied to plume and spatter descriptors or to raw images, showing that the best classification accuracy, in the order of 92.8%, could be achieved by applying a Convolutional Neural Network (CNN) directly on raw images. Zhang et al. [188] showed that previously presented results could be further improved by additionally including temporal information within the trained network. The underlying idea is that the relevant information content about spatter and plume behaviour is not only captured by individual video frames, but also by variations in sequential frames. Zhang et al. [188] proposed a hybrid CNN scheme consisting of two steps. In the first step, the network learns spatial features from single images. In the second step, the features extracted in step 1 are rearranged according to the video frame sequence and used as inputs to a second network, whose output is the classified process state. With this approach, an overall accuracy of 99.6% was achieved. However, all these methods were applied to single tracks of simple specimens. There is still a need for studies demonstrating the suitability of L-PBF by-product signatures, to identify changes of the process state in the presence of complex shapes, or to detect the onset of local defects.

A semi-supervised classification approach was proposed by Yuan et al. [164], who used melt pool images acquired by means of a co-axial high-speed camera. The semi-supervised approach trains the classifier using both labelled and unlabeled data. Labelling individual data samples can be a time-consuming task and defining the correct label for some samples is not always straight forward. Single tracks AISI 316L stainless steel were labelled by measuring their height after the process. The proposed CNN applied to melt pool images combined a supervised and unsupervised model. The classifier was trained using 1000 training data points, by varying the number of labelled ones. Yuan et al. [164] reported a successful classification rate of 93.8% when 50% of the training data were unlabeled. The classification performance decreased as the amount of unlabeled data increased.

2.3.2.2 In-situ porosity detection

Porosity is the defect that attracted the largest interest and highest number of studies in the literature. Nonetheless, the number of researchers who effectively demonstrated practical in-situ porosity detection capabilities, is still limited. The literature on this area covers three distinct approaches when testing porosity detection, i) voids included into the model of the part, which are also referred to as "artificial" or "intentional" pores, ii) local porosity (single pores or local clusters of pores, either spherical or irregular pores caused by lack of fusion – LoF) and iii) part density (the overall percentage of voids in the volume). The majority of authors investigated the correlation between in-situ signals and the overall part density, but only few of them demonstrated the capability to detect local porosities within the part or even individual pores.

The advantage of inserting artificial pores in the part is that their location and shape is known in advance, hence it is easier to determine the effect of these artificial flaws on in-situ acquired signals. The main drawback is that the pattern of the measured process signatures is not fully representative of the one that can be observed when a real pore originates in the part. In effect, an artificial void implies that a small region of the layer is not scanned, whereas a real pore originates from the beam-material interaction without scan interruptions along the track.

Voids of different shapes and sizes were used in various studies, including cubic voids with sizes in the range 30 μm to 300 μm [137] or 50 μm to 750 μm [47,79,80], cylindrical voids with diameters in the range 50 μm to 750 μm [47,79,80] and spherical voids with diameters in the range 600 μm to 900 μm [84]. Imani et al. [79,80] and Mahmoudi et al. [52] used intentionally seeded voids to test the capability of their proposed layerwise surface pattern monitoring methods, to detect surface discontinuities within the printed area. Both the methods presented by Imani et al. [79,80] and Mahmoudi et al. [52] were applied in L-PBF and worked by partitioning the surfaces into regions of interest (RoIs) and classifying them into defective or defect-free regions. In Imani et al. [79,80] , RoIs were generated from optical layerwise imaging, such that each RoI has the same number of pixels but different shapes, to adapt to layerwise varying part geometry. In Mahmoudi et al. [52], RoIs were identified as rectangular regions placed where connected components were observed after a binarisation of the layerwise reconstructed thermal

map. Imani et al. [79,80] used a deep learning approach to classify the RoIs into defective or defect-free. An accuracy (the ratio of RoIs that were correctly identified) of 92.5% was reported for artificial voids of different sizes and shapes. Mahmoudi et al. [52] proposed a modelling step, based on a Gaussian process model, that flags pixels with statistically significant deviations, followed by a final classification step to determine whether a RoI includes a defect or not. An accuracy of 96% was reported for this defect detection method, although tests were only carried out in the presence of one single artificially seeded void. Both the methods presented by Imani et al. [79,80] and Mahmoudi et al. [52] required a training phase involving samples of defective and defect-free image data.

Mitchell et al. [137] proposed a method, based on off-axis dual wavelength video imaging, that combined the estimation of melt pool properties with a reconstruction of the thermal map of the part. In the presence of artificially seeded voids, Mitchell et al. [137] showed that voids as small as 120 μm were identified, however, the in-situ reconstructed void volume was underestimated by up to 28% with respect to the corresponding post-process reconstruction via X-ray computed tomography (XCT).

Mitchell et al. [137] additionally investigated the capability of automatically detecting not only artificial voids but also natural porosity generated by the process. The AISI 316L specimens produced via L-PBF mainly included spherical pores with an equivalent spherical diameter (ESD) ranging between 11.4 μm (minimum size detectable by the micro-computer tomography (micro-CT)) and 70 μm. A neighborhood searching algorithm was proposed to classify individual melt pool images into normal or outlier, by comparing the similarity of the melt pool in a given location with melt pools observed in its vicinity, within a given radius in terms of melt pool aspect ratio and orientation. Mitchell et al. [137] showed that the percentage of pores detected by means of melt pool images signaled as outliers was in the range 25% to 55%, but it increased above 70% when considering only pores with ESD larger than 50 μm. Nevertheless, a relatively high false positive rate between 23% and 58% was reported. Examples of results from the study of Mitchell et al. [137] are shown in Figure 2.3.a.

The high false alarm rate highlights the need for further research developments to design more effective in-situ monitoring tools for porosity detection. Such high false alarm rates

can also be related to the remelting effect as the process continues, which may cause partial pore annihilation in underneath layers.

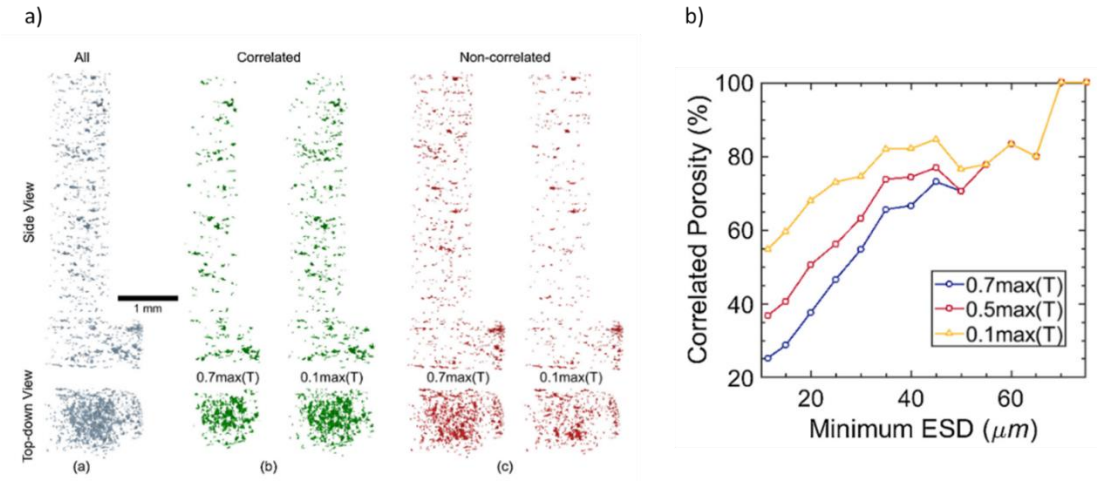

Figure 2.3.a Examples of results from Mitchell et al. [137]; a) three-dimensional reconstructions of all pores identified using micro-CT, pores correlated with in-situ outlying melt pool signals, and pores not correlated; b) percentages of pores spatially coincident/correlated with outlier melt pools at different minimum ESDs and different threshold values.

Other studies investigated the capability to detect local pores using different in-situ monitoring approaches. As far as level 1 methods are concerned, Gobert et al. [46] presented a voxel-wise comparison between a 3D reconstruction of the part, based on in-situ layerwise image pixel intensities and the post-process XCT reconstruction. A landmark-based registration between the in-situ data and the CT data was applied. Then, the support vector machine (SVM) approach was used as a binary classifier to detect flaws in the in-situ reconstruction. Layerwise images were acquired with different illumination conditions, and Gobert et al. [46] showed that the most appropriate pore detection performances were achieved using an ensemble learning system, merging SVM models associated with each condition. The test specimen built with stainless steel powder had pores with ESD in the range 29.5 µm to 50.5 µm (with very few above 50.5 µm). Gobert et al. [46] reported a detection accuracy of 85%, with a "precision" of 64%, where the precision was defined as the ratio between the number of true positives and the total number of true positives and false positives.

A comparison between in-situ and post-process XCT reconstructions of specimens, produced via L-PBF, was presented by Bamberg et al. [53], who performed a layerwise mapping of hot and cold areas. This method was later implemented by EOS in the EOSTATE suite and called "Optical Tomography". Although no information about the pore detection algorithm was provided, the authors showed a probability of detection between 90% and 95% for lack-of-fusion flaws with diameters in the order of 150 μm.

A voxel-wise comparison between thermal signatures generated via in-situ thermography and the XCT of the part was carried out by Mohr et al. [100], Lough et al. [95,189] and Bartlett et al. [67]. Lough et al. [95] compared different synthetic descriptors to generate layerwise thermal maps from IR video image data. They showed a correlation between the proposed synthetic indexes and the presence of local pores (at least the largest ones). Bartlett et al. [67] proposed another rule to detect potential anomalies in thermal maps. The rule consists of signaling any pixel whose temperature is K standard deviations above or below the average temperature of the layer. They applied this approach to cylindrical specimens, showing a detection rate of 33% for keyhole porosity and 82% for lack-of-fusion porosity. Pores below approximately 50 μm were only detected with a 50% success rate, whereas all pores larger than 500 μm were correctly detected. The researchers also showed that false alarms were strongly affected by the selected value of K. A correlation between subsurface pores and cooling profiles reconstructed via in-situ thermography was presented by Paulson et al. [101], however, in this case, in-situ X-ray video imaging was used as ground truth instead of post-process XCT inspection. Pores were classified into small (<10 μm) and large (>10 μm), mainly focusing on spherical ones. By testing different sets of thermal history features and different classification algorithms, an accuracy in the range 84% to 100% was reported.

Similar comparisons between in-situ reconstructed porosity maps and XCT inspections have also been carried out in EB-PBF. Yoder et al. [55] used the LayerQam system developed by Arcam to acquire layerwise images of the build in the NIR range, resulting in a voxel size of the in-situ data of (100 × 100 × 50) μm. Potential pores were identified simply by setting a threshold-to-pixel intensity, as surface cavities were assumed to yield a bright spot in the image. Lack-of-fusion defects were concentrated in banded regions along vertical tensile specimens. Yoder et al. [55] qualitatively demonstrated the

correspondence between pore concentration regions signaled by the in-situ monitoring tool and "ground truth" pore concentration regions from the XCT measurements. They also showed that tensile specimens failed in correspondence of those bands. The relevance of the overall build layout for the quality of individual parts in the build confirms the results discussed by Williams et al. [89] in L-PBF. Arnold et al. [74], instead, showed a comparison between in-situ electronic imaging, post-process optical microscopy on a prepared micro-section and XCT, as shown in Figure 2.3.b. Rather than identifying individual pores, Arnold et al. [74] directly compared the pixel intensities in the images generated with different in-situ and ex-situ methods. A good agreement was highlighted for lack-of-fusion pores larger than 100 μm.

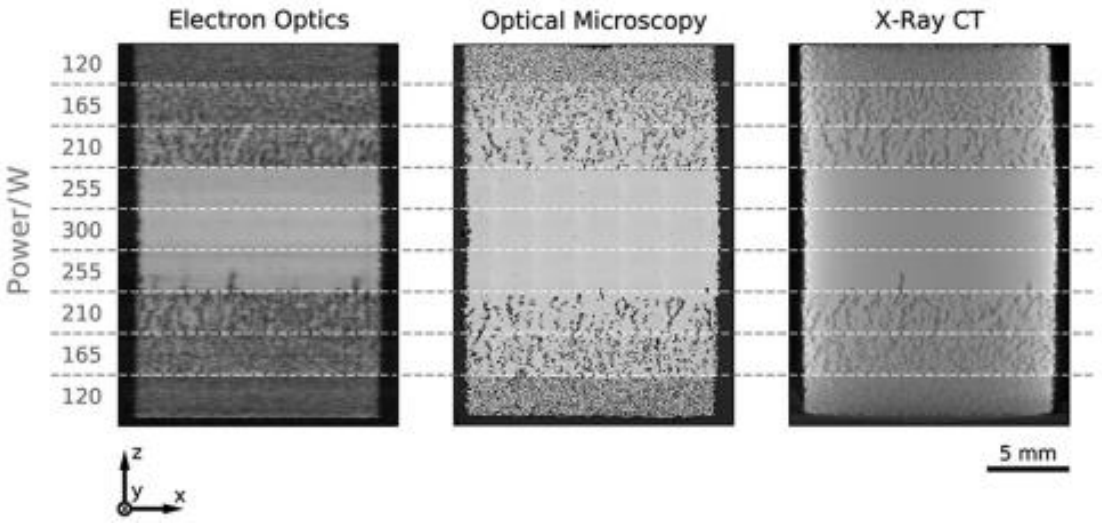

Figure 2.3.b Comparison between a cross-Section from an in-situ electronic image, ex-situ optical microscopy and ex-situ XCT [74].

2.3.2.3 In-situ detection of geometrical distortions

Almost all the methods presented in the literature for the in-situ detection of geometrical distortions belong to level 1 and level 2. Regarding level 1 methods, the possibility to directly measure the geometry of the printed slice represents the major driver for in-situ geometrical distortion detection. However, only a few researchers developed automated alarm rules for the detection of deviations from the nominal shape with a validation based on ex-situ inspections of the final part. Gaikwad et al. [82] presented a CNN for the in-situ prediction of the quality of thin-wall Ti6Al4V parts in L-PBF. Instead of reconstructing the slice contour, de-noised and binarised images of the powder bed were

provided as input to the CNN. Gaikwad et al. [82] showed agreement in the range 80% to 98% between the in-situ predicted quality of the thin walls and their ex-situ measured quality.

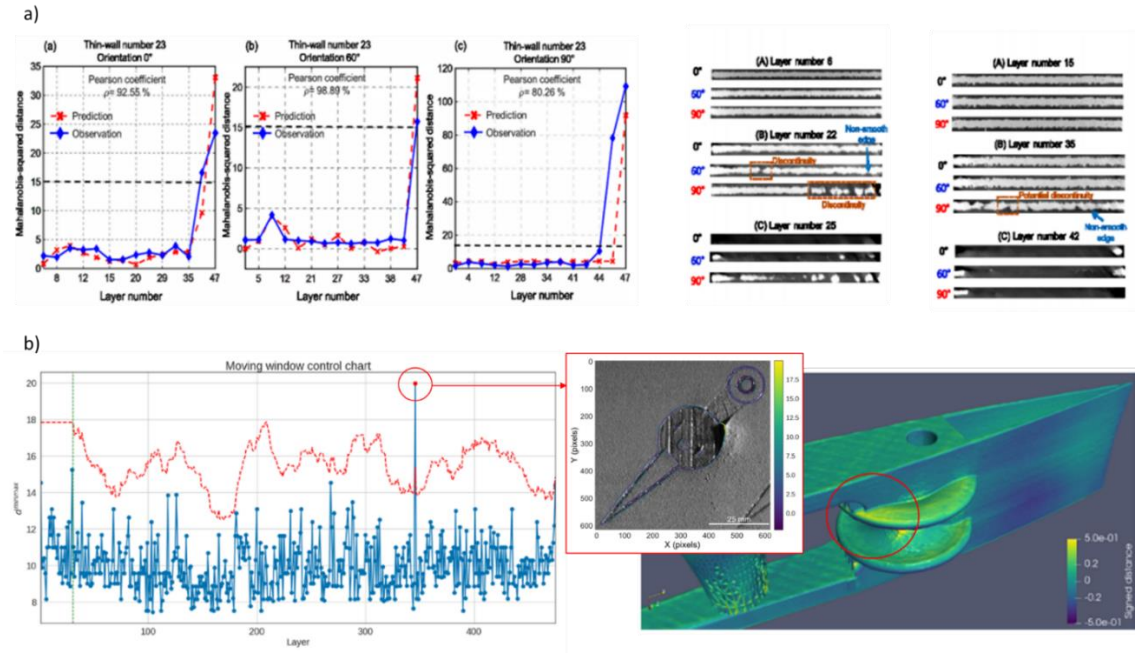

Figure 2.3.c a) Comparison between in-situ and ex-situ estimates of the thin-wall quality in Gaikwad et al. [82] for different thin wall orientations (the horizontal dashed line indicates the upper limit before the thin wall collapsed) and examples of thin-wall defects; b) moving window control chart for the in-situ detection of geometrical distortions proposed by Pagani et al. [48] with an example of a detected geometrical distortion caused by warpage of the part.

More recently, Pagani et al. [48] presented a statistical process monitoring approach for the in-situ detection of geometrical errors in L-PBF. The method allows modelling the natural variability of geometric errors for complex shapes whose layerwise geometry is changing every layer. This approach enabled the identification of anomalies in one or multiple layers through the estimation of a deviation index capturing local mismatches between the in-situ observed shape and the nominal one from the slice CAD model. The method was tested by producing Ti6Al4V specimens with complex shapes on an industrial L-PBF system, using the already embedded powder bed camera and light source. Pagani et al. [48] showed that the proposed approach produced a false alarm rate very close to the targeted one and allowed the signaling of various anomalies

corresponding to geometrical deformations quantified after the process via XCT inspection. Figure 2.3.c shows examples of thin-wall quality prediction by Gaikwad et al. [82] and the statistical process monitoring approach developed by Pagani et al. [48].

Level 1 methods, based on the analysis of the surface patterns of the powder bed and the printed slice, could also be suitable to detect geometrical distortions. A few researchers demonstrated correlations between in-situ detected and classified anomalies in one or multiple layers as well as the final quality of the part. Scime and Beuth [50,51] combined layerwise imaging in the visible range with a multi-scale CNN (MsCNN) in L-PBF, to automatically detect various kinds of anomalies such as recoater hopping and streaking, incomplete powder spreading, presence of debris on the powder bed, super-elevated edges and other part damages. Part damages were successfully classified in 94.2% of test samples with a false alarm rate of 0.7% (anomalies of any kind signaled in defect-free images). The method was validated during the L-PBF of an Inconel 718 heat exchanger, where macroscopic defects were observed and detected by the proposed approach. The training was performed using fifty-one builds produced on industrial systems involving different materials. An expert user manually selected square image patches from powder bed images corresponding to either correct powder spreading or anomalies belonging to different categories. The training set included about 10,000 patches. Although the formation of such a large dataset could be quite demanding, once it has been made available, it could be used to train the classifier implemented on different L-PBF machines during the production of different materials.

Scime et al. [49] recently extended and tuned the method previously proposed by Scime and Beuth [50] and tested a transfer learning approach for the implementation of a classification algorithm, not only on different L-PBF machines from different vendors, but also in various metal AM technologies, for example, EB-PBF and binder jetting, using different sensing setups. Scime et al. [49] showed that false positive and false negative rates varied within a relatively wide range, depending on the AM system where the algorithm was tested. Best validation performances involved a false alarm rate of 0.4% and a true positive rate of 99.8%. Examples of in-situ detected geometrical distortions with these methods are shown in Figure 2.3.d.

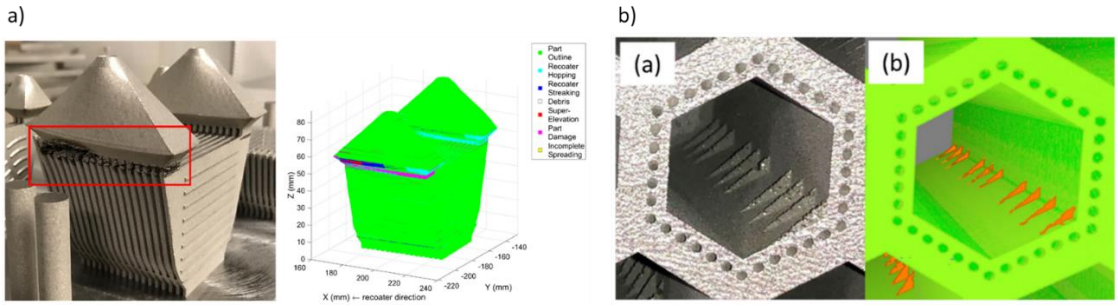

Figure 2.3.d Examples of geometrical distortions and corresponding in-situ anomaly detection in a) Scime and Beuth [50] and b) Scime et al. [49].

A few other solutions suitable to detect anomalies affecting the geometrical accuracy of the part were proposed in the literature using level 2 in-situ monitoring methods. Colosimo and Grasso [190] proposed a hot-spot detection methodology based on the in-process analysis of the spatio-temporal auto-correlation pattern of pixel intensities in high-speed videos gathered through off-axis machine vision in the visible range. They showed that local anomalous heat accumulations in L-PBF could lead to micro- and macro-scale geometrical deformations in the final part. Grasso et al. [191] proposed the use of an extension of the principal component analysis (PCA) method for high-speed video-image data. This extension, also known as "T-mode PCA", is suitable to detect pixels whose intensity patterns over time exhibit anomalous temporal auto-correlations, which is a condition typically associated with pixels that remain hot for a long time with a slow cooling gradient. The spatial mapping of a synthetic PCA-based control statistic combined with a clustering-based alarm rule allowed the automated identification and localisation of local hot-spot events. This was expanded on with a spatio-temporal PCA method, where a spatial weight matrix was included into the PCA decomposition to account for both the temporal and spatial auto-correlations of pixel intensities in the video image. This allowed the detection of hot-spot events to be faster and more reliable. The method was tested during the L-PBF production of a complex geometry where hot-spots originated due to the presence of over-hang acute corners, leading to local geometrical distortions. In-situ video images were acquired by means of a high-speed camera in the visible range, placed outside the front viewport of an industrial L-PBF system. A more recent study of the same authors [192] presented a different approach based on the spatio-temporal modelling of background and foreground patterns of the same high-speed video

image data. Ye et al. [192] showed that the proposed model-based approach was faster and more computationally efficient in detecting hot-spot events, at the expense of a number of parameters that needed to be tuned during the training phase.

A different perspective was adopted in Grasso et al. [34] and Grasso and Colosimo [108] where a statistical monitoring method was proposed to monitor the stability over time of plume emissions during the L-PBF of pure zinc specimens with different process parameters. Off-axis IR video images were processed to isolate the RoI corresponding to the plume and extract salient features, such as the area, average intensity and orientation. A few initial layers were used to estimate the control limits to be applied in all following layers. Results showed that unstable process conditions leading to defective parts could be quickly detected since their onset stage. Such out-of-control states were characterised by anomalous and explosive plume patterns becoming more and more frequent along the build. Results also showed that no violations of the control limits occurred when optimal process parameters were used, leading to fully dense parts.

2.4 Research gaps

Many studies have been devoted to in-situ measurement and monitoring of PBF processes in the recent years. The majority of these studies presented and demonstrated in-situ anomaly and defect detection capabilities. However, there still is a lack of methods suitable to detect local flaws with acceptable false alarm rates. Without reliable detect detection methods for processing the data acquire, these systems have limited applications outside of research environments.

A significant limitation of the current state of the art regards the fact that, in the majority of studies, the proposed methods were tested during single track experiments or during the production of simple specimens. This is often motivated by the need for easing post-process inspections and tests to correlate in-situ measurements with quality and mechanical properties. This leads to at least two main issues. On the one hand, defect onset mechanisms and process signature dynamics in complex shapes can be quite different from those observed in simple specimens. On the other hand, there is a lack of methods to transfer knowledge and models from the simple specimens used during the development phase to the in-situ monitoring of more complex shapes. This latter issue is

also related to the training of machine learning approaches for defect detection or process state classification. Full powder bed monitoring and analysis is key to better understand the build process, and to create reliable defect detecting systems rather than just sampling small regions or single tracks on the powder bed. Although some full field monitoring methods do exist, they are mostly focussed on the analysis of optic image data taken per layer, where difference in greyscale values over the image may be indicative of surface features on the powder bed. Some efforts have been made to acquire topographical maps of the powder bed through FP, but these either focus on acquiring a high resolution measurement over a small region of the powder bed [59], or have covered a larger measurement area at the sacrifice of resolution to analyse larger bed features such as elevation drops from sintering [61,62,193] or curling defects [194]. High resolution topographical measurements capable of identifying small scale features generated by the lasing process, such as weld tracks (nominally 100 µm in width), elongated pores (50 µm to 500 µm), balling (up to 500 µm in width and potentially the length of the build) [25], unfused powder (100 µm to 150 µm) [195] and lattice deviations (up to 500 µm) [26], over the entire powder bed, which may be up to (400 × 400) mm, are yet to be developed.

3 System concept, design, and initial testing

As has been discussed in the previous chapter, a significant gap in the literature comes from the lack of monitoring methods with adequate automatic anomaly detection over the entire volume of the part as it built. Current research has shown promising results when automatically assessing the quality of single weld tracks. However, when it comes to detecting build anomalies such as pores, spatter, balling and geometrical distortions over the entire build area capabilities are far more limited, typically only being able to identify larger features on the powder bed with a lower level of reliability. To achieve a more reliable identification of smaller features over the entire build area a new approach to both monitoring the build plate, and processing the data collected is required. In this chapter, the development of a potential system to achieve this goal is discussed, from original concept to initial prototype and testing.

3.1 System concept

The complex nature of the PBF process makes for a difficult challenge when considering appropriate inspection methods to implement. Four key factors to consider are:

1. The impact on manufacturing times that the measurement system may have.
2. The resolving capabilities and range limitations of the chosen method.
3. The spatial limitations of the PBF chamber.
4. The environmental conditions of the build chamber.

PBF processes typically have long build times due to their layer-by-layer nature, with builds potentially taking days depending on the size and complexity of the component being manufactured. In a production environment, any additional time added to the build process results in additional costs for the company. PBF machine manufacturers have been putting a significant focus on reducing these build times, such as Renishaw's 500Q systems implementing four lasers to decrease the time for each layer's completion. To reduce the impact that an inspection system may have on the overall build time, data collection must either be rapid, or synchronised with the PBF mechanisms so that the machine is not significantly slowed or paused for too long.

As PBF technologies continue to advance, the build areas of the systems continue to increase. Current generation systems have build areas up to 160,000 mm^2, such as the EOS M 400-4, Aconity ONE, and SLM solutions SLM 800 machines. A robust defect detection system must be effective over the entire powder bed area, whilst also being capable of identifying relevant process signatures that could be regarded as defects.

The spatial limitations of L-PBF build chambers must be taken into consideration when implementing a measurement system. Any components places in the machine must not significantly interfere with the operation of the machine such that the build process is altered, or the machine's components are obstructed or damaged. The three main considerations to ensure this are the path of the laser over the build area, the powder spreading system and the gas flow directly over the powder bed.

The harsh environment of the L-PBF process, created by the need for low pressure inert atmosphere and the ejection of molten materials from the laser melting of powdered material, make the placement and protection of any inspection system challenging. These conditions, and the lack of physical tool-workpiece interaction, make contact metrology unsuitable for in-process monitoring.

Machine vision systems have been proposed by multiple researchers in the field due to the their rapid acquisition rates, non-contact functionality, possible wide FoV and the small, easy to secure form factor of cameras [40,41,43,45,46,61,63,77,196,197]. Where many approaches have been focussed around the use of optical vision cameras and image processing to identify regions of non-conformity in the build layers, other approaches have used a machine vision method known as fringe projection (FP), which enables the generation of a topographical map of the surface rather than a 2D image of the build plate. Topographical data has a benefit over simple imaging systems as more dimensional information can be extracted such as height and volume of features.

3.1.1 Fringe Projection

FP is an optical measurement method commonly used for the three-dimensional measurement of object form and is used in many sectors due to its relatively fast acquisition rates and non-destructive nature [198–201]. In their simplest form, FP systems consist of a single camera-projector pair, sharing a common FoV that acts as the

measurement volume. Fringe images from the projector are distorted by the object's shape and, when viewed from a different perspective by the camera, these distortions can be used to reconstruct the shape of the object, as shown in Figure 3.1.a. Depth information can be derived from the distortion of the fringes, making it possible to calculate the form of an object through a series of image projections and captures. The rapid acquisition rate and non-contact nature of FP make it appealing as an in-process measurement tool. However, FP has several disadvantages. When measuring highly specular surfaces, as would be expected during the AM build process of a metal component, data quality decreases and data drop out occurs when the positional value cannot be resolved [200]. In addition to data drop out issues, there is an inherent trade-off between the system's FoV and the resolving power of a given camera sensor, meaning that obtaining a measurement of the complete powder bed region often requires the sacrifice of smaller scale surface details due to an effective decrease in magnification [202]. To combat issues such as data drop out or surface occlusions due to part form, FP systems often use multi-view approaches that allow multiple measurements to be taken from different viewing points. Typically, the capture of multiple views is performed by placing the part being measured on a rotary table and performing a measurement at different fixed angles [203–205] or by mounting the FP system onto a robot arm to be moved around the part [206,207]. Other methods have focussed on the simultaneous capture of multiple views by introducing more camera-projector pairs [208–210]. Simultaneous capture is beneficial as no moving parts are required and the capture time can be greatly reduced when compared to rotation stage or robot arm methods. However, when using a simultaneous capture approach with multiple fixed cameras, limitations in the flexibility of the system are introduced.

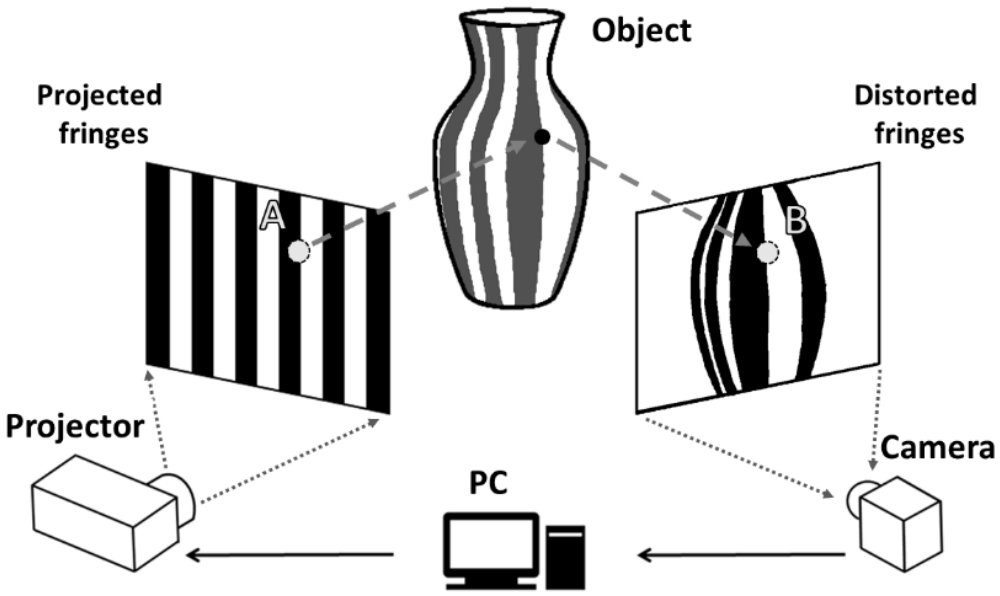

Figure 3.1.a. Illustration of depth determination in FP. Points A and B mark the same point on the measured object through both the projector's and camera's perspectives.

The rapid acquisition and non-contact nature of FP makes the method ideal for performing in-process topographic measurements without significantly interrupting the build process. Multiple in-process monitoring systems have been proposed for PBF systems which the target of detecting defects that have arisen on the build area through topographical analysis of the powder bed.

Land et al. [211] and Zhang et al. [62] present work on a single camera-projector pair FP system for use in a custom built metal L-PBF machine. The system consists of a DLSR (pixel array: 5184 × 3456) that measured approximately (100 × 100) mm of the build plate. This system proved capable of recognising regions of sintered material due to the elevation drop from the powder layer. Zhang et al [212] later reconfigured the system using a machine vision camera (pixel array: 4096 × 2160) which covered a reduced FoV of (28 × 15) mm. In this configuration, a lateral point spacing of 6.8 μm was achieved with a single point repeatability of 0.47 μm. This higher lateral resolution was achieved by trading off the larger FoV, making the system less beneficial for full powder bed process monitoring, but still highlighting FP as a valuable tool for in-process high resolution measurement. Li et al. [213] applied a two camera, single projector FP set up to a metal L-PBF system capable of identifying sintered contours. For this work, two machine vision cameras (pixel array: 2592 × 1944) were used to measure a region of the

powder bed approximately (200 × 250) mm in size. Resolving capabilities were not discussed, but regions of the powder that had dropped from the nominal plane were identifiable. Southon et al. [214] investigated the use of a commercial FP system pointed through the viewing window of a commercial polymer L-PBF machine as an in-process monitoring system. Over a measured region of approximately (200 × 100) mm, curling defects were identified on the test part being observed, with height differences as low as 50 μm being clearly visible in the data. Liu et al. used the FP method and applied it to an EB-PBF system [215,216]. In this method a single camera and projector pair (pixel arrays of 3016 × 4016 and 912 × 1140, respectively) was used to observe a region of approximately (90 × 90) mm on the powder bed. A measurement of twenty-four fringes was taken in approximately 2 seconds. This system implemented an active feedback loop that either respreads the powder or alters the process parameters for correction when an issue is identified. The system was typically found to measure vertical distances to within 7 μm when compared to a laser interferometer displacement measurement with the accuracy of the system quoted to be 15.8 μm.

From these publications, FP methods have been demonstrated to have potential for in-process monitoring of AM systems. However, there is a trade off between FoV and lateral resolving capabilities in these systems. Fringe projection systems that have been able to measure all. or the majority, of a modern systems powder bed area ((250 × 250) mm to (400 × 400) mm in size) are only discussed as resolving larger scale features over the build such as curling over the part or elevation drop of sintered regions. Systems that have been discussed to have high lateral sampling have been achieved by lowering the FoV to a small region of the powder bed, and in these cases lateral sampling or single point repeatability is reported rather than identifiable feature sizes within the data. Improvements need to be made to achieve a higher resolution surface reconstruction that can be used for feature-based identification of defects, such as those discussed in section 2.4, over the majority of the build area for in-process monitoring purposes [217–220]. A feature-based identification approach could provide a more robust method of determining the successful manufacture of each additive layer and, therefore, the whole component.

To address these issues, a multi-view FP approach has been chosen to investigate the possibility of using it as an in-process measurement system for L-PBF. A four camera

system has been designed with the aim of maintaining a high resolving power over the entire powder bed area by combining multiple measurements from four different cameras. Using multiple views to measure the same surface also reduces regions of data drop out (if, when data drop out occurs in one camera, one of the other views is able to measure it and fill in the gap on the surface). Using multiple views to acquire four point clouds should also increase user confidence in the measurements as a metric for data quality could be calculated based on how well the four point clouds agree on the surface reconstruction.

3.1.2 System design

For the development of a multi-view FP system for in-process inspection of a metal L-PBF machine, an out of machine prototype was developed to test in a lab environment. The prototype was based around the chamber dimensions of a Renishaw AM250 machine with a (250 × 250) mm powder bed area. The target of the system is to use a multi-view FP [221] method with four cameras to measure surface topography of an L-PBF layer. The camera positions were chosen to provide a full field image of the build area from each perspective so that four point clouds can be collected from a single measurement [222] and combined into a high resolution surface reconstruction.

To achieve a full field measurement from each perspective the cameras and projector must be placed at a significant distance from measurement volume. This distance means that the impact of the components presence on the powder spreading mechanism and the lower chamber air flow should be minimal with respect to machine performance and build quality. However, the effect of the components presence on machine performance should still be investigated as the benefits of a defect detection system would be redundant if the system itself was to introduce defects. In the chosen design the camera positions were placed in the upper corners of the build chamber, with the projector placed outside of the build chamber, projecting through a upper window at the front of the chamber that is typically used for a light source that is non-essential to the machine operation (design shown in Figure 3.1.b). The positioning of the components for this prototype have been selected so that the volume below the laser lens, and any moving components such as the powder spreader or powder hopper have as much clearance as possible, whilst maintaining a full FoV. The placement of the cameras being inside of the build chamber

would put the optics at risk of metallisation in a real manufacturing system. Fringe projection from the literature have successfully placed cameras both inside the chamber using a protective casing [63] and externally with view windows installed to the chamber ceiling [61]. Either of these approaches can be taken once the system is ready to be used in a real additive manufacturing system.

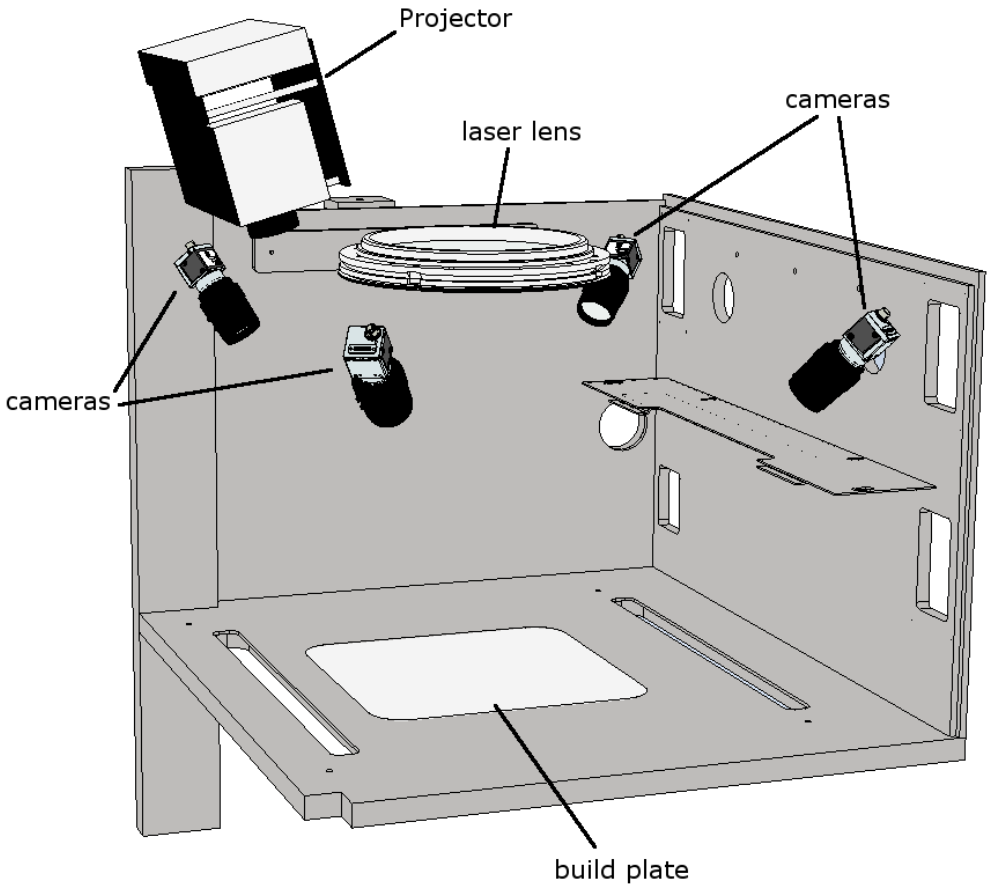

Figure 3.1.b. CAD model of the multi-view FP concept. In this design, four cameras are placed in the upper corners of the L-PBF chamber where they would be protected by an inner chamber casing with viewing windows. The projector is place externally, looking through a window in the top of the chamber.

It is worth noting that with the cameras in these positions, the camera's line of sight is not normal to the powder bed surface, which will result in a varying focus from the closest to farthest corner from the camera. For this system the cameras will be focussed on the centre of the powder bed region, creating the a central letterbox of in focus image per camera (from the left to right corners powder bed are, as later shown in Figure 3.3.b). As

there is a camera in each corner, this will result in there being 2 in focus cameras for each corner of the powder bed which will affect an affect on the quality of data in these regions. For the work presented throughout this thesis, the central region of the powder bed has been focussed on as this is typically where L-PBF components are most commonly built.

To meet the aim of this work, the multi-view FP system must achieve a spatial resolution that allows for identification of sub 500 µm features, such as those previously mentioned in section 2.4 over the (250 × 250) mm target measurement area. The system is being designed as an out-of-machine prototype with the spatial limitations of a currently existing commercial L-PBF system being considered.

3.2 Metrology lab prototype

A mock build chamber was designed and constructed out of aluminium extrude (CAD model in Figure 3.2.b) and PVC foamboard to mimic the spatial constraints of a Renishaw AM250 build chamber. A replica of the top panel of the build chamber was manufactured (Figure 3.2.a) to provide an entrance window for the projector, and a reference for where the laser lens and powder intake hopper are positioned as not to block them with the cameras when fixing them. The bench top system was built with black PVC and any gaps covered where possible using a black low reflectance foil to reduce any internal reflections and light pollution from the lab. A (265 × 265) mm measurement stage mimicking the build plate's size and location.

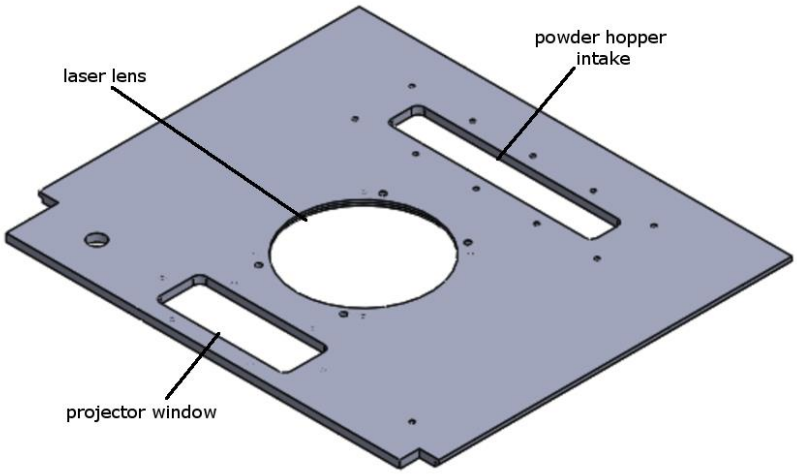

Figure 3.2.a. CAD of the top plate of a Renishaw AM250 L-PBF system used as a reference for hardware positioning.

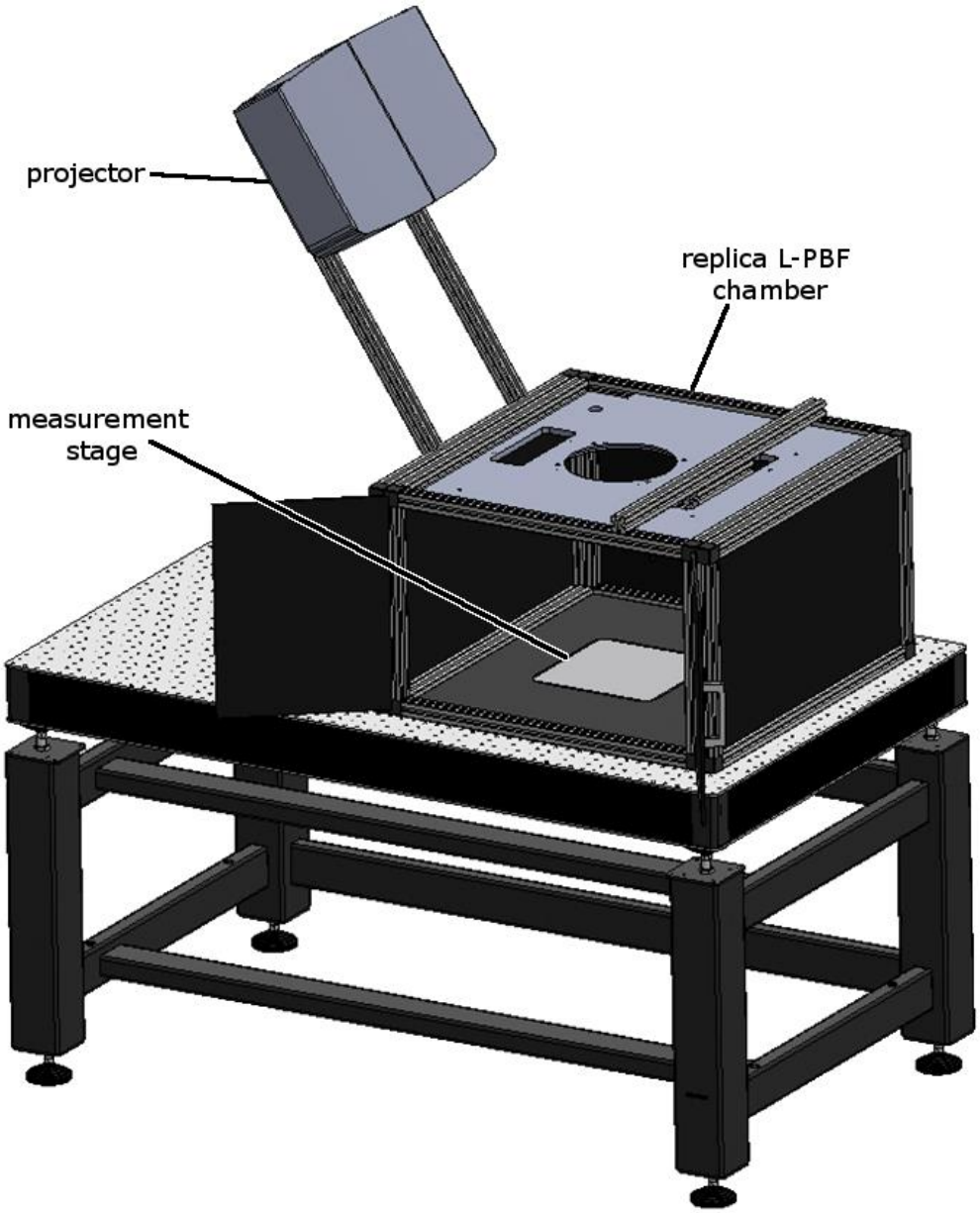

Figure 3.2.b. CAD model of lab system design. The measurement chamber is designed to mimic the dimensions of a Renishaw AM250 build chamber with the measurement stage positioned where the build plate would be. The top panel of the system is the top plate of the Renishaw build chamber.

3.2.1 Initial prototype system hardware

The first version of the multi-view FP system was comprised of four Canon digital single-lens reflex (DSLR) cameras (18 MP 3:2 sensor, stock lenses, framerate: 3 fps) and an Optoma UHD550X projector (pixel array: 3840 × 2160, maximum frame rate: 24 fps,

brightness: 2800 lm) fitted with a close-up lens attachment. Components were arranged to replicate the space limitations presented by a Renishaw AM250, with a (265 × 265) mm measurement stage mimicking the build plate's size and location. An image of the bench top setup can be seen in *Figure 3.2.c*.

Figure 3.2.c. Initial prototype of the multi-view FP system used for initial testing.

This system design can achieve a lateral projected pixel size of approximately 60 µm and the DSLR cameras have an equivalent pixel imaging size of approximately 50 µm on the powder bed per camera assuming the image plane is squared up to the power bed area. Assuming a minimum of 3 points are required to identify a feature on the surface, this would potentially allow for features as small as 150 µm to be identified using a single camera, ruling out the possibility of identifying weld tracks (nominally 100 µm in width) and smaller pores (down to 50 µm), but still allowing for larger features such as larger elongated pores, balling [25] and lattice deviations [26] (up to 500 µm) identifiable with a single camera system. Given that four cameras are being used, this should double the lateral sampling, making features down to 75 µm visible, potentially making unfused powder (100 µm to 150 µm) identifiable. As the cameras and projector are placed at an

angle to the powder bed, and are not square on, the actual projected pixel size will be slightly larger, and varying across the FoV.

3.2.2 Software

To characterise the positions of the projector and cameras in space, geometric characterisation software [222] has been used on the system using a high precision checkerboard pattern. The checkerboard is imaged in multiple positions with all cameras with and without fringes being projected onto the measurement area. This provides the intrinsic and extrinsic parameters of the cameras and projector allowing for a global reference frame to be made between all the devices so measurements are accurate coarsely aligned between the four sets of data acquired by the four cameras. The characterisation also accounts for any optical distortions in the lens so that these can be corrected for in the data sets.

Pre-existing FP code developed within the Manufacturing Metrology Team at the University of Nottingham was used on the multi-view FP system. The software used the geometric characterisation to create multiple point clouds form multiple perspectives that are pre-aligned and captured simultaneously [222]. The FP code projects 8 binary images, and 10-20 sinusoidal images at a range of frequencies to calculate a phase map of each camera's perspective. The phase map is then calculated as a function of height across the image for the point cloud to be generating during the phase unwrapping process. Control of the DSLRs was achieved using digiCamControl [223], an open source camera control software, which was triggered through a MATLAB [224] library for digiCamControl. The projector was controlled as a second monitor on the acquisition PC with full screen images being displayed to project the fringe images.

3.3 Initial data acquisition and analysis

3.3.1 Measurement technologies

To test the proposed multi-view FP system, measurements were made of the same sample using the FP system in its multi-view and single-view modes. A focus variation (FV) measurement was also taken of the sample to compare the FP measurements against a higher resolution system.

3.3.1.1 Fringe projection

Geometric characterisation of the system was performed using a calibrated chequerboard which was placed manually in multiple locations around the measurement volume [209]. Chequerboard locations were chosen to represent the region of interest within a real L-PBF system (a volume roughly (250 × 250 × 10) mm in size to cover the whole mock powder bed and a small vertical region). Images were captured in each position, both with and without projected fringes, to acquire the intrinsic and extrinsic parameters of all four cameras and the projector within a common global reference frame. The FP method used relies on a temporal phase unwrapping method that uses both phase-stepped sinusoidal fringes and varying frequency binary fringes to retrieve the absolute phase map. Further details of the geometric characterisation and the FP phase unwrapping methods are discussed in Shaheen et al. [209].

Eighteen images were captured per camera per measurement (eight binary images and ten sinusoidal images). The system operated as four separate camera-projector pairs, each outputting a point cloud of the measured surface. The four point clouds saved from a measurement cycle were initially coarsely aligned (due to the common reference frame), but required a further fine alignment process to create a combined, multi-view dataset. The projection covers the entire width and most of the length (approximately 190 mm) of the (265 × 265) mm measurement stage with the FoV of all four cameras covering the entire projected image. Point clouds were acquired with four samples in the measurement volume (shown in Figure 3.3.b.) with only the central sample, a Ti-64 additive manufactured flat, being used for analysis.

3.3.1.2 Focus variation microscopy

The FP results were compared against those from a commercial FV system [225]. The FV system has well-quantified metrological characteristics [226,227] and its resolving power is orders of magnitude higher than that of the FP system. The FV was used to measure the entire top surface of both samples using the following setup: 5× magnification objective lens (numerical aperture: 0.15, FoV: (2.82 × 2.82) mm, pixel sampling resolution: 3.52 µm), coaxial illumination, measured area: (12.5 × 12.5) mm, stitching of multiple FoVs performed in the manufacturer's software. Height maps of the

two samples from the FV system were acquired separately for each sample due to the FoV limitations of the FV system.

3.3.2 Sample

For the initial testing of the multi-view FP system, a (50 × 50) mm flat square of Ti-64 was manufactured using a Renishaw AM250 L-PBF system (image in Figure 3.3.a). For ease of orientation, a small piece of Blu Tack was placed on one corner of the sample. This corner was used as the RoI and was the only section measured by the FV system for comparison.

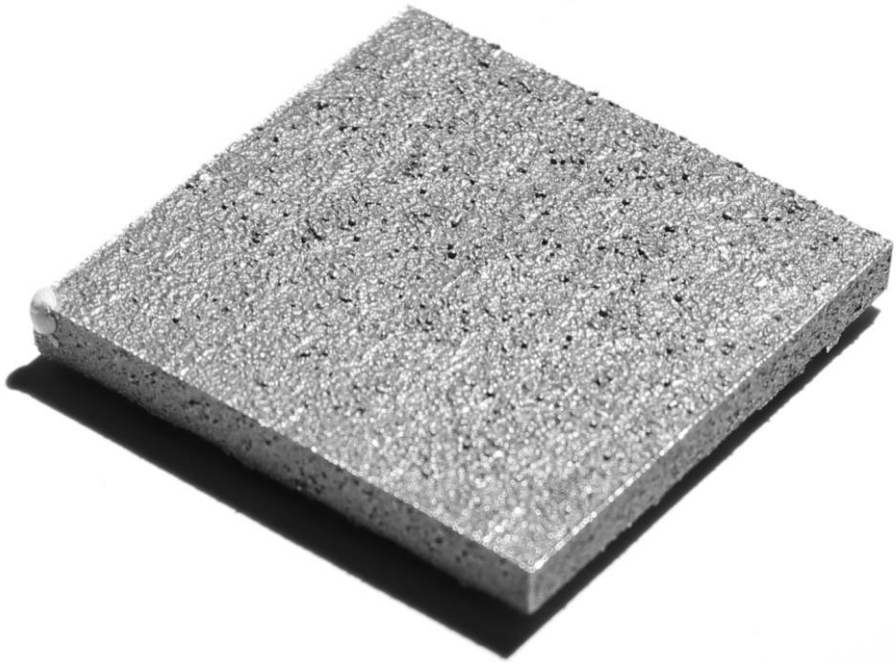

Figure 3.3.a Ti flat sample measured in the initial testing of the multi-view FP system. The sample is a (50 × 50) mm square of Ti-64 built in a Renishaw AM250 L-PBF.

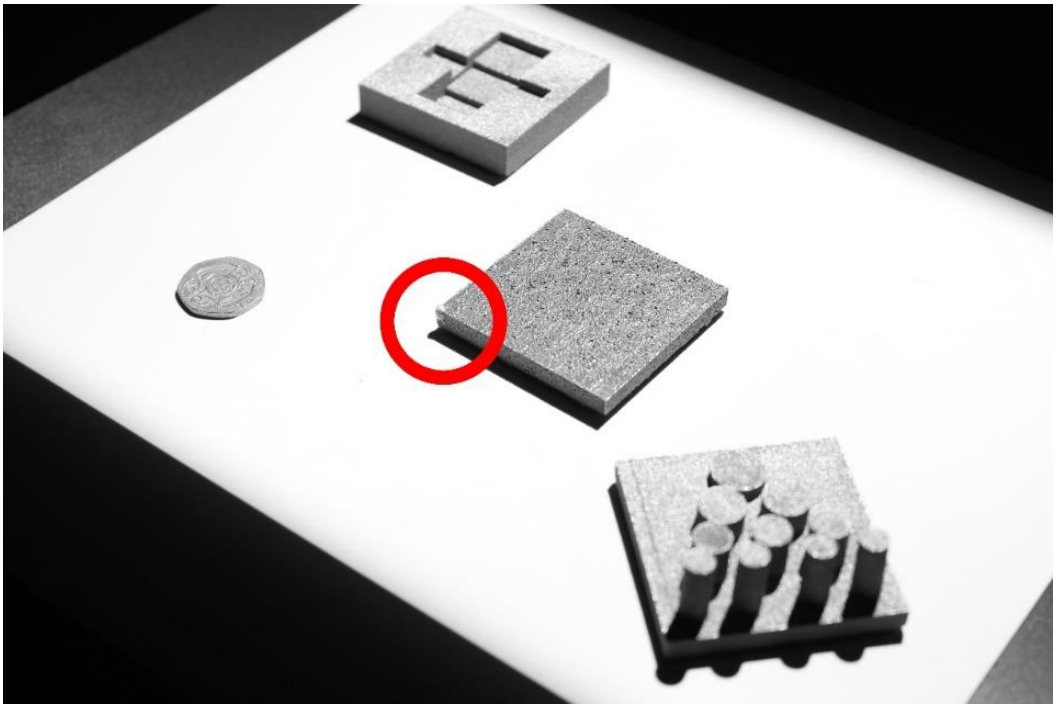

Figure 3.3.b. White image from single camera perspective when data was collected for multi-view DSLR testing of additive surfaces. Red circle shows RoI used for comparison.

3.3.3 Data processing

The raw data output from the FP and FV systems are point clouds (a 3D set of data points in space) and height maps (a collection of equispaced height points on a planar grid) formats respectively, with the FP FoV being multiple times larger than that of the FV system. To allow meaningful comparison, the two datasets were both cropped to only include the top surface of the ASMA4, and the FP data were converted to height maps (see section 3.3.3.3).

3.3.3.1 Fringe projection data

The point cloud generated from each camera was imported into CloudCompare 3D point cloud processing software [228], where it was cropped to only the region of the samples. A statistical outlier removal filter was applied (settings: number of points used for mean distance estimation = 8, standard deviations multiplier threshold (nσ) = 1, maximum point-to-point distance = mean distance + (nσ × standard deviation). Following the cropping and noise removal process, the point cloud was exported as an ASCII text file.

Each point cloud was imported into Polyworks|Inspector™[229], where they were further manually cropped to the RoI (In this case the corner of the Ti flat with a Blu Tack marker shown by a red circle in Figure 3.3.b). A two-phase alignment process (coarse and fine) was performed to align the individual camera FP point clouds to the FV measurements. The coarse alignment involved the manual selection of three common features between the target dataset (FP point cloud) and the reference data (FV triangulated mesh). After the coarse alignment, a fine alignment was performed using an iterative closest point (ICP) fitting algorithm [230–232]. The multi-view point cloud was constructed by fusing the independent point clouds of each camera into a single high-density dataset. For this experiment the point cloud from camera 3 was not included in the multi-view data due to a focussing issue with camera 3 when the data was acquired. All datasets of the RoI are exported in an ASCII text point cloud format, before being converted to a triangulated mesh in Polyworks|Inspector™ through a Delaunay triangulation algorithm [233] with a maximum edge length of 0.7 mm. The polygonal models are all exported in ".ply" format.

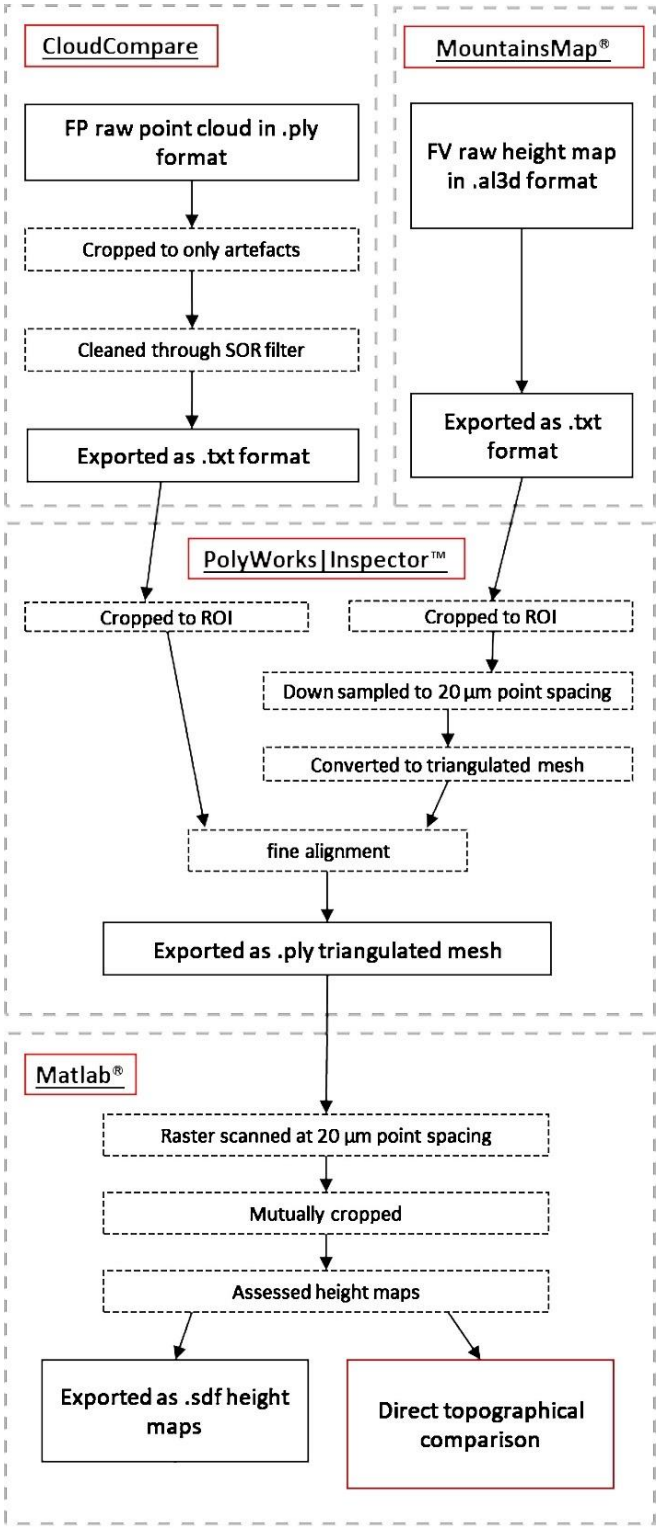

Figure 3.3.c. Data processing pipeline for both FP and FV measurements.

The ASCII point clouds of the FP RoIs are imported back into CloudCompare, where an approximate mean point spacing is calculated.

3.3.3.2 Focus variation data

Height maps from the FV system were imported into Polyworks|Inspector™, downsampled to a 20 µm point spacing through linear interpolation, and converted into triangulated meshes using the same method outlined for the FP point clouds in section 3.3.3.1.

3.3.3.3 Data set comparisons

A recently developed method [234] of point-by-point topography comparison that creates equi-point-spaced height maps of pre-aligned triangulated meshes was used for the FP and FV datasets to be compared in a meaningful manner. Polygonal models of both samples are converted into height maps by virtual raster scanning [234–236] (a method of interpolating the polygonal model into a uniform grid by rastering along the XY plane) with a 20 µm point spacing. The height maps are equivalently cropped before comparison.

Point-by-point deviations in height between the FP and FV were mapped and the mean absolute deviation over the surface was calculated to provide a mean deviation which functions as a measure of the measurement accuracy (under the assumption that the FV measurement is a reference representation of the surface).

Average point spacing of the multi-view and single-view FP point clouds are compared to act as an indicator of the system's potential resolving capabilities. Point spacing is not synonymous with resolution, as the resolving power of a system describes the distance at which two features can be differentiated. However, a higher point density should result in an improved resolving capability due to an increased number of measured points per feature, assuming that the points are approximately equi-spaced over the measurement area and no aliasing is present.

3.4 Initial results and discussion

3.4.1 TI flat data

Height maps of the FV and different FP measurements are presented in Figure 3.4.a for the Ti flat sample, with deviation maps relative to the FV measurement presented in Figure 3.4.b.

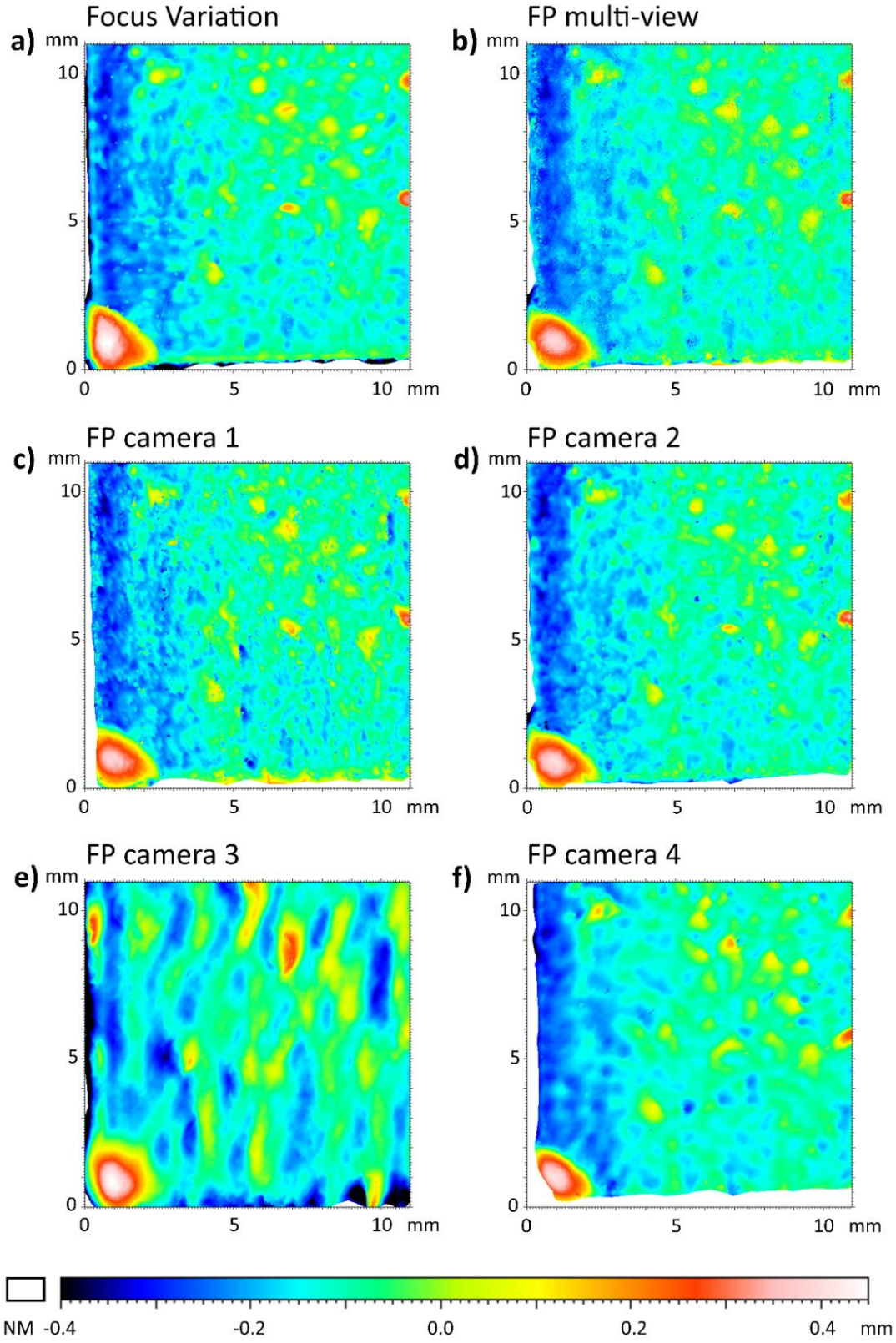

Figure 3.4.a Aligned height maps of the Ti flat RoI from a) FV, b) multi-view FP (omitting cameras 3), c) FP camera 1, d) FP camera 2, e) FP camera 3, f) FP camera 4.

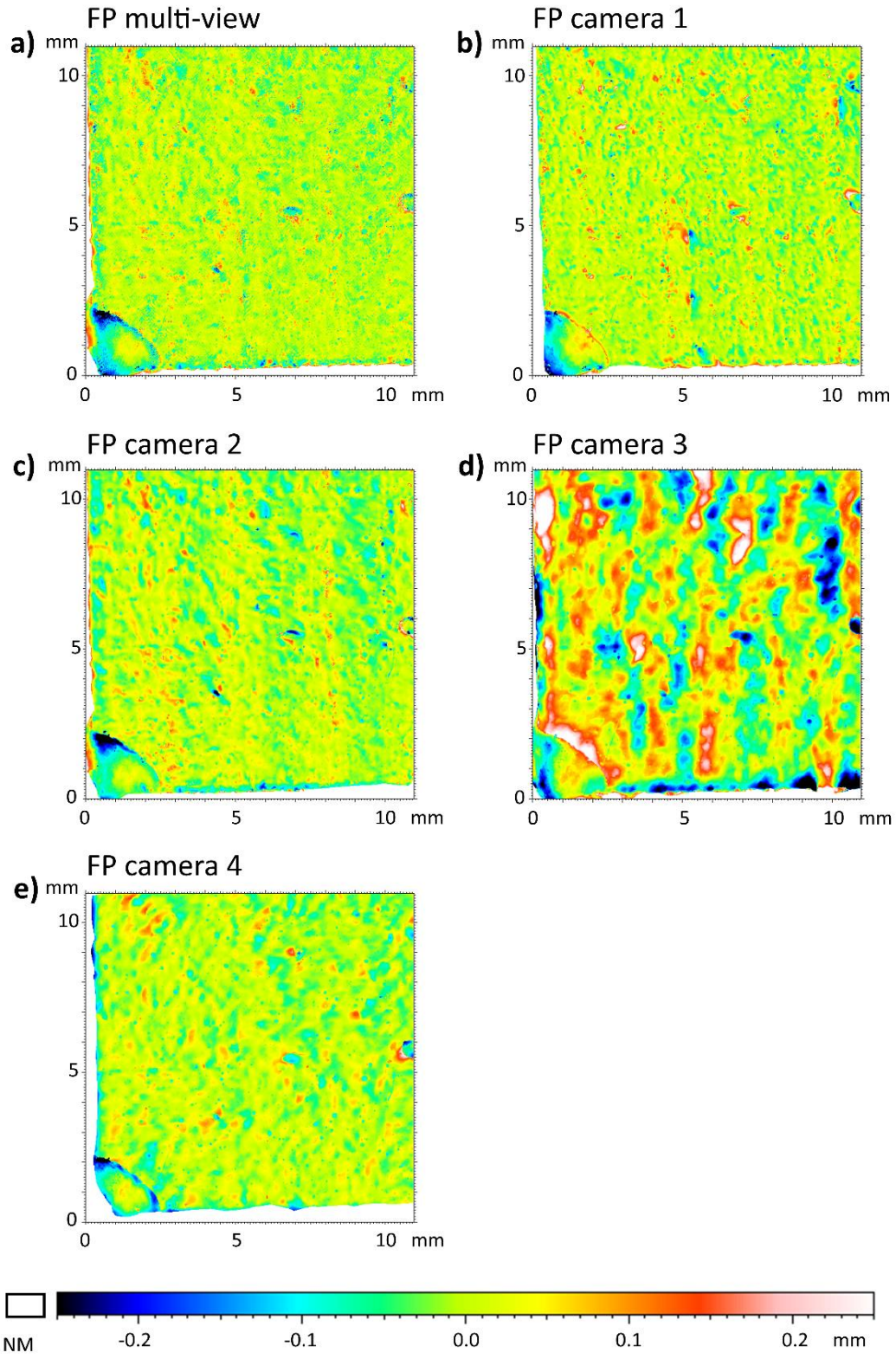

Figure 3.4.b Deviation maps when compared to the FV measurement for a) multi-view FP (omitting camera 3), b) FP camera 1, c) FP camera 2, d) FP camera 3, e) FP camera 4.

Out of the four point clouds collected by the system, data from camera 3 showed high levels of waviness due to a focussing error in the set up. As a result of this set up error, only cameras 1, 2 and 4 were used in the multi-view FP data set rather than all four cameras. Mean and max deviation from the FV measurement, and the mean point spacing of the raw point clouds are given in Table 2 for both the multi-view and all single camera FP measurements.

Table 2. Max deviations, mean deviations of the FP height maps when compared to the FV data, and point spacing of the raw FP point clouds.

	Multi-view FP	**Single-view FP**			
		Cam 1	Cam 2	Cam 3	Cam 4
Max deviation/µm	694.2	694.2	731.1	711.3	389.4
Mean deviation/µm	25.6	25.7	28.4	69.4	25.7
Point spacing/µm	59.15	91.56	101.24	113.18	97.20

Maximum deviations of the multi-view and single-view FP data form the FV data remains roughly consistent at around 700 µm except for the single-view data from camera 4. The lower maximum deviation from camera 4 is a result of camera 4 not gaining full coverage of the RoI, as seen In Figure 3.4.b and Figure 3.4.c where the bottom and left edges have missing regions. These missing regions are where the most severe deviations occur. The mean deviations of cameras 1, 2 and 4 are also approximately the same as the multi-view data, with a minor improvement of 0.1 µm which is arguably negligible. The multi-view FP point cloud (pre-meshing and raster scanning) has a mean point spacing of 59.15 µm, with the single camera approach having 96.67 µm (averaged from cameras 1, 2 and 4), resulting in a point density that is 2.67 times higher when using the multi-view approach over an area measurement. For metal PBF defects, such as elongated pores (typical size: 50 µm to 500 µm) and unfused powder (typical size: 100 µm to 150 µm) [237] the higher point spacing could make the difference between the features being resolvable or not due to multiple measured points covering the same feature. In Figure 3.4.c, A single surface feature is compared between the FV, multi-view FP, and the single-view FP data which qualitatively shows the resolving limits of a single camera approach. The single-view data has regions of data drop that are not present in the multi-view data, resulting in the multi-

view data measuring the feature, and its surrounding areas, far more comparably to the FV measurement.

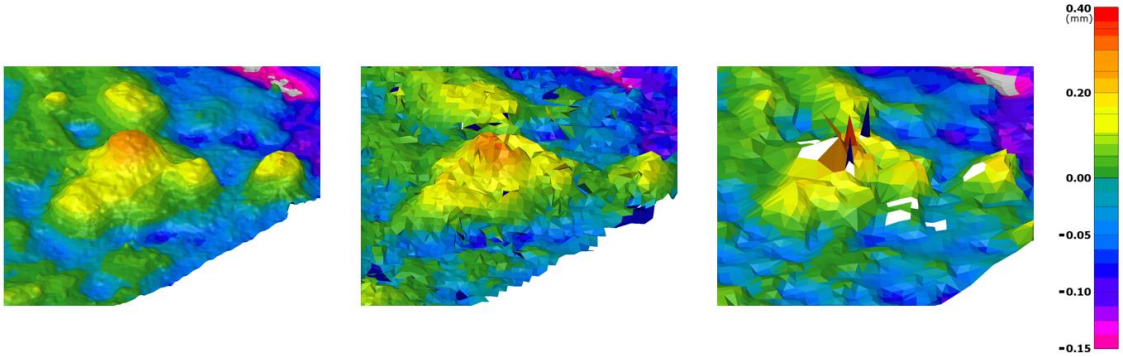

Figure 3.4.c. Close up view of a single surface feature from the Ti flat sample. (From left to right) FV, 3 view FP, and single-view FP.

3.4.2 Concluding remarks from initial prototype

In this chapter, an in-situ monitoring system for metal PBF systems has been designed that uses multi-view FP to measure topography over a large percentage of the build area. To test this design, an out-of-machine prototype has been built using commercially available cameras and projector within the spatial limitations of a real PBF machine. A L-PBF manufactured sample has been measured using both the prototype multi-view FP system an initial test for the systems capabilities, with comparisons being made against a higher resolution FV measurement to assess the accuracy. This initial measurement data gave the following results:

- A multi-view FP system is capable of measuring additive surfaces with results that do not largely differ from the FV data (mean deviations of 25.6 µm across the surface)
- A higher potential lateral resolution is achievable through a higher density point cloud and that individual features can be more clearly resolved when compared to single-view FP data
- Multi-view FP provides a level of measurement redundancy meaning that if one of the camera's provides insufficient or unreliable data, either in a specific region of the surface or over the entire measurement, then the data taken from the other cameras can still be used

3.4.2.1 Remaining issues from the initial prototype

Issues with version 1 of the system became apparent over the testing period. The Canon DSLRs requiring third party software control resulting in extremely slow capture times as the software could not be accurately synchronised with the projector. To ensure that the slow communication between Matlab [224] and digiCamControl [223] large delays had to be introduced to the measurement software, making the system ill-suited for any in-process application because of the additional time that would be added to the built process. This long acquisition time also resulted in the geometric characterisation becoming a full day task due to the repeat moving and recapturing of the checkerboard pattern throughout the measurement volume. Communication issues between Matlab [224] and digiCamControl [223] became a further issue during the characterisation program as the digiCamControl software was prone to crashing during prolonged runtime. When digiCamControl would crash, the FP characterisation software would fail and require the characterisation process to be started over again with all the checkerboard positions repeated, effectively making the characterisation process a game of chance as to whether it could be completed within a day ready to take measurements.

Aside from the software issues found when operating the cameras, the DSLRs were also deemed unsuited to in-process measurement due to their size and internal software. In a real AM chamber, smaller more robust sensors would be required to minimise the impact on the L-PBF machines performance. The maximum frame rate of the DSLRs used is 3 fps, which for an 18 image measurement would result in a shortest possible acquisition time of 6 seconds. If a measurement was to be taken for every layer of a hypothetical build, 6 additional second per layer could accumulate to hours of delay on a build that utilises the machines whole chamber height. To reduce dead time in the build process and to reduce the volume of the hardware, higher frame rate industrial machine vision cameras could be implemented.

4 System repeatability

As discussed in the previous chapter, an in-process monitoring system must take the following considerations into account to ensure that it's suitable for use in a real manufacturing machine:

1. The impact on manufacturing times that the measurement system may have.
2. The resolving capabilities and range limitations of the chosen method.
3. The spatial limitations of the PBF chamber.
4. The environmental conditions of the build chamber.

Work presented in chapter 3 showed that the resolving capabilities of a multi-view FP system were potentially good enough to allow for in-process additive defects to be measured, with mean deviations from FV data being 25.6 µm across the samples surface and a mean point spacing of 59.15 µm. However, the cameras used for this version of the system would not be suitable for build chamber conditions, measuring time constraints, or the spatial limitations of a commercially manufacturing L-PBF machine. The Canon DSLRs used in the initial prototype are designed for consumer photography rather than industrial machine vision applications and therefore are not as compact and stable as what would be ideal, with a maximum frame rate of 3 fps.

To address the issues outlined in chapter 3 with the initial prototype, the multi-view FP system has been modified to operate with machine vision cameras. With the new hardware changes, the system has been tested to assess the measurement repeatability of some additively manufactured metrology samples, with the results again compared to FV variation data as a standard. Results are presented from the newly modified prototype PBF chamber to compare the performance differences between a single camera and the multi-view FP system for on-machine monitoring applications.

4.1 Changes to the multi-view fringe projection system

To address the issues caused by the current cameras lack of suitability for an in-process system, the DSLRs have were replaced by Basler ace acA5472-17um cameras. The Basler cameras have a comparable pixel array size of 5472 × 3648 compared to the Canon DSLRs 5184 × 3456 pixel array, with a monochrome sensor. The Basler cameras also

have a maximum framerate of 17fps, meaning that all of the 18 images required to collect FP data could be captures in ~1 second rather than the 6 seconds limit imposed by the DSLRs tested previously. The use of industrial machine vision cameras also allows for digiCamControl [223] to be bypassed in favour of Matlab's [224] native machine vision capabilities. Removing digiCamControl from the capture software eliminates the frequent crashing and additional time delays seen from digiCamControl when communicating with Matlab. The reconfigured benchtop prototype with the new Basler cameras can be seen in Figure 4.2.a. The more compact form factor of the machine vision cameras also makes them better suited for fitting in an additive machine without impacting the machines operating capabilities.

4.2 Repeatability testing methodology

4.2.1 Measurement technologies

To test the proposed multi-view FP system, measurements were made of the same samples using the FP system in its multi-view and single-view modes. FV measurements were also taken of the samples to compare the FP measurements against a higher resolution system.

4.2.1.1 Fringe projection updated hardware

The modified multi-view FP system is comprised of four Basler ace acA5472-17um cameras (pixel array: 5472 × 3648, sensor size: (13.1 × 8.8) mm, maximum frame rate: 17 fps), each fitted with a MVL16M1 16 mm focal length lens, and the same Optoma UHD550X projector (pixel array: 3840 × 2160, maximum frame rate: 24 fps, brightness: 2800 lm) as before, fitted with a close-up lens attachment. Components were arranged within the same frame as before to replicate the space limitations presented by a Renishaw AM250, with the same (265 × 265) mm measurement stage mimicking the build plate's size and location. Images of the bench top setup can be seen in Figure 4.2.a.

Geometric characterisation of the system was again performed using a calibrated chequerboard which was placed manually in multiple locations around the measurement volume [209]. Images were captured in each position, both with and without projected fringes, to acquire the intrinsic and extrinsic parameters of all four cameras and the projector within a common global reference frame. The FP method used relies on a

temporal phase unwrapping method that uses both phase-stepped sinusoidal fringes and varying frequency binary fringes to retrieve the absolute phase map. Further details of the geometric characterisation and the FP phase unwrapping methods are discussed in Shaheen et al. [209].

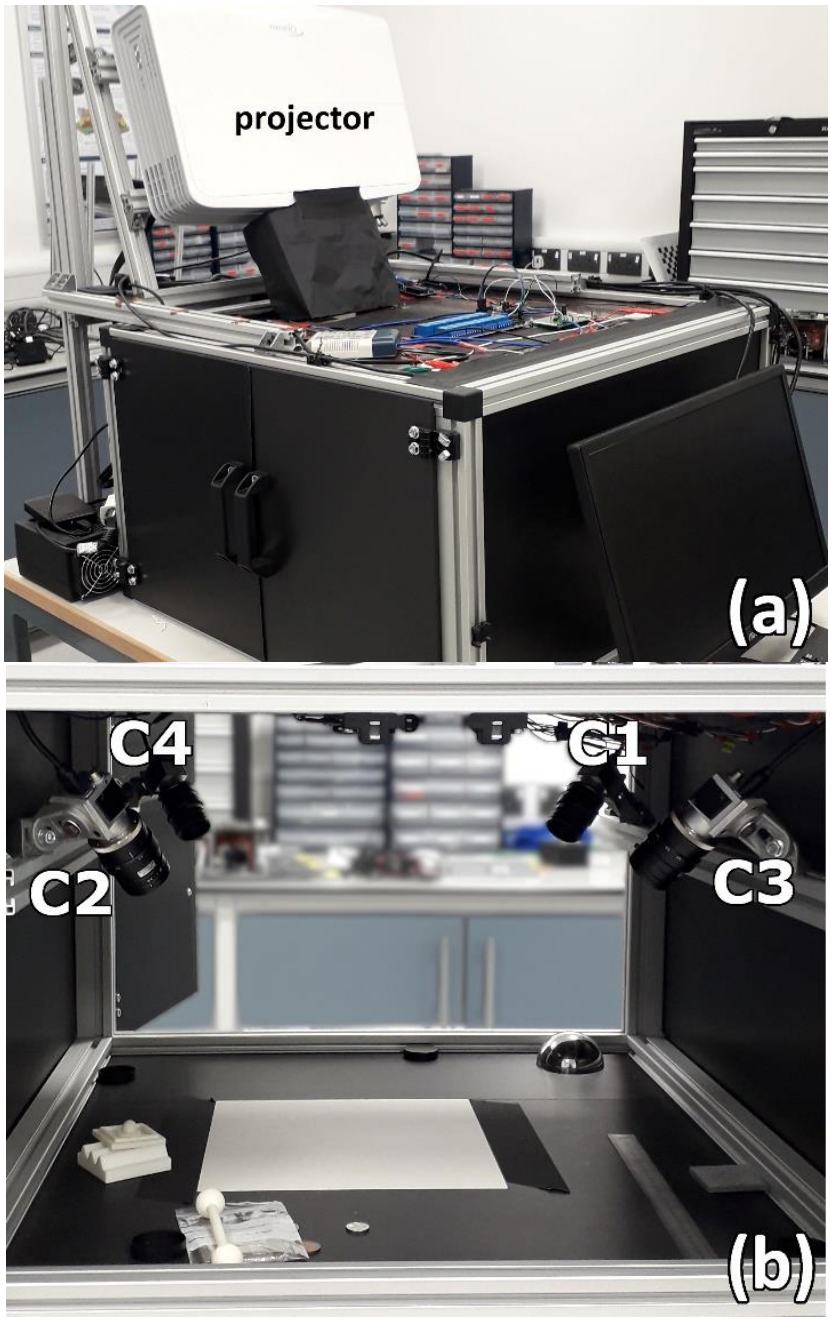

Figure 4.2.a. Multi-view FP system. (a) External view of FP system with projector labelled. (b) Inside measurement chamber with the mock powder bed region (250 mm × 250 mm) and four cameras (labelled C1 to C4).

Eighteen images were captured per camera per measurement (eight binary images and ten sinusoidal images). The system operated as four separate camera-projector pairs, each outputting a point cloud of the measured surface. The four point clouds saved from a measurement cycle were initially coarsely aligned (due to the common reference frame), but required a further fine alignment process to create a combined, multi-view dataset (described in section 3.3.3.1). The projection covers the entire width and most of the length (approximately 190 mm) of the (265 × 265) mm measurement stage with the FoV of all four cameras covering the entire projected image. Point clouds were acquired with both samples (described in section 3.3.2) in the same measurement volume. Sample positioning is shown in Figure 4.2.d.

4.2.1.2 Focus variation microscopy

The FP results were compared against those from a commercial FV system [225]. The FV system has well-quantified metrological characteristics [226,227] and its resolving power is orders of magnitude higher than that of the FP system. The FV was used to measure the entire top surface of both samples using the following setup: 5× magnification objective lens, (numerical aperture: 0.15, FoV: (2.82 × 2.82) mm, pixel sampling resolution: 3.52 µm), coaxial illumination, measured area: (25 × 25) mm, stitching of multiple FoVs performed in the manufacturer's software. Height maps of the two samples from the FV system were acquired separately for each sample due to the FoV limitations of the FV system.

4.2.2 Samples

Two AM surface samples that were designed and manufactured by Townsend et al. using an ARCAM Q10 EB-PBF system and a Renishaw AM250 L-PBF system [29] were used as samples for all measurements. The ASMA4 samples include three sections, each with a constant amplitude and decreasing wavelength sine-wave structure along the section length. Both samples were manufactured with the measured plane of the structured surface orthogonal to the build direction (see Figure 4.2.b). The use of these samples over one more representative of a L-PBF powder bed in is to identify at which spatial frequencies the fringe projection system has difficulty resolving the features.

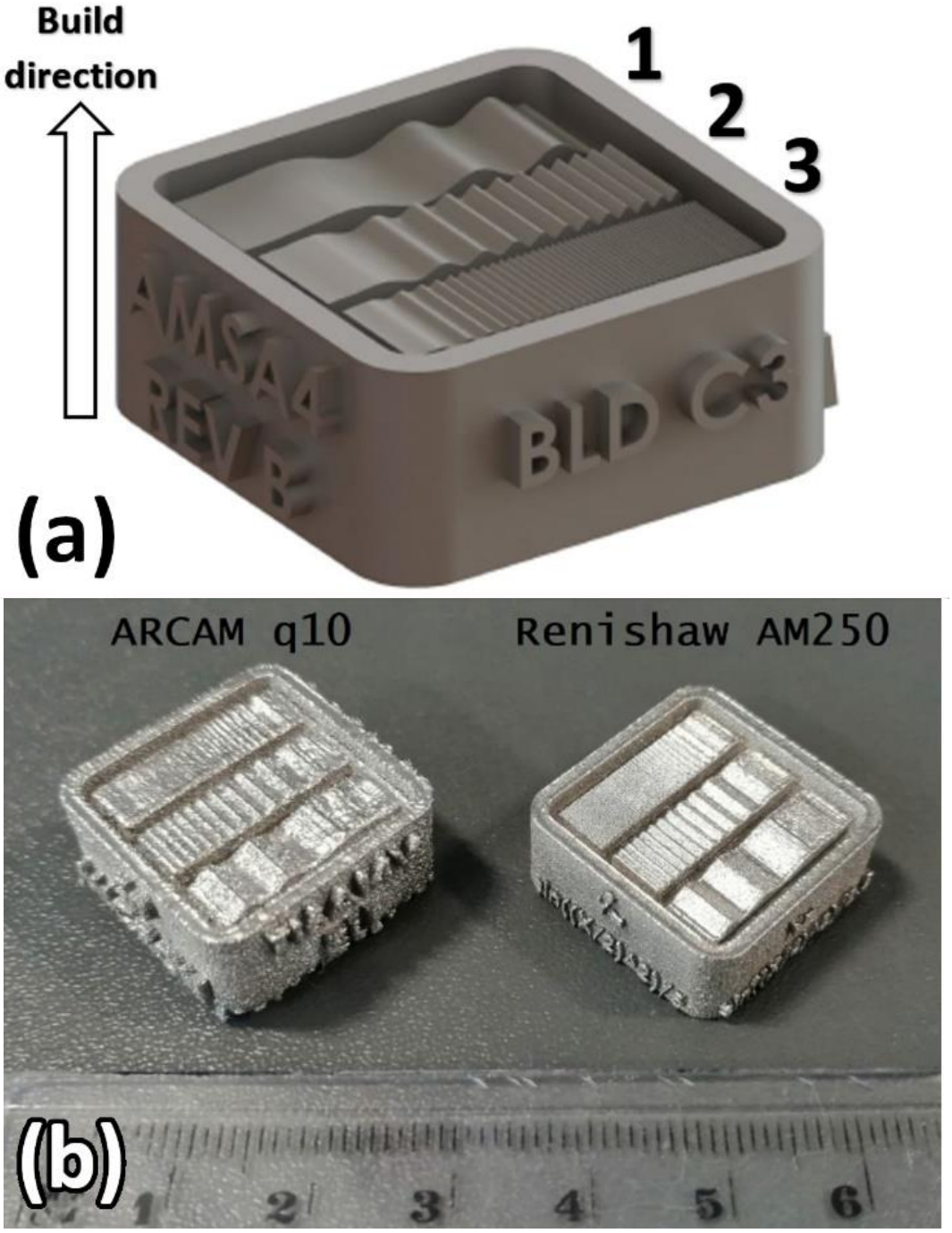

Figure 4.2.b. (a) CAD model the AMSA4 (modified from Townsend et al. [29]) with three sections labelled in correspondence to Table 3. (b) Photograph of the two AMSA4 samples, manufactured using EB-PBF (left) and L-PBF (right) against a ruler for scale (numbered divisions in centimetres).

For all measurements, the RoI was the top surfaces of the three 17 mm × 5 mm structured sections. The equations for the nominal structure of each section are given in Table 3,

with the accuracy achieved in the manufacturing of the samples reported in Townsend et al. [29]. All data presented is exclusively of the three structured top sections.

Table 3. The equations of the CAD models for the three structured sections of the AMSA4 [29], labelled in Figure 4.2.b(a), where *Y* is the amplitude and *X* is the distance along the section in millimetres.

Section number	Amplitude/ µm	Structure equation/mm
1	400	$Y = \frac{\sin\left(\frac{X^2}{16}\right)}{2.5}$
2	200	$Y = \frac{\sin\left(\frac{X^2}{4}\right)}{5}$
3	100	$Y = \frac{\sin(X^2)}{10}$

4.2.3 Data processing

The raw data output from the FP and FV systems are point clouds (a 3D set of data points in space) and height maps (a collection of equispaced height points on a planar grid) formats respectively, with the FP FoV being multiple times larger than that of the FV system. To allow meaningful comparison, the two datasets were both cropped to only include the top surface of the ASMA4, and the FP data were converted to height maps (see section 3.3.3.3). Five repeat measurements, as deemed sufficient for estimating uncertainty by NPL's Good Practice Guide No. 11 [238], were made on the single and multi-view FP systems and the FV system without repositioning the sample, so that a statistical measure of repeatability could be estimated. A schema of the data processing pipeline is shown in Figure 3.3.c and detailed explanations of this pipeline follow throughout this section.

4.2.3.1 Fringe projection data

The point cloud generated from each camera was imported into CloudCompare 3D point cloud processing software [228], where it was cropped to the region of the samples. A statistical outlier removal filter was applied (settings: number of points used for mean distance estimation = 8, standard deviations multiplier threshold (nσ) = 1, maximum point-to-point distance = mean distance + (nσ × standard deviation). Following the cropping and noise removal process, the point cloud was exported as an ASCII text file.

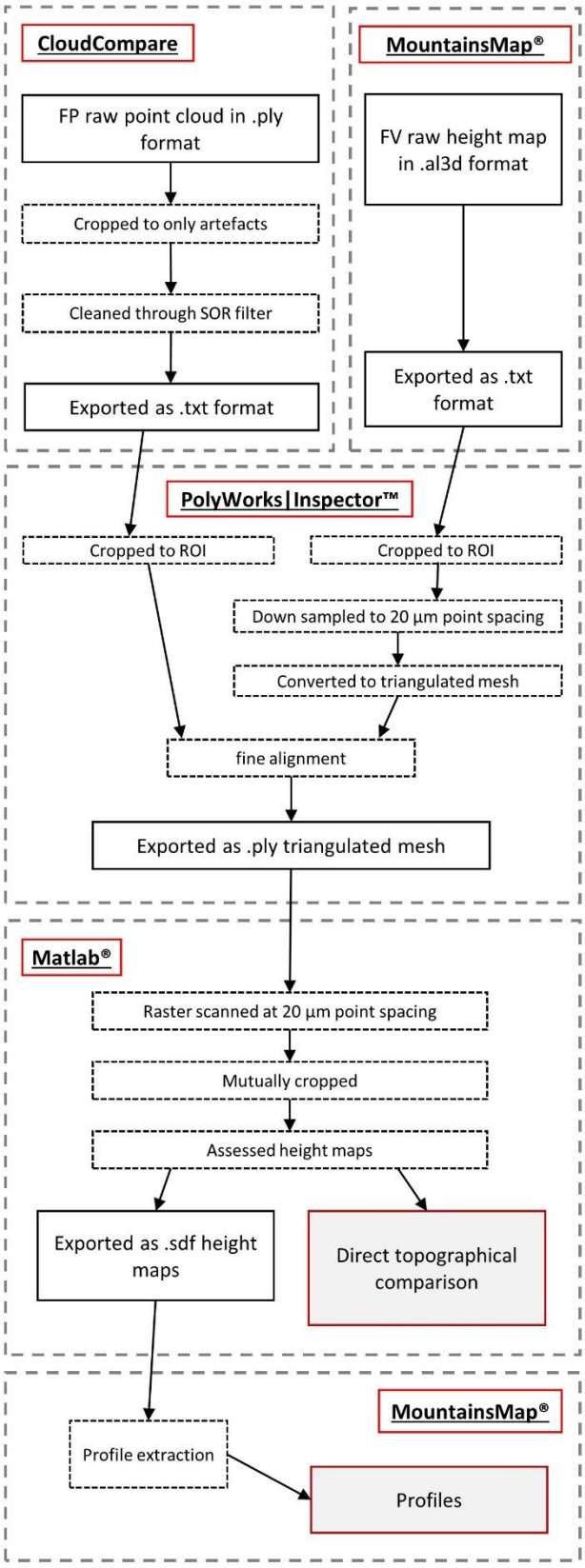

Figure 4.2.c. Data processing pipeline for both FP and FV measurements.

Each point cloud was imported into Polyworks|Inspector™[229], where they were further manually cropped to the RoI. A two-phase alignment process (coarse and fine) was performed to align the individual camera FP point clouds to the FV measurements. The coarse alignment involved the manual selection of three common features between the target dataset (FP point cloud) and the reference data (FV triangulated mesh). After the coarse alignment, a fine alignment was performed using an ICP fitting algorithm [230–232]. During alignment, repeat measurements acquired using the same camera were fixed in space relative to one another to ensure that repeatability calculations were not influenced by geometric transformations. The multi-view point cloud was constructed by fusing the independent point clouds of each camera into a single high-density dataset. All datasets of the RoI are exported in an ASCII text point cloud format, before being converted to a triangulated mesh in Polyworks|Inspector™ through a Delaunay triangulation algorithm [233] with a maximum edge length of 0.7 mm. The polygonal models are all exported in ".ply" format. The ASCII point clouds of the FP RoIs are imported back into CloudCompare, where an approximate mean point spacing is calculated.

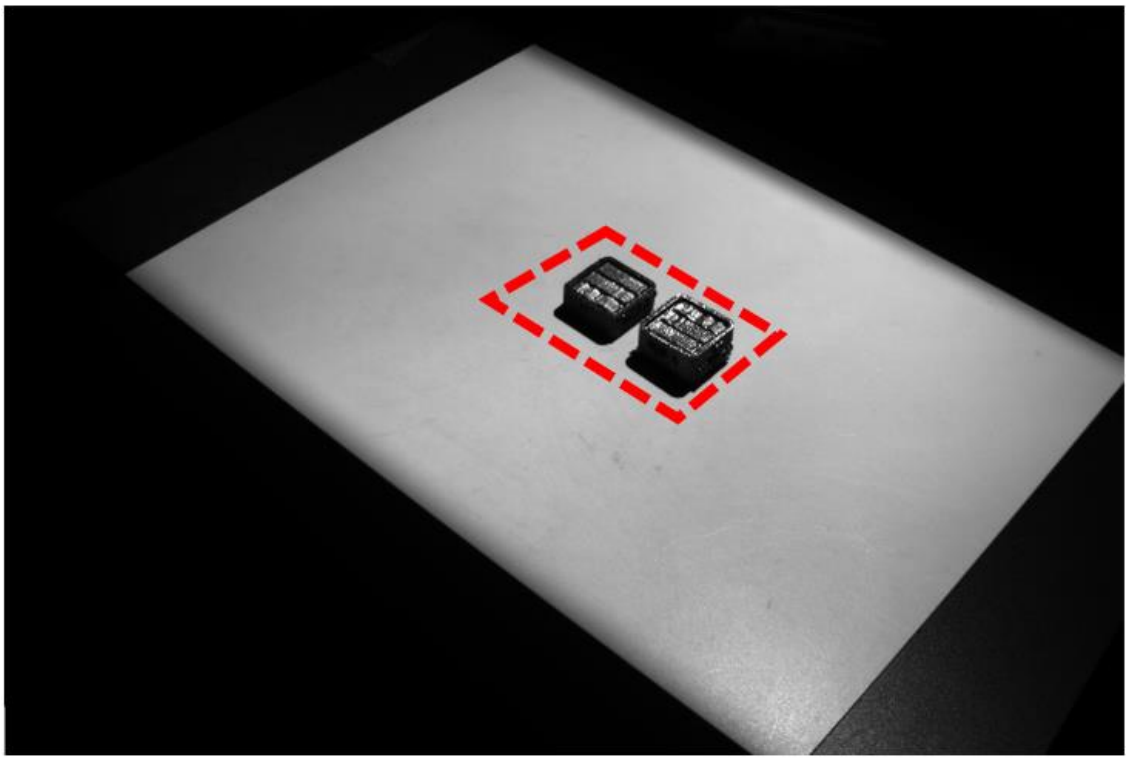

Figure 4.2.d. White image of both AMSA4 samples within the measurement volume of the FP system from the perspective of camera 1. Red box marks the region of initial cropping.

4.2.3.2 Focus variation data

Height maps from the FV system were imported into Polyworks|Inspector™, downsampled to a 20 µm point spacing through linear interpolation, and converted into triangulated meshes using the same method outlined for the FP point clouds in section 3.3.3.1.

4.2.3.3 Data set comparisons

A recently developed method [234] of point-by-point topography comparison that creates equi-point-spaced height maps of pre-aligned triangulated meshes was used for the FP and FV datasets to be compared in a meaningful manner. Polygonal models of both samples are converted into height maps by virtual raster scanning [234–236] with a 20 µm point spacing. The height maps are equivalently cropped before a mean *z*-value for each measurement point is calculated with a corresponding 95% confidence interval (CI), providing a measure of the measurement precision.

Point-by-point deviations in height between the FP and FV were mapped and the mean absolute deviation over the surface was calculated to provide a mean deviation which functions as a measure of the measurement accuracy (under the assumption that the FV measurement is a reference representation of the surface). Discrepancies between measurement methods are also mapped to present where the different methods disagree on the height position of each point. Discrepancy is defined here as the negative output from a binary measure that states where the CI width of the FP and FV height values do or do not overlap with one another, therefore, its value is dependent on both the magnitude of deviation and the CI width. Discrepancy as a percentage over the surface provides a measure of how well two measurement methods agree with one another.

Point spacings of the multi-view and single-view FP point clouds are compared to act as an indicator of the system's potential resolving capabilities. As previously stated in section 3.3.3.3, it is worth noting that point spacing is not synonymous with resolution. However, higher point density would result in an improved resolving capability due to an increased number of measured points per feature.

Profiles were extracted along the centre of each structured section from the aligned datasets using MountainsMap®[239]. The profiles serve as a visual representation of the surface form that outline some effects of using multi-view over single-view FP.

4.3 Results and discussion

4.3.1 Focus variation measurements

Height maps and associated CI widths of the FV measurements are presented in Figure 4.3.a for both L-PBF and EB-PBF samples. Mean CI widths for the FV measurements were calculated to be 10 μm and 27 μm for the EB-PBF and L-PBF samples, respectively. The higher mean CI width value for the L-PBF sample is likely a result of the high slope angles as the structured surface tends towards the highest spatial frequencies [240]. On the EB-PBF sample, these high aspect ratio features are not present due to the resolution limits of the EB-PBF system in manufacturing.

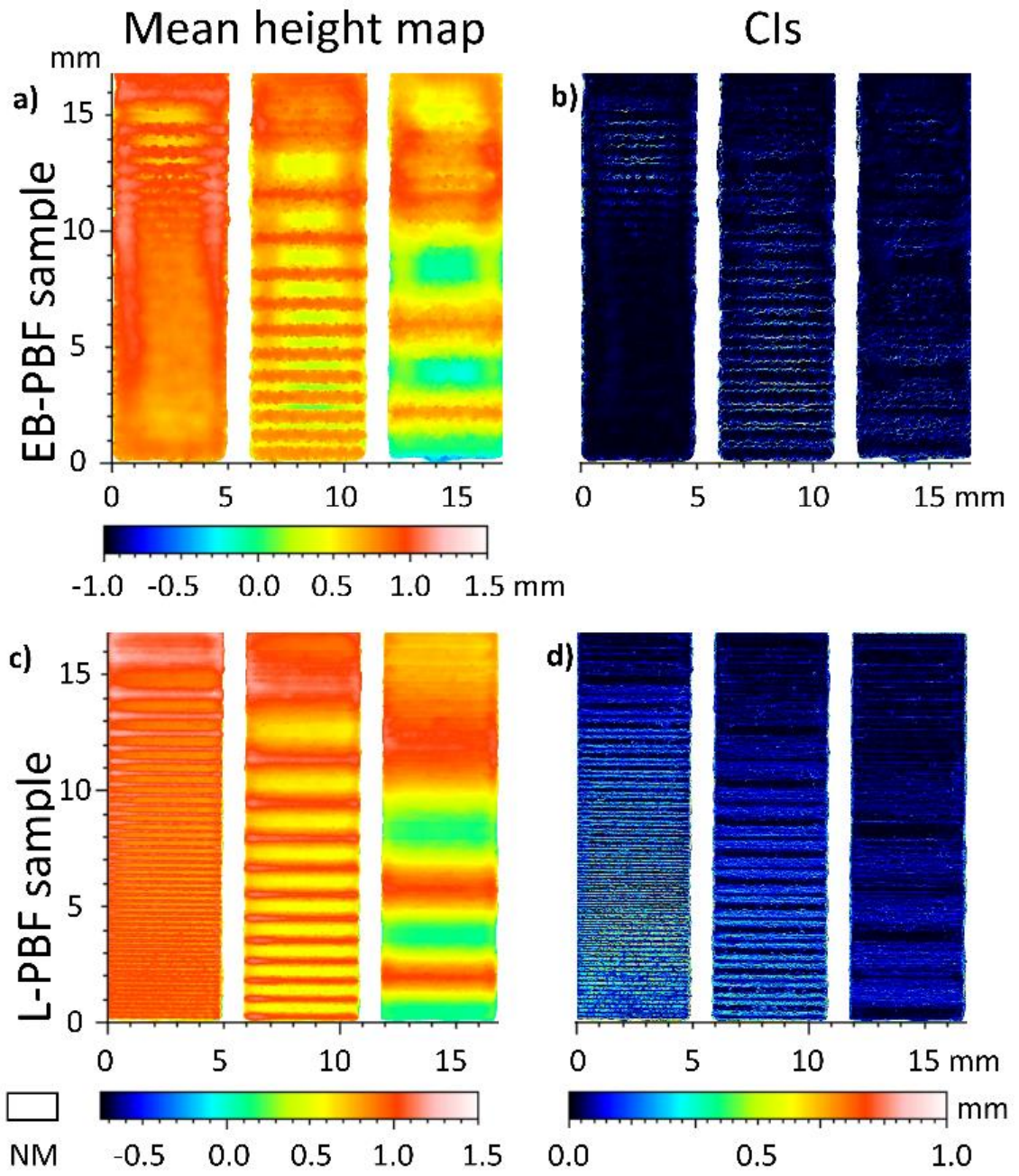

Figure 4.3.a. Mean height maps (a and c) and CI maps (b and d) for the FV measurements of both the EB-PBF and L-PBF sample. Both CI plots are set to the same colour bar; all saturated values exceed colour bar scale.

4.3.2 Fringe projection measurements

4.3.2.1 Surface coverage

To assess the impact on data dropout over the measured surface, a percentage of surface overlap between the FP and FV datasets is calculated (values presented in Table 4 and

Table 5). For both samples, the percentage of overlap on the measured surfaces is higher when multi-view is used, with some single-views losing as much as 10% of the overall surface data. Height maps presented in Figure 4.3.b and Figure 4.3.c of the FP data have regions of missing data from all individual cameras that are much less prevalent in the multi-view reconstruction, although there are cases where a single-view perspective covers the majority of the surface, achieving surface coverage of up to 97.9%, the multi-view system still improves upon this, covering 99.5% of the surface for the same sample (L-PBF sample). High coverage of the single-view method is also not consistent across the entire measurement volume. In Figure 4.3.c (d), where 97.8% surface coverage was achieved of the L-PBF sample, the same camera only achieved 93.0% surface coverage of the EB-PBF sample, where the multi-view method was able to cover 98.7%.

Table 4. Discrepancy (percentage point-by-point disagreement), surface overlap (percentage of data surface coverage) and mean deviation (point-by-point difference is height value) between FP and FV height maps of the EB-PBF sample.

EB-PBF Data set	**Multi-view FP**	**Single-view FP**			
		Cam1	Cam2	Cam3	Cam4
Discrepancy from FV /%	51.1	81.7	83.8	81.5	78.1
Surface overlap from FV /%	98.7	97.5	88.3	93.0	90.6
Mean deviation from FV /μm	67	83	92	77	81

Table 5. Discrepancy (percentage point-by-point disagreement), surface overlap (percentage of data surface coverage) and mean deviation (point-by-point difference is height value) between FP and FV height maps of the L-PBF sample.

L-PBF Data set	**Multi-view FP**	**Single-view FP**			
		Cam1	Cam2	Cam3	Cam4
Discrepancy from FV /%	49.9	78.9	75.4	78.2	73.2
Surface overlap from FV /%	99.5	97.9	90.3	97.8	88.2
Mean deviation from FV /μm	69	93	85	79	82

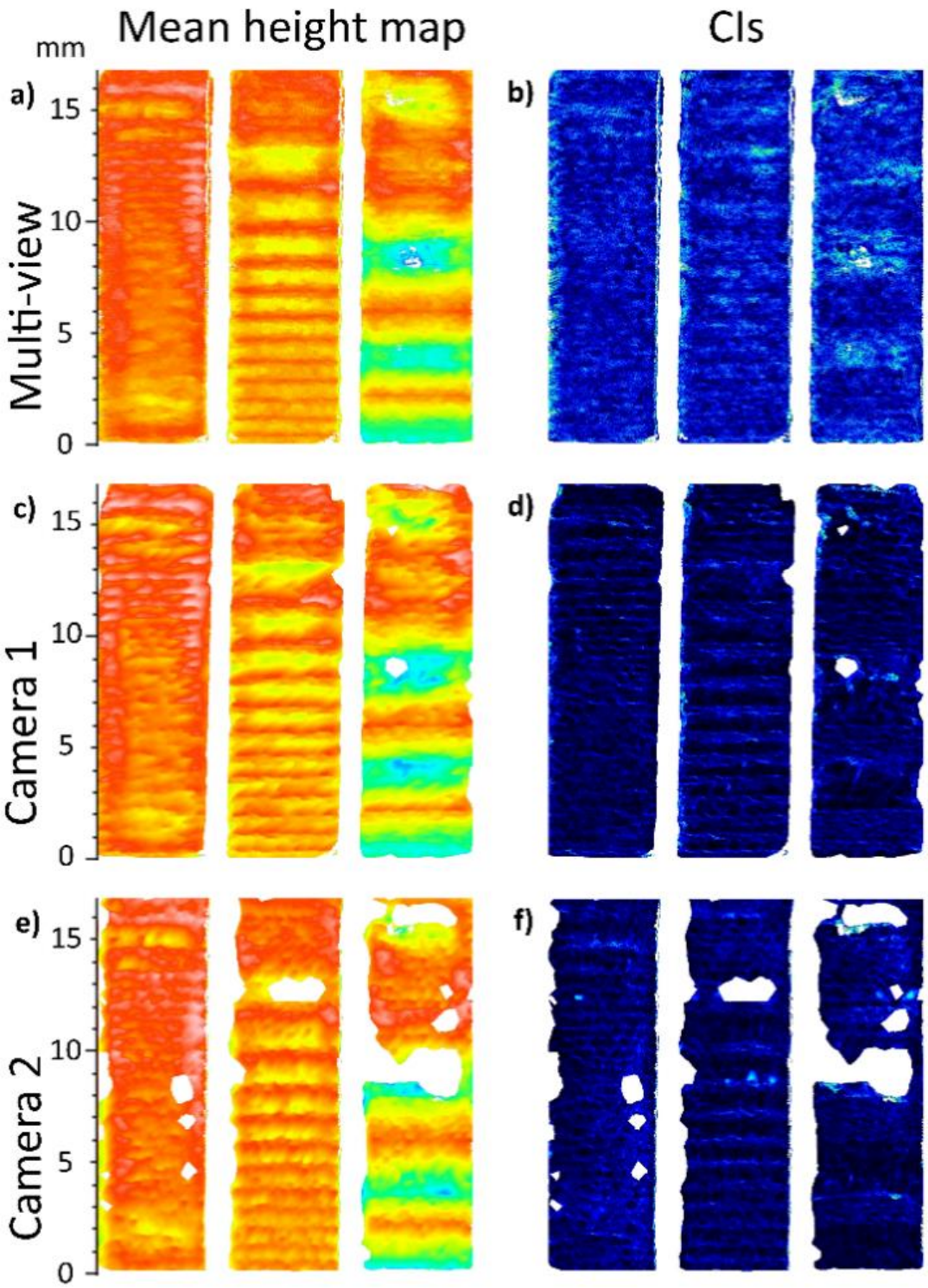
Mean height map
CIs
mm
a)
b)
c)
d)
e)
f)
Multi-view
Camera 1
Camera 2
15
10
5
0

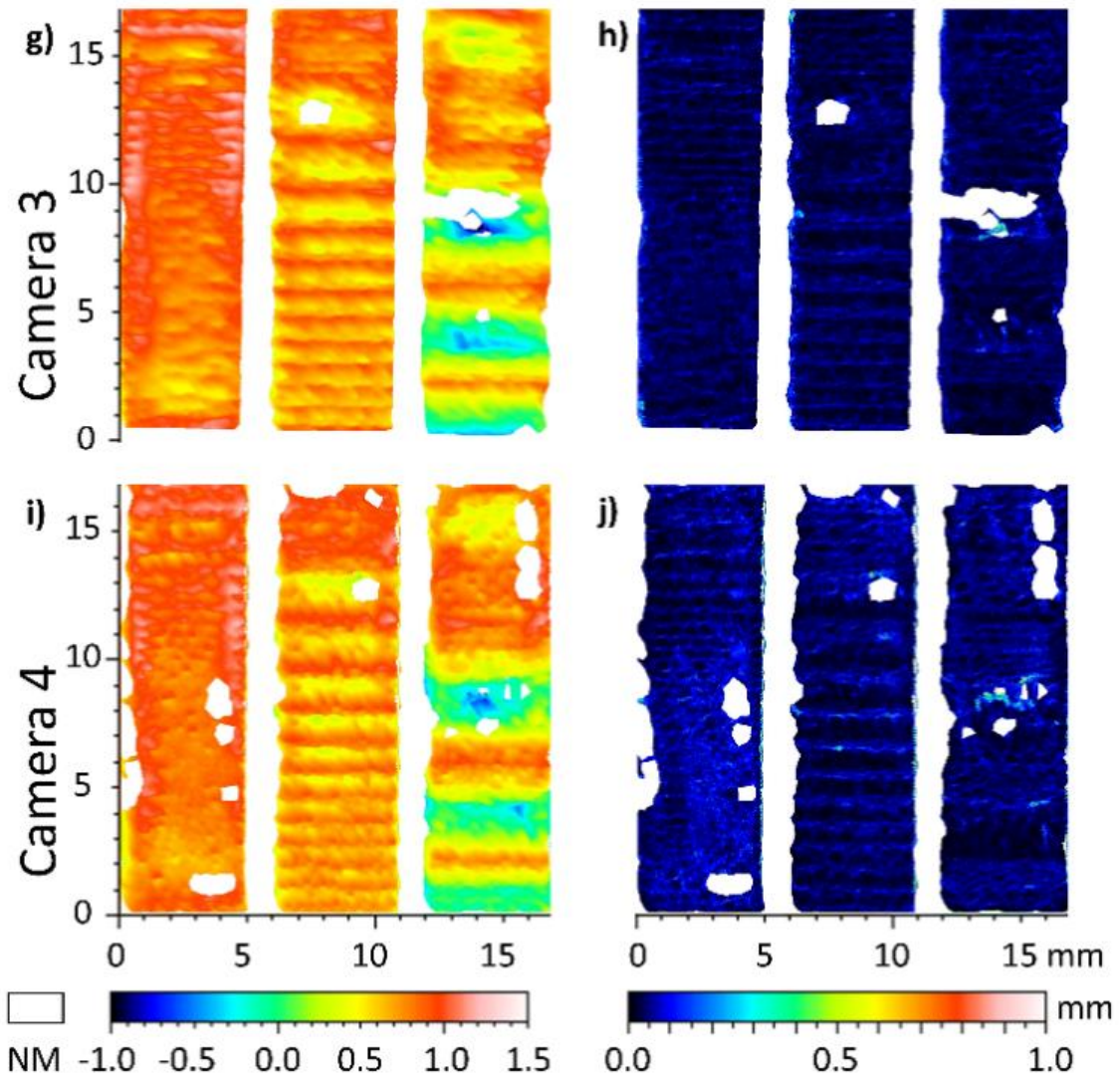

Figure 4.3.b. Mean height maps and CI maps for the multi-view (a and b) and single-view (c to j) FP measurements of the EB-PBF. Single-view FP measurements all show larger regions of data drop-out than the multi-view measurements, although CI widths are shown to have increased in the multi-view data (sub-figures a-f on previous page).

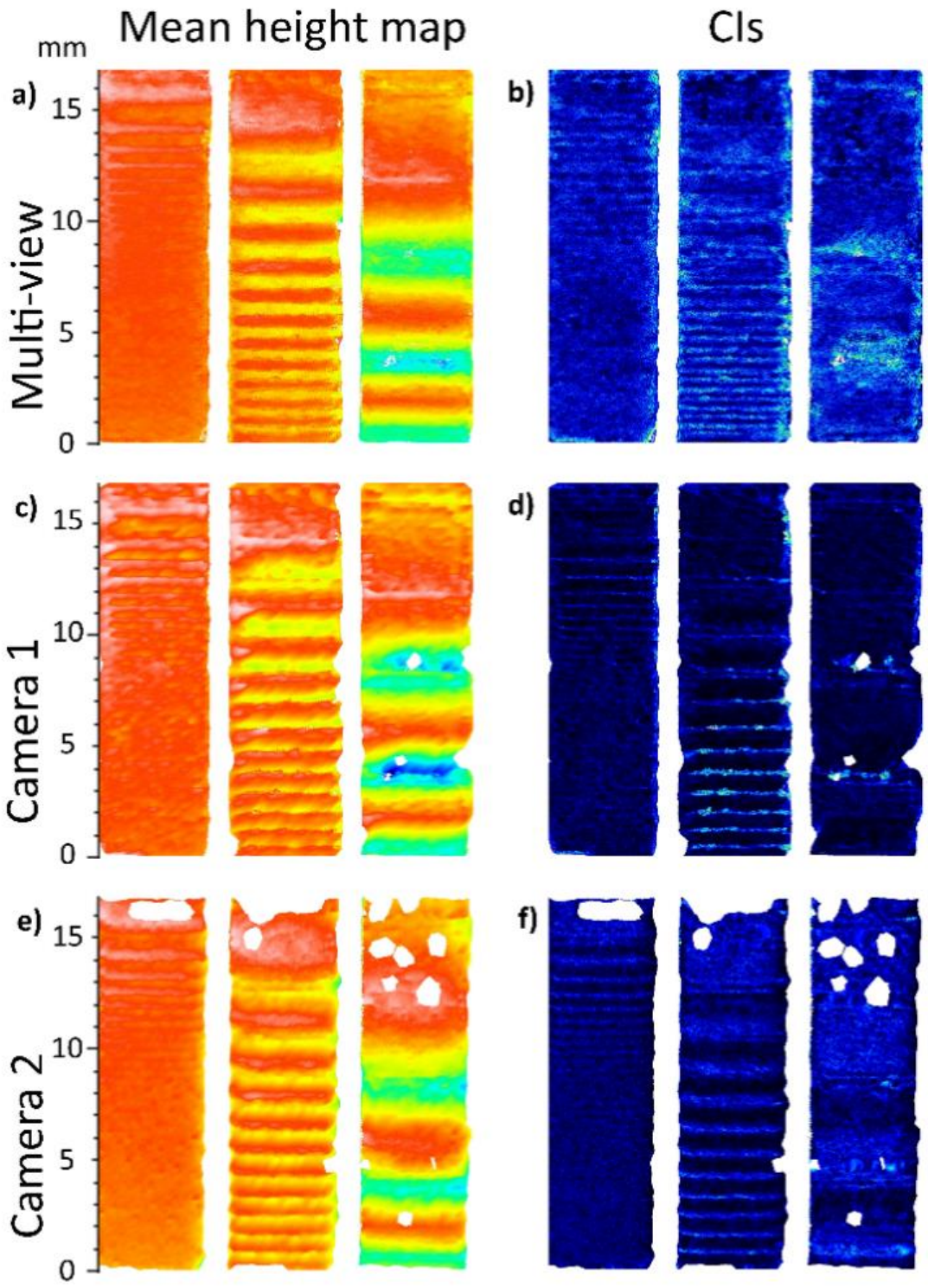
Mean height map
CIs
mm
a)
b)
Multi-view
15
10
5
0
c)
d)
Camera 1
e)
f)
Camera 2

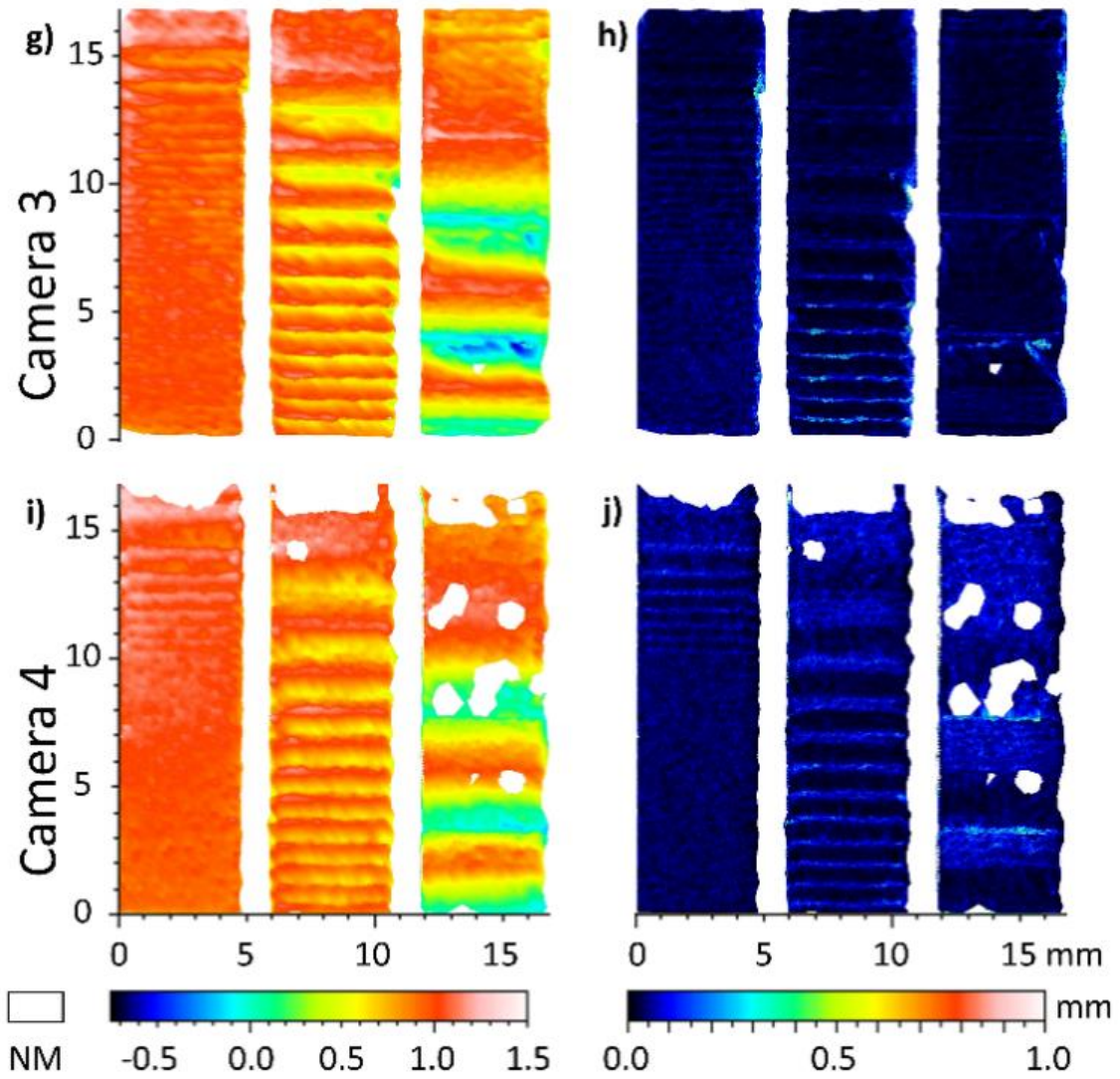

Figure 4.3.c. Mean height maps and CI maps for the multi-view (a and b) and single-view (c to j) FP measurements of the L-PBF. Single-view FP measurements all show larger regions of data drop-out than the multi-view measurements, although CI widths are shown to have increased in the multi-view data. The high spatial frequency structured sections of the L-PBF sample that can be seen in the FV data (Figure 4.3.a(c)) were not resolved by either of the FP methods (sub-figures a-f on previous page).

4.3.2.2 Measurement performance

CI widths for the FP measurements are presented alongside the height maps in Figure 4.3.b and Figure 4.3.c, while the mean and maximum CI widths from each measurement are plotted in Figure 4.3.d(a) and Figure 4.3.d(b) respectively. The multi-view method is shown to have significantly higher CI widths than each of the single-view height maps. As the same raw point cloud is used in both the single and multi-view scenarios, the

increase in multi-view CI width is not related to the repeatability of the individual camera measurements. Possible reasons for the increase in CI widths when using the multi-view system could be related to the use of data fusion with the multi-view dataset, with errors in the geometric characterisation of the global reference frame and the fine alignment performed in Polyworks|Inspector™ propagating into the final result. Another reason for increased CI widths when using the multi-view could be because the different camera views are effectively measuring different surfaces, since there is a large angular shift between their perspectives. Improvements to the data fusion method could potentially reduce the size of the CI for the multi-view data by reducing relative deformations in the individual point clouds. Although the additional transformations that occur from the data fusion process of the multi-view data may introduce further variation, effective averaging from multiple views results in a lower mean deviation than with the single-view height maps, with the mean deviation over both samples for the multi-view system being 68 µm and the mean over all individual views being 84 µm. Mean deviations across the surface for each data set are presented in Table 4 and Table 5.

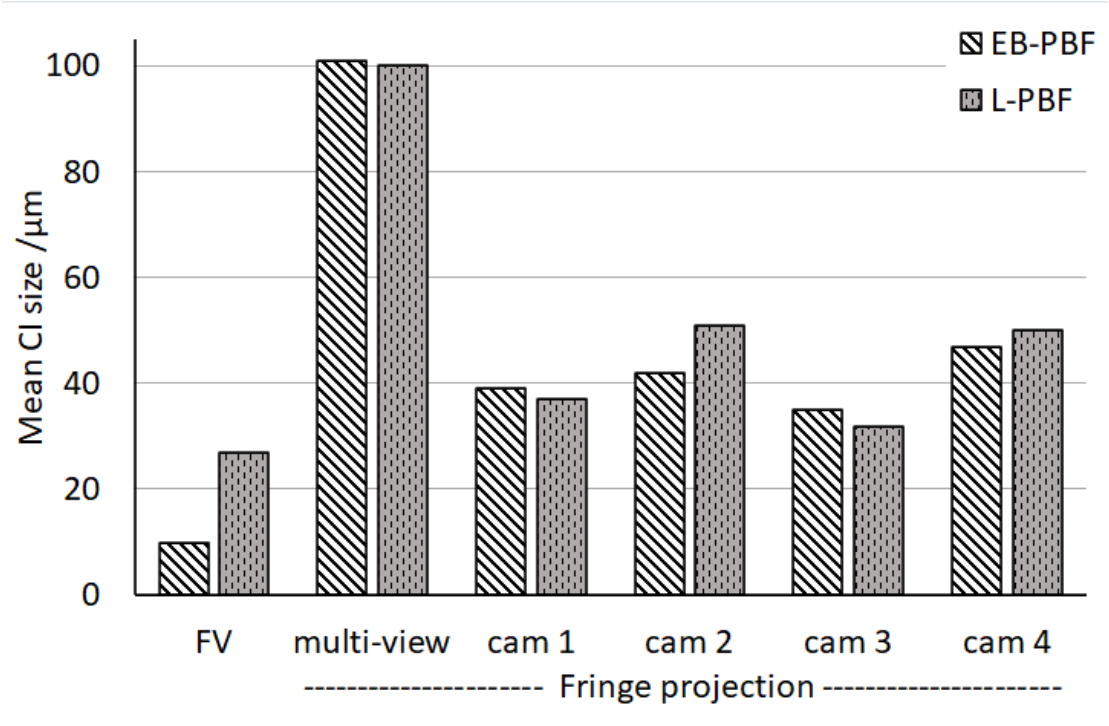

Figure 4.3.d. (a) Mean CI widths for all measurement methods on both the EB-PBF and L-PBF samples.

Deviation maps of the FP datasets against the FV reference are presented in Figure 4.3.e and Figure 4.3.f, along with the corresponding discrepancy maps. Discrepancy as a percentage of the FV surface is also provided in Table 4 and Table 5. The single-view FP height maps each have a much higher discrepancy percentage than the multi-view height maps, with the two multi-view datasets having a mean of 50.5% discrepancy between the two samples and the single-view counter parts having a mean of 78.9% across both samples and all views. The mean deviation across the whole surface is also 16 μm less on average when using the multi-view approach over the single-view measurements (values presented in Table 4 and Table 5), which can be seen over the deviation maps presented in Figure 4.3.e and Figure 4.3.f. The reduction in both discrepancies and mean deviations suggests that the multi-view approach has a higher level of accuracy than a single-view system for the same FoV. However, it is worth noting that the increase in CI widths will also have improved the discrepancy values as well the point-by-point deviations. The trade-off between achieving a lower mean deviation but a higher CI width results in a multi-view system having a higher level of accuracy, but a lower level of precision when compared to the single-view set-up.

A notable contributor to the deviations observed between the FP and FV data can be observed from the measurements of the deep, narrow valleys present on the L-PBF sample's higher spatial frequency section. The FV measurement of the L-PBF sample presented in Figure 4.3.a(c) shows the high spatial frequency form of section 3. In Figure 4.3.c, none of the FP measurements have been able to resolve the L-PBF samples surface features at the majority of section 3. While the FV system measures the sample orthogonally to the top surface, the cameras of the FP system are viewing the sample from a significant angular offset (seen in Figure (b)), which is a practical necessity for the FP method. This large angular offset results in the bottom of the sample valleys for the shorter peak-to-peak regions being occluded from the cameras line of sight, meaning that the bottoms of these valleys could not be measured by the FP system which results in the data showing what appears to be flat surface across the peaks of the features. Although for the sample used in this paper this appears as a significant limitation of the FP method, for the application of in-process monitoring it would not be expected that repeated features of such a high aspect ratio would occur, as by comparison the powder bed in a PBF is relatively flat.

4.3.2.3 Point cloud density

The multi-view FP point cloud (pre-meshing and raster scanning) has a mean point spacing of 73.4 µm, with the single camera approach having 136.7 µm (values for each data set presented in Table 6 and Table 2), resulting in a point density that is 3.5 times higher when using the multi-view approach over an area measurement. A higher point density for the measurement will result in an improved resolution capability in terms of observable features. However, even with the multi-view setup, the average point spacing of 74.3 µm achieved across the surface will likely need to be reduced further if smaller scale additive defects are to be detected. Assuming a minimum of 3 points must be taken over a feature for it to be clearly identified, This would make the current limit in resolving particle size to be somewhere in the region of 225 µm. This would make larger features such as larger pores [195], balling [195], and lattice deviations [26] (up to 500 µm) detectable, but not smaller pores or unfused powder [195] (sub 150 µm).

Table 6. Mean point spacing of the FP point clouds for EB-PBF sample (rounded to the nearest micrometre).

EB-PBF Data set	Multi-view FP/µm	Single-view FP/µm			
		Cam 1	Cam 2	Cam 3	Cam 4
Repeat 1	76	138	131	158	133
Repeat 2	76	137	131	158	132
Repeat 3	75	137	131	159	131
Repeat 4	76	137	132	158	132
Repeat 5	76	137	131	158	131

Table 7. Mean point spacing of the FP point clouds for L-PBF sample (rounded to the nearest micrometre).

L-PBF Data set	Multi-view FP/µm	Single-view FP/µm			
		Cam 1	Cam 2	Cam 3	Cam 4
Repeat 1	73	147	121	140	129
Repeat 2	72	147	121	141	129
Repeat 3	73	148	123	141	129
Repeat 4	73	147	123	141	129
Repeat 5	73	147	121	142	129

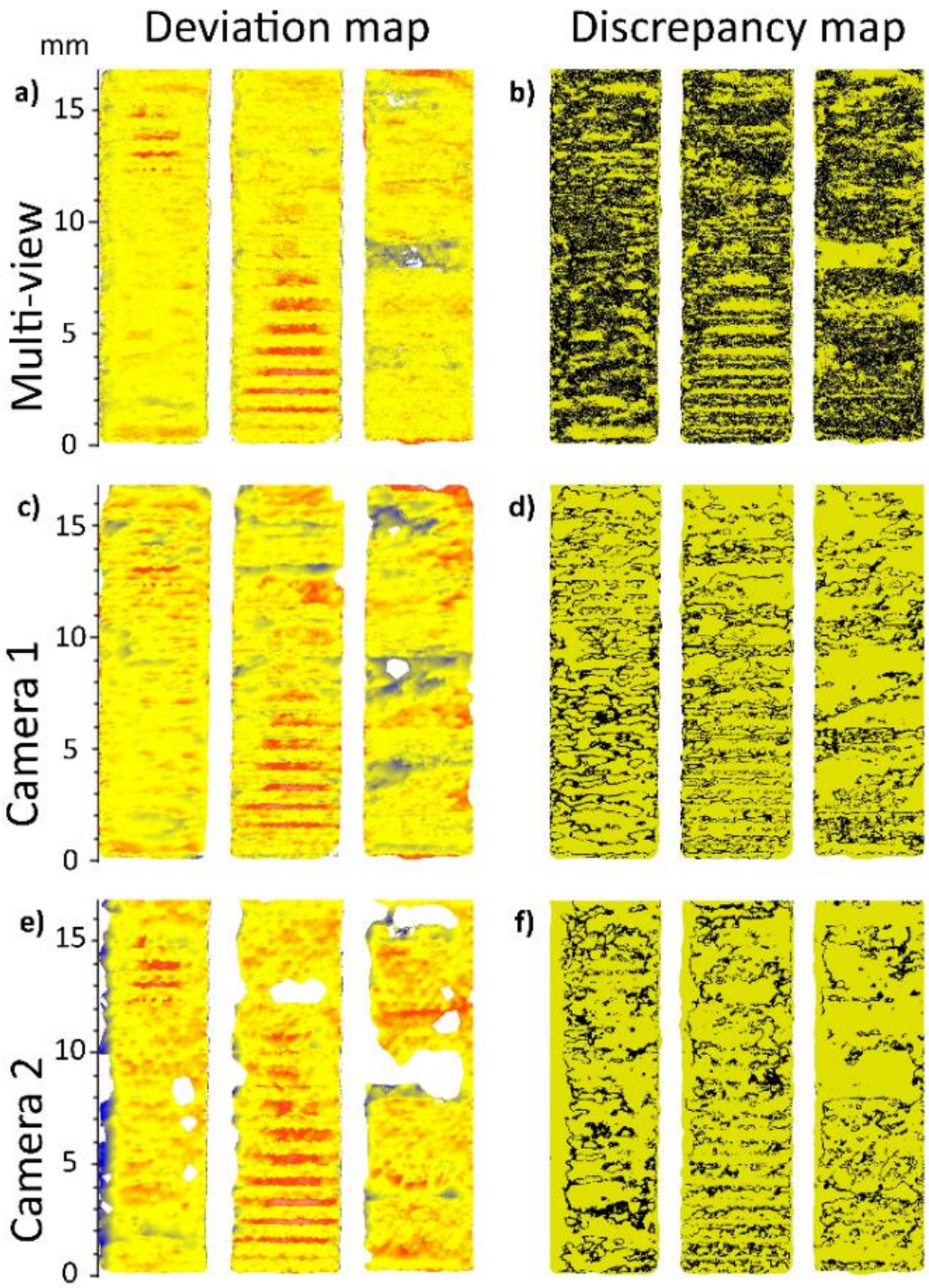
Deviation map
Discrepancy map
mm
a)
b)
Multi-view
15
10
5
0
c)
d)
Camera 1
e)
f)
Camera 2

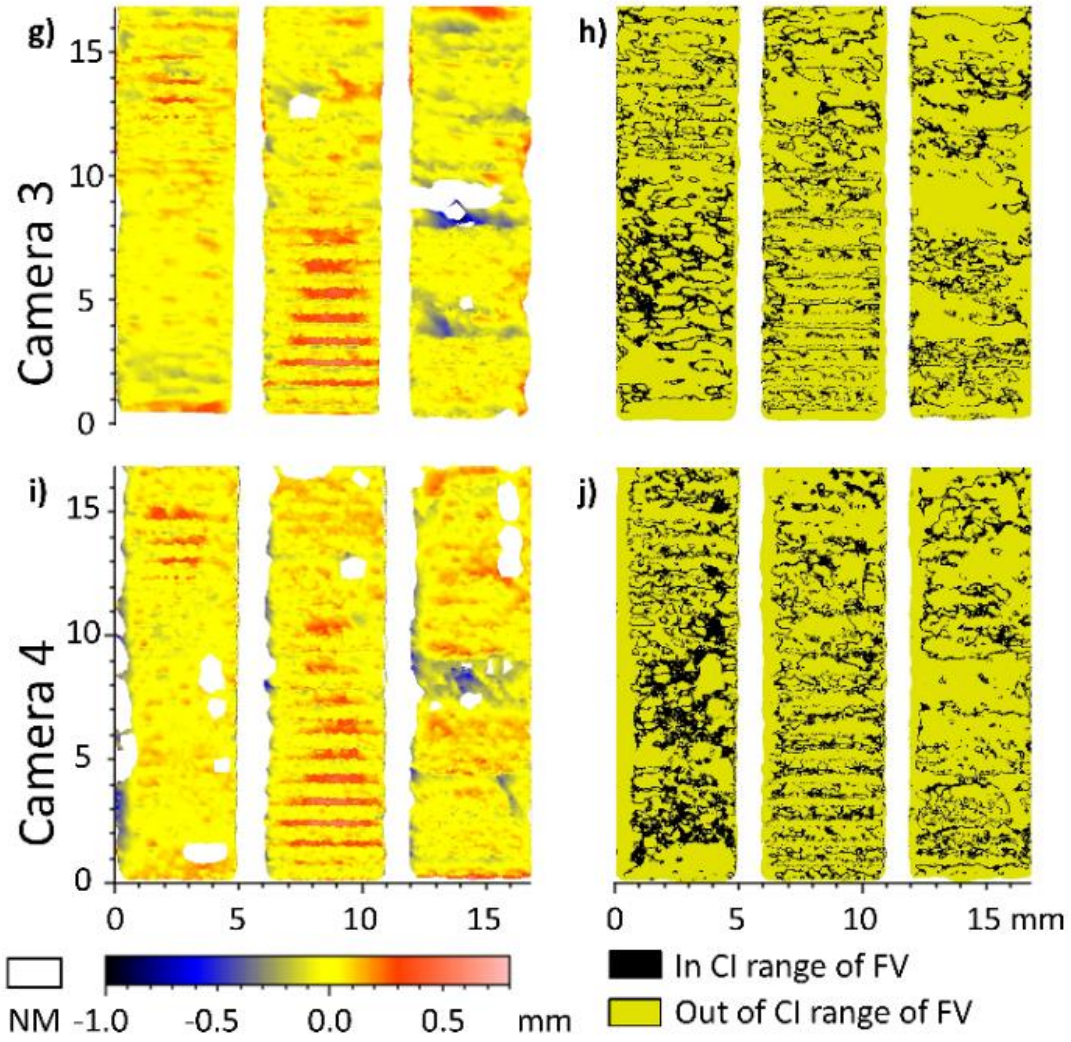

Figure 4.3.e. EB-PBF FP against FV difference map and discrepancy (within CIs). Regions of data drop out from the FP system have been plotted as discrepancies. The multi-view measurement shows a vast improvement in both the deviations and discrepancy across the surface. Each of the single-view FP measurements has significant regions of the surface exceeding 0.5 mm of deviation from the FV measurement that are not present on the multi-view data (sub-figures a-f on previous page).

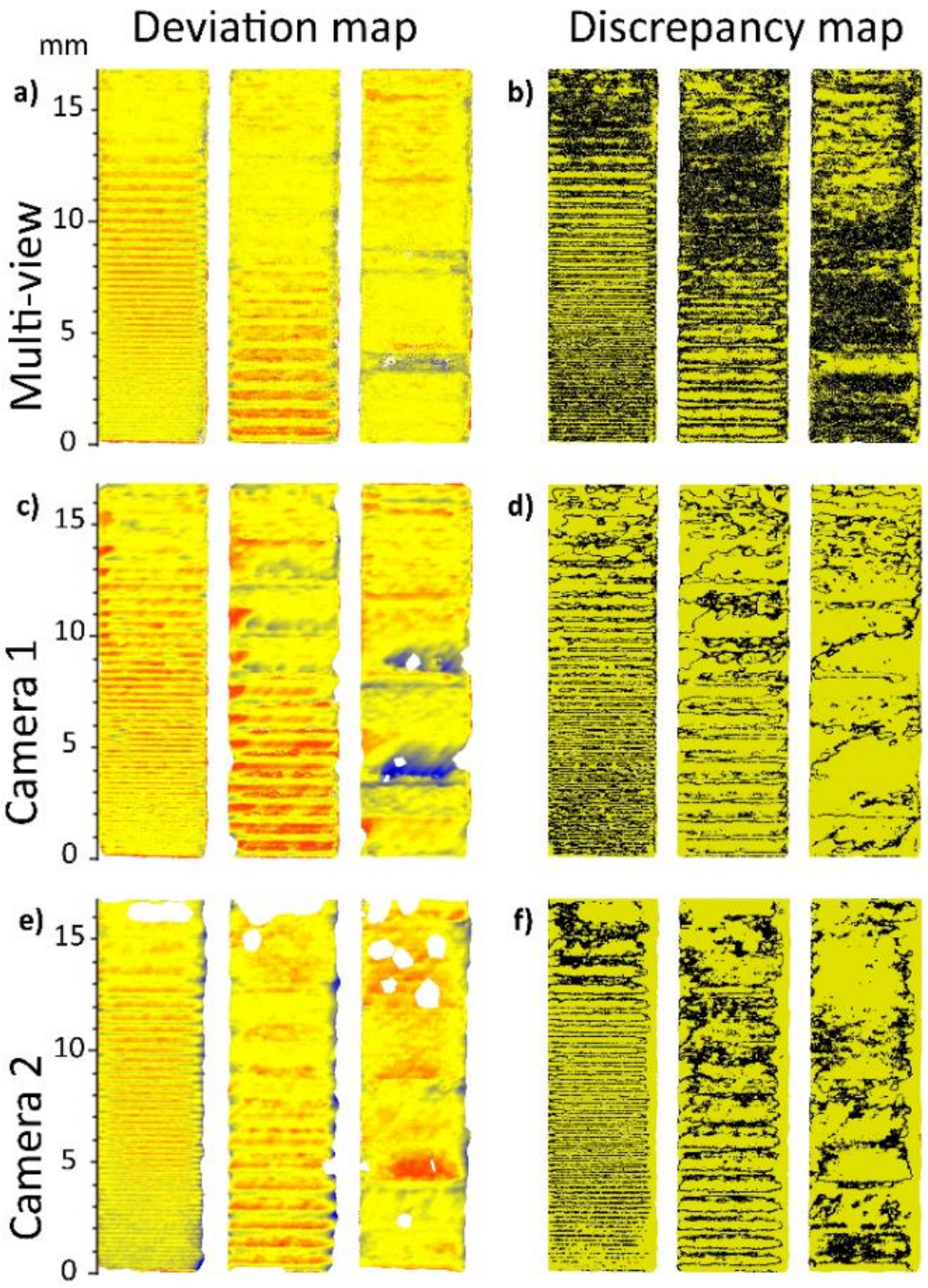
Deviation map
Discrepancy map
mm
a)
b)
Multi-view
15
10
5
0
c)
d)
Camera 1
e)
f)
Camera 2

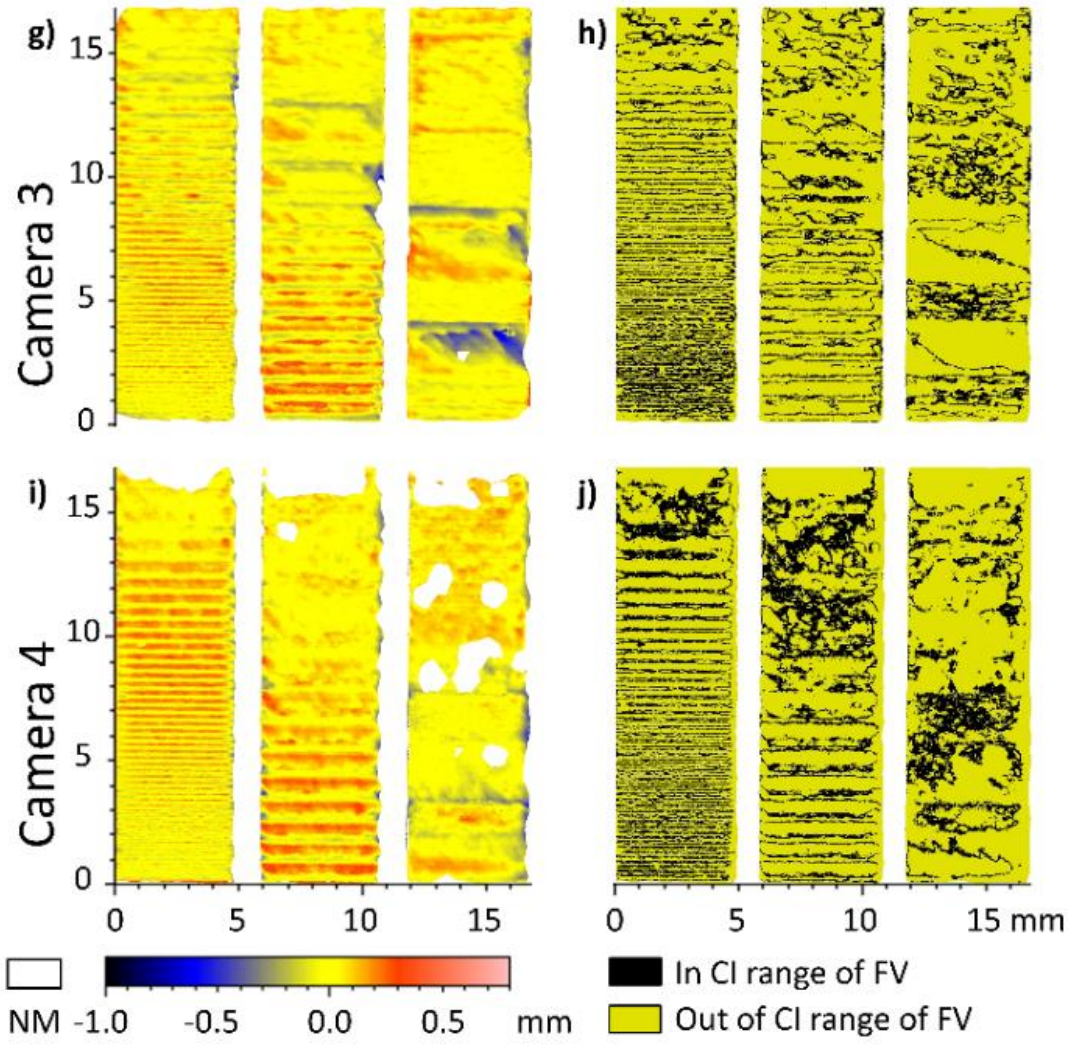

Figure 4.3.f. L-PBF FP against FV difference map and discrepancy (within CIs). Regions of data drop out from the FP system have been plotted as discrepancies. The multi-view measurement shows a vast improvement in both the deviations and discrepancy across the surface. Each of the single-view FP measurements has significant regions of the surface exceeding 0.5 mm of deviation from the FV measurement that are not present on the multi-view data (sub-figures a-f on previous page).

4.3.2.4 Profiles

Profiles of section 2 for the L-PBF sample are presented in Figure 4.3.g. In the plots, angular perspectives of the different cameras on the single camera FP data influence the peak topographies measured. On all single-view measurements, the profile skews in the direction of the camera's placement in the chamber (shown in Figure (b)), with cameras 1 and 4 skewing to the left, and camera 2 and 3 to the right. This deformation is averaged

out in the multi-view data, creating a profile that is more representative of the FV profiles but with a higher level of noise introduced from the fusion process. This skewing effect on single-view FP measurements is a further example of how the single-view has a lower level of accuracy than the multi-view approach. The inaccuracies of the single-view measurements over the surface features presents another possible cause for the increase in CI width observed on the multi-view dataset, as the fusion of the multi-view data is effectively averaging out the imperfections of the single-view measurements. This same effect was observed on profiles for all three sections on both samples. The skewing effects of the profiles would be expected to be greatly reduced when performing in-process measurements due to the relative flatness of the powder bed in comparison to the features present on the samples used in this study.

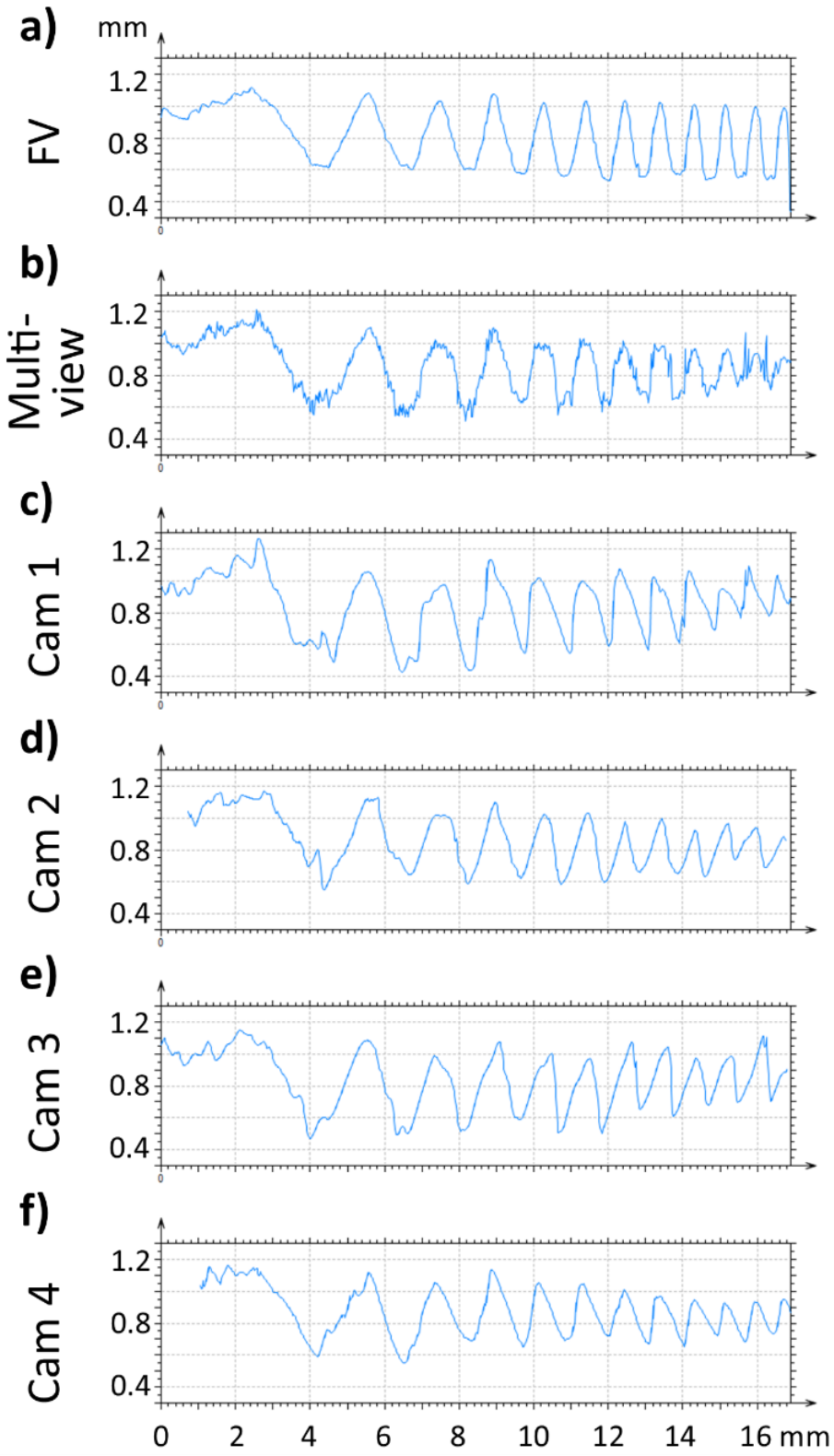

Figure 4.3.g. Line profiles from the aligned datasets of the L-PBF sample. Each numbered section corresponds to the sections labelled in Figure 4.2.b(a) and the profile is taken down the approximately the centre of each section.

4.4 Conclusions from repeatability tests

In this chapter, measurements of two AMSA4 [29] samples, one manufactured through L-PBF and the other EB-PBF, have been performed using a multi-view FP method, single-view FP and FV to assess the improvements in performance of the multi-view system when compared to single-view data.

- Measurements made using the multi-view approach provided a reduction in regions of missing data as well as an overall higher point cloud density than the data acquired using a single-view method. In comparison with FV measurements of the same surfaces, the multi-view measurements were shown to be more accurate than a single-view FP measurement, with an average decrease in point-by-point deviations of 16 μm.
- The multi-view measurements consistently achieved a higher level of surface coverage, measuring 98.7% and 99.5% of the EB-PBF and the L-PBF surfaces respectively.
- The point cloud density of the multi-view system data was found to be 3.5 times higher than the single-view approach which means there is a higher lateral sampling rate over the measurement area.

Although the multi-view system is of higher accuracy, surface coverage and point density, the data acquired also proved to have a higher average CI width across the measured surface, suggesting a lower level of precision. There are several potential reasons for this increase in CI width, including additional errors introduced by the geometrical characterisation and data fusion of the multi-view approach. The individual camera measurements also proved to have a skewing of the high aspect ratio surface features which contributed to the single-view methods decrease in accuracy that was averaged out in the multi-view data for a trade-off of increased noise in these regions.

4.4.1 Remaining issues from repeatability testing

In the configuration that was used for the measurements presented in this chapter, the measurement capabilities may not be sufficient for the detection of smaller surface defects that may be present in the metal PBF build process (sub-100 μm in lateral size). In chapter 5 modifications have been made to the system to increase point cloud density by

repositioning the cameras for a slightly smaller FoV so that layer-wise defects in the PBF process would be more likely to be detected. With the set up used in this work, each perspective's horizontal FoV was approximately 350 mm. Typical commercial metal PBF systems have a build area between 100 mm and 250 mm in width, meaning that a reduction in camera FoV would still cover the majority, if not all, of the powder bed.

Due to the use of a commercial cinematic projector (which is operated as a second monitor for the systems computer with full screen fringe images being displayed for the projections) the acquisition cycle is software synchronised with induvial captures being trigger independently with each new projection. This is a limiting factor stopping the system from measuring at a faster rate due to the commercial projector that cannot be hardware synchronised with the cameras. In theory, when using an industrial projector the acquisition rate would be limited by the camera's maximum frame rate of 17 fps, which would result in the nineteen images being captured just over 1 s. The acquisition time could then be reduced further by using higher framerate cameras if necessary. In the configuration used in this chapter, each measurement takes roughly 5 s, which over the course of an entire part build could add too much to the manufacturing time if every layer is measured. To improve the performance of the system presented, Further testing will also be performed with the cameras configured to cover a smaller measurement area to further increase the point cloud density, making the system better suited for the detection of smaller-scale PBF defects.

For use in a manufacturing environment, it is not enough to simply be able to acquire the topography of a given layer in the build process. For the data be gather to be useful there must also be an automated analysis of the measurement so that potential issues can be flagged without manual data processing and analysis. Future testing of the system's capabilities will include feature based segmentation [217–220] of the multi-view FP measurements to assess how well metal PBF surface features can be identified using this approach as a potential method of automical defect detection.

5 Feature based characterisation

The work presented in chapter 4 has shown that surface topography data captured from reference samples by this technique does closely match the information that could be captured on a conventional lab-based surface topography measurement instrument, despite limitations in resolution. Whilst the ability to capture similar surface topography is beneficial, in an in-process monitoring scenario, two further aspects need to be considered: firstly, meaningful information must be inferred from the measured topography (content relevant to understanding how the manufacturing process is behaving must be extracted). Secondly, meaningful information must be extracted and processed quickly enough to allow for corrective actions to be taken or alerts triggered, in case of anomalies. In this chapter, the challenge of extracting meaningful information from topography measured by multi-view FP is addressed.

5.1 In-situ feature identification in additive manufacturing

For in-situ monitoring systems to be of significant value in a manufacturing environment it is not enough for a measurement to simply be taken. Information relevant to the process and part quality must be extractable from ted at collected in a repeatable manor so that any potential issues with the process can be identified and acted on. The importance of this ability is being highlighted more frequently in the literature surrounding in-situ monitoring of additive processes as more researchers focus on the identification of defects and final part quality indicators through a variety of different data processing methodologies.

Different machine learning approaches have been applied to single weld track monitoring systems to automatically identify spatter and plume behaviour from in-situ video footage of the melt-process using deep belief network classifiers [186] and CNNs [187,188] with high rates of success in correctly identifying targeted features. A semi-supervised classification approach has also been applied to meltpool images captured by a co-axial high-speed camera [164] on single weld tracks with similar promising results.

In-situ systems have been used to predict microstructural properties, such as grain size and orientation, which can provide valuable insights into final part quality and process variations throughout the build [106]. This has been studied in EB-PBF processes through

in-situ thermography [105] to access how different scan strategies may impact grain orientation with agreement between in-situ predictions and post-process destructive inspections. In L-PBF, in-situ thermography has been used to relate layer surface temperature to grain growth and orientation, as well as the amount of spatter being ejected from the meltpool [89].

In-situ porosity detection has been one of the largest areas of interest in the literature, with three main focusses on the topic:

- Voids included into the model of the part, which are also referred to as "artificial" or "intentional" pores
- Local porosity (single pores or local clusters of pores, either spherical or irregular pores caused by lack of fusion)
- Part density (the overall percentage of voids in the volume)

Voids of different shapes and sizes were used in various studies, including cubic voids with sizes in the range 30 μm to 300 μm [137] or 50 μm to 750 μm [47,79,80], cylindrical voids with diameters in the range 50 μm to 750 μm [47,79,80] and spherical voids with diameters in the range 600 μm to 900 μm [84]. In L-PBF, binarization of optical layer-wise imaging has been used to feed supervised machine learning algorithms for the detection of pores on powder bed surface [52,79,80]. Off-axis dual wavelength video data has also been used to estimate meltpool properties and compare these against a thermal map of the layer to identify voids by using a neighbourhood searching algorithm to sort meltpool images as either normal or outliers [137]. Comparisons to post-process XCT measurements have been made to determine the success rate and further train the algorithms.

Local porosity detection on L-PBF methods has been carried out using 3D constructions of layer-wise imaging [46], mapping of hot and cold areas and through in-situ thermography [53], IR video image data [67,95,189] with comparisons to post-process XCT measurements of the parts as a ground truth for part porosity. Sub-surface pores have also been correlated to cooling profiles re-constructed by in-situ thermography using in-situ X-ray video image as the ground truth [101]. In EB-PBF, NIR layer-wise imaging

[55] in-situ electron beam imaging [74] have been used to detect pores by pixel intensity values with comparisons to post-process XCT measurements being made.

In-situ measures of globally porosity over the build of the part have been carried out by multiple researchers. Features identified from layer-wise optical images of both the powder layer post coating [39,178] and the build layer post melting phase [38] have been shown to correlate with final part density. Off-axis multi-spectral spatially integrated pyrometry measurements in L-PBF [179] have also been found to correlate with global porosity through Fourier analysis of measured signals. Machine learning algorithms have been applied to co-axial mounted photodiode signals [149], meltpool images [162], spatter descriptors [121], and acoustic emissions [133,134,177] all with the aim of monitoring global part porosity in-situ.

Geometrical distortions across the powder bed have been monitoring and identified through a few different methods. Binarised powder bed images have been fed into a CNN to monitor thing wall features in L-PBF [82] with a similar approach being expanded to full part monitoring by comparing the images layer with a corresponding CAD slices of the part being built [48]. Layer-wise imaging of L-PBF has also been used to feed a MsCNN to monitor for features such as recoater hopping and streaking, incomplete powder spreading, presence of debris on the powder bed, super-elevated edges and other part damages pre-melting phase [50,51]. Hotspot detection using high speed video images from off-axis machine vision cameras [190] has been performed using principle component analysis to allow for automated identification of local hotspot events [191]. Monitoring stability of plume emissions over time during L-PBF using off axis IR video has also been done with correlations between plume events and part defects being found [34,108].

Other defects, such as residuals stresses, cracks, and delamination have also been identified during the build process via in-situ monitoring methods. Residuals stresses have been observed using X-ray diffraction to detect stress formations and phase changes beneath the current layer in custom built L-PBF systems [132,168]. Delamination detection has been developed through the use of a “smart” build-plate with embedded fibre optic strain sensors [170] capable of measuring strains, directions of strain vectors and location delamination events, as well as some cracking that may occur near the

baseplate surface that may not be visible with other sensors. Off-axis IR video imaging has also been used in combination with deep learning algorithms to detect severe defects that may cause large heat accumulations in the layer, such as delamination [241].

All these methods follow the same aim of attempting to correlate measured signals with known, real defects that have developed during the parts manufacture. This work is essential for the future of automated systems that can flag manufacturing issues without user intervention or interpretation of the measured data.

5.2 Feature based characterisation

FBC is a developing area of surface metrology that focusses around the characterisations of features found in topographical data that has been proven effective at identifying expected features on PBF surfaces [242,243]. This approach varies from conventional methods of surface characterisation, such as surface texture parameters like roughness and waviness, by targeting individual features on the surface. This is typically performed by segmenting topography into localised regions, and is done through a variety of different algorithms. The complete sequence of data processing operations characterising a FBC approach is usually custom-tailored to application-specific needs, and can be automated once these needs are verified and tested. However, due to its complexity and computational requirements, feature-based topography characterisation has not seen widespread application to in-situ measurement yet. Conventional optical imaging has more commonly been applied for automated detection, as discussed in section 5.1, and has shown promising results due to the intrinsic speed of image taking and the mature tools available for image processing methods. There has been some work on processing measured surface topography data in ways that are like FBC, for example by computing maps of local curvatures [194], and other attempts at processing topography data specifically acquired in-situ [59,61,65,193] though no comprehensive endeavour towards defining a proper FBC pipeline has been attempted yet.

The design of a proper, FBC-compliant data processing pipeline must start from the identification of localised topographic formations which must be targeted, i.e. the topography “features” of interest for the specific application. Leftover particles (isolated and in clusters) and spatter features are localised topographic formations, of similar

protruding nature, which are dominant on PBF surfaces due to the nature of the PBF process. Particles results from lack of, or incomplete, fusion of the powder bed. Spatter features are formed by fully molten gobs of material ejected from the processing area and fallen back onto the surface. FBC methods to identify leftover particles and spatter features have been successfully implemented in previous work, however only from lab-based surface topography measurement, i.e. not in-situ [243–245].

The in-process identification of leftover particles and spatter features from in-situ topography measurement has important implications for PBF process monitoring, because being able to detect such features paves the way to detecting important anomalies related to the manufacturing process. As the PBF process builds a part, a layer of powder is spread using a wiper blade or powder roller to ensure the creation of a powder bed characterised by an even distribution of material (even thickness) for optimal, subsequent laser processing [11]. However, if a spatter formation of particle cluster is excessively large, it may stick out of the powder layer and consequently influence the laser melting process, or even interfere with the wiper blade or roller during spreading, resulting in catastrophic collisions, or at least causing unevenness of the bed and consequent defects in the part [117,246].

5.3 Methodology for feature based characterisation

An investigation of the performance of the measuring system based on multi-view FP is performed by acquiring the surface topography of samples fabricated by metal L-PBF. Most of the relevant surface topography features (leftover particles and spatter) are present in the samples. The analysis is aimed at determining if the achievable measurement resolution and in general, the metrological performance, which is compatible with the needs of an inspection process targeting features of such sizes and shapes.

5.3.1 Measurement technologies

5.3.1.1 Final multi-view fringe projection system

The multi-view FP system used in this chapter is an updated version of the system described in detail in section 4.2.1.1. The system is comprised of four Basler ace acA5472–17um cameras and a newly fitted DLP Lightcrafter 6500 projector to replace

the Optoma projector previously used. The new projector provides monochromatic image projection rather than RGB to match the Basler cameras and allows for hardware synchronisation that was not possible with the Optoma projector. The Basler cameras have been repositioned to give a slightly smaller FoV than the previous version of the system with the aim of achieving point clouds of higher density (example of one of the perspectives white images shown in Figure 5.3.a). The projection and measurement cover the entire width and most of the length (approximately 190 mm) of the (265 × 265) mm measurement stage with the FoV of all four cameras covering the entire projected image.

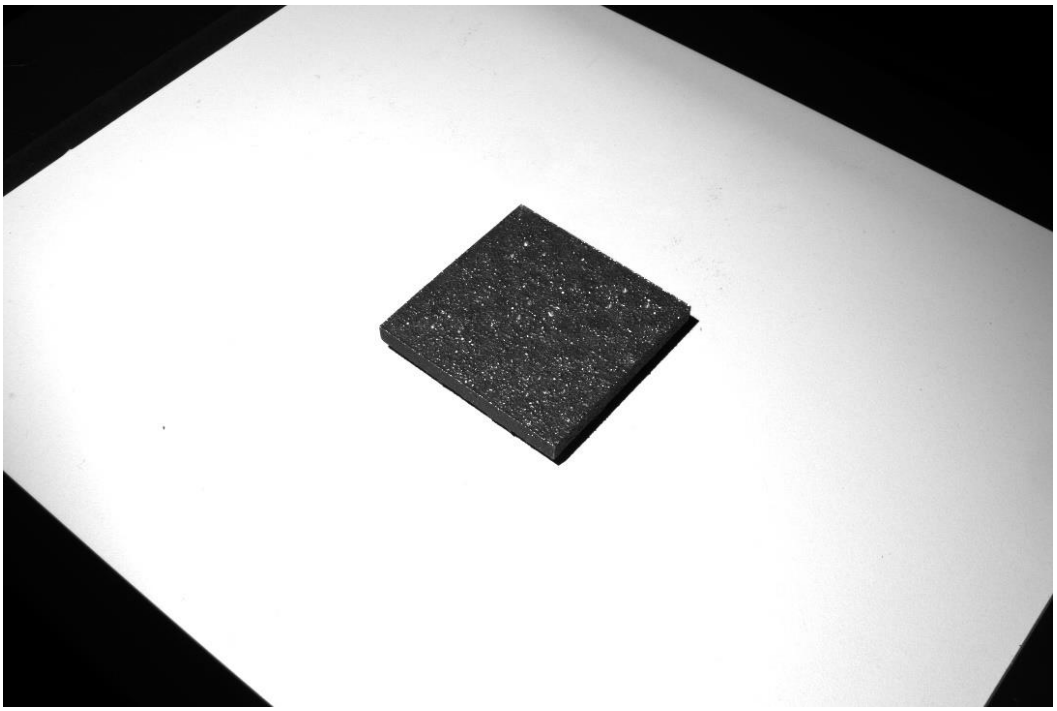

Figure 5.3.a White image of L-PBF flat sample within the measurement volume of the FP system.

5.3.1.2 Focus variation microscopy

As with in chapters 3 and 4, FV microscopy was used as the reference lab-based measurement. FV can operate at higher sampling resolution with respect to our multi-view FP and has been demonstrated to be a suitable reference for the measurement of PBF surfaces [247]. The following settings were used to measure the entire top surface: 5× magnification objective lens [numerical aperture: 0.15, FoV: (2.82 × 2.82) mm, pixel sampling resolution: 3.52 µm], ring light illumination; instrument vertical resolution: 1 µm and instrument lateral resolution: 7.25 µm. Stitching of multiple FoVs were

performed to measure a (59.2 × 59.2) mm measurement area. Each FV measurement resulted in a height map (a matrix of height (z) values arranged onto a regular *x,y* grid with uniform *x,y* spacing).

5.3.2 Samples

A (50 × 50 × 5) mm L-PBF flat sample was used in this work, as shown in Figure 5.3.b. The sample was chosen for the presence of leftover particles/spatter on the top surface, as well as for the overall size of the measurable surface. While the whole surface was measured for the sample, a region of (10 × 10) mm was cropped down for the analysis and comparison as the FV system the data is being compared against is not capable of measuring the entire sample surface. These region the data has been cropped to is representative of the wider surface in terms of surface features.

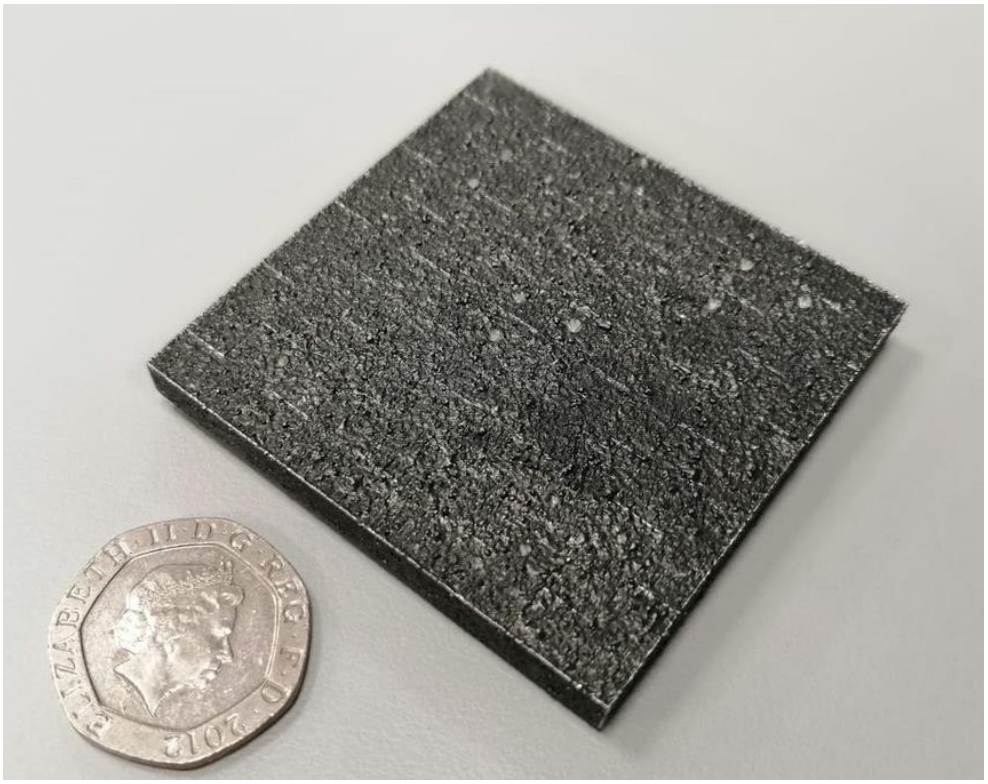

Figure 5.3.b Photograph of the (50 × 50 × 5) mm L-PBF flat surface with a British 20 pence piece for scale.

5.3.3 Alignment and registration

Following the same procedure described in sections 3.3.3.1 and 4.2.3.1, each FV dataset (height map) was cropped to only include an (10 × 10) mm region using Polyworks Inspector [248]. The FV cropped maps were then downsampled to 20 µm point spacing through linear interpolation and converted into triangle meshes using Delaunay triangulation. The multi-view FP point cloud for the same surface (or analogously, any point cloud obtained using only one camera-projector pair in the FP system) was registered to the FV reference dataset over 6 degrees of freedom using coarse alignment by point selection followed by a finer ICP alignment [230–232]. The aligned FP point cloud was also triangulated using the Delaunay method. The whole process resulted in two triangle meshes (one FV and one FP) coarsely aligned to each other and to the *x,y* plane. In order to investigate geometric differences between the two meshes, both were resampled into aligned height maps using a virtual raster scanning method implemented in MATLAB. Virtual raster scanning consists of probing local heights on triangle meshes at selected locations defined by a regular *x,y* grid. Scanning was performed at 20 µm spacing to replicate the density chosen for the initial down-sampling. Following scanning, heigh values resulted vertically aligned at the same *x,y* positions, allowing for local comparison of heights. Both maps were finally cropped to the RoI. Moreover, the FP maps were smoothed by low-pass Gaussian filtering (nesting index: 20 µm) to reduce noise.

5.3.4 Feature-based characterisation

Using the method developed in Newton et al. [245], the active contours algorithm was applied to perform segmentation and isolation of leftover particles/spatter features on the PBF surfaces. Segmentation was performed using the following steps, optimised for the FV dataset:

- Application of a L-filter (low-pass) with nesting index of 800 µm, designed to better highlight localised protrusions of the targeted size on the surface, whilst reducing any other higher-frequency topographic formation.
- Generation of an initial guess mask (needed by the active contours algorithm), by applying thresholding on heights, using a height threshold equal to 95% of the height range.

- Application of the active contours algorithm, starting from the initial guess mask, to "grow" the initial masked regions outwards, to increasingly approximate the actual particle/spatter boundaries, over 100 iterations.

5.3.5 Comparisons of FP and FV feature-based characterisation results

The same feature-based characterisation method was applied to the FV and FP height maps. A quantitative comparison of the results was then performed using the method presented in Newton et al [230], using the FV results as the reference. The comparison method consisted of pairwise comparison performed at all the locations of the two segmented maps, using a binary classification scheme where each location labelled as belonging to a particle or spatter formation is tagged as "true", whilst the other locations are labelled as "false". Using the FV segmentation result as the reference, then each the FP segmentation result at each corresponding location was therefore labelled as true positive, false positive, true negative or false negative depending on the local agreement of segmentation results. After this initial classification, the following metrics were computed:

- Precision – positive predictive value – measure of the proportion of true positives over all positive instances. High precision implies a small number of excess feature points.
- Recall – True positive rate – measure of the proportion of positives that are correctly identified. High recall implies a small number of missing feature points.
- Specificity – True negative rate - measures the proportion of negatives that are correctly identified. High specificity implies a small number of excess feature points (pixels wrongly recognised as belonging to the feature). However, different to precision, the viewpoint is the identification of the background.
- Balanced accuracy – arithmetic average of recall and specificity, this metric is less skewed by differences in number of feature and background pixels in the analysed region when compared to the conventional accuracy metric.

Additionally, visual comparison was performed on single features (particles or spatter formations) in the topographies, as well as over the whole topography, looking at the

topographies themselves, the resulting segmentation mask applied to the surface topography and the binary classification comparison over the surface topography.

5.4 Results

5.4.1 Surface topography measurement

The large (10 × 10) mm cropped region that is representative of the whole surface on the L-PBF flat sample surface as measured by FV can be shown in Figure 5.4.b. As with in chapter 4, discrepancy, surface overlap, mean deviation and mean point spacing were calculated for the repeat 5 measurements of the L-PBF flat sample and are present in Table 8 and Table 9. Deviation maps over the (10 × 10) mm cropped region can be seen in Appendix A1.

Table 8. Discrepancy (percentage point-by-point disagreement), surface overlap (percentage of data surface coverage) and mean deviation (point-by-point difference is height value) between FP and FV height maps of the L-PBF flat sample.

Ti-flat sample	Multi-view FP	Single-view FP			
		Cam1	Cam2	Cam3	Cam4
Discrepancy from FV /%	12.58	28.97	30.61	28.76	27.08
Surface overlap from FV /%	100	99.95	100.00	99.98	100
Mean deviation from FV /μm	27.2	34.7	30.0	34.6	28.5

Table 9. Mean point spacing of the FP point clouds for the L-PBF flat sample from the first measurement of 5 repeats (rounded to the nearest micrometre).

Ti-flat sample	Multi-view FP/μm	Single-view FP/μm			
		Cam 1	Cam 2	Cam 3	Cam 4
Repeat 1	35	72	66	75	65

When compared to data from the previous version of the system, discrepancy, mean deviation and mean point spacing appear to have improved. Although individual camera CIs appear to be larger than before (presented in Figure 5.4.a). This increase in CI values could possibly be a result of the difference in sample surface form being measured or a result of the change projector, which is now projecting a (1920 × 1080) pixel image rather than a (3840 × 2160) pixel image from the Optoma.

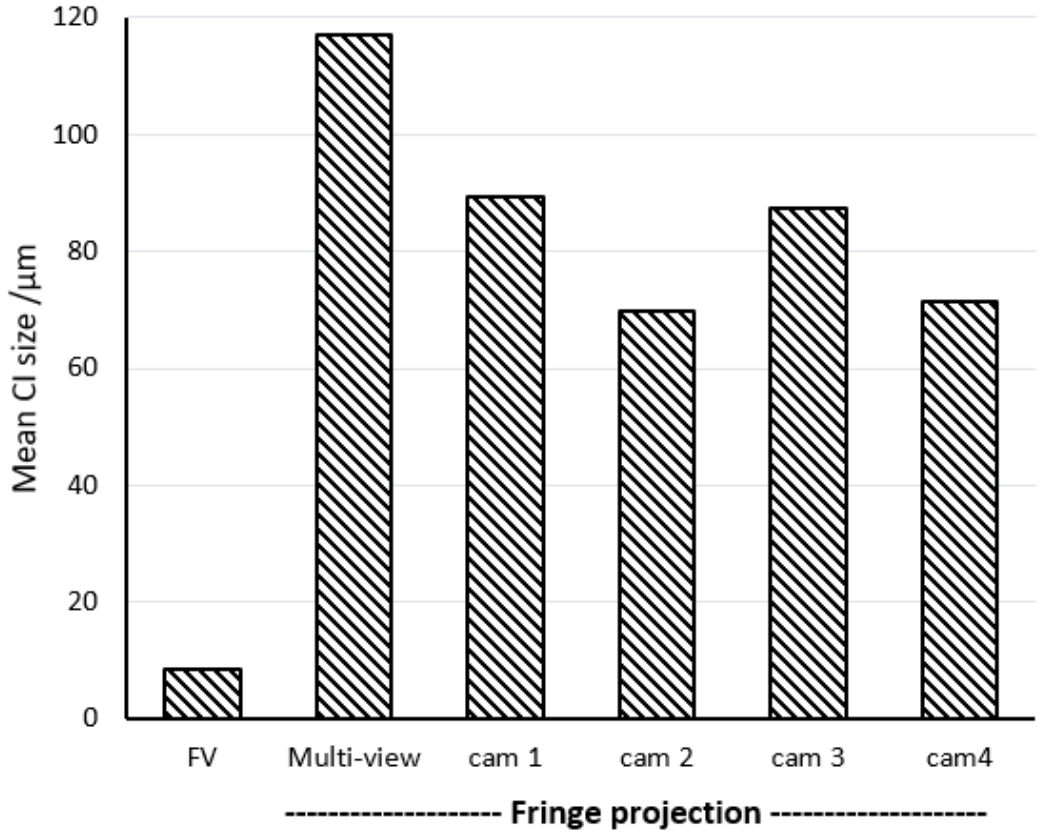

Figure 5.4.a. Mean CI widths for all measurement methods on both the L-PBF flat sample.

On the L-PBF flat surface, particles and possibly spatter formations can be clearly shown positioned randomly over the surface, with a few larger singularities that have large heights. The higher resolution of the FV technique reveals the presence of some smaller formations (possibly individual particles) that are also scattered randomly over the surface. The FV measurement is shown in Figure 5.4.b.

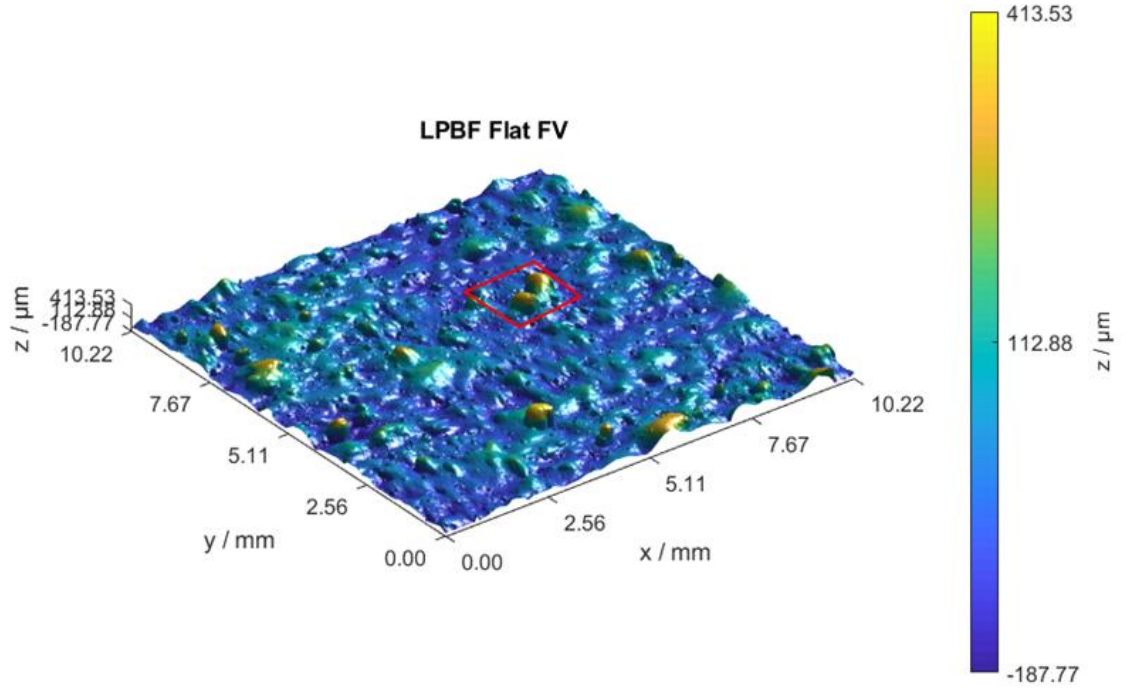

Figure 5.4.b Surface topography height map from the L-PBF flat top surface measured with FV. The highlighted red square represents a cropped region used to evaluate some smaller features.

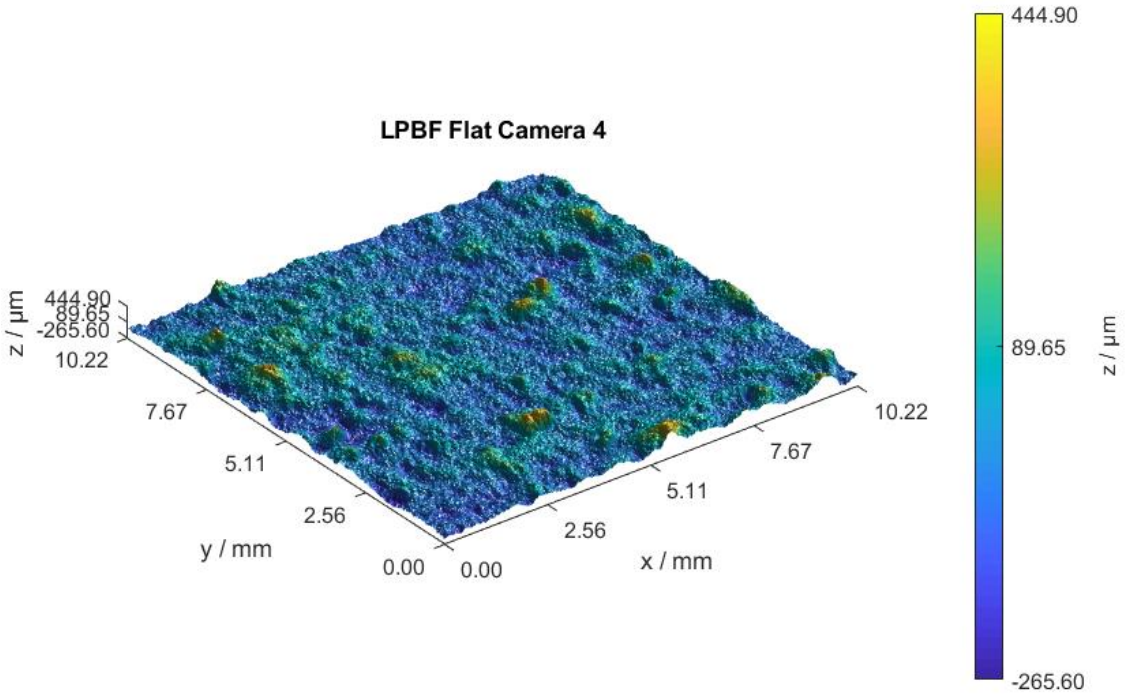

Figure 5.4.c Surface topography height map for the L-PBF flat top surface, measured with single-view (camera 4) of the FP system.

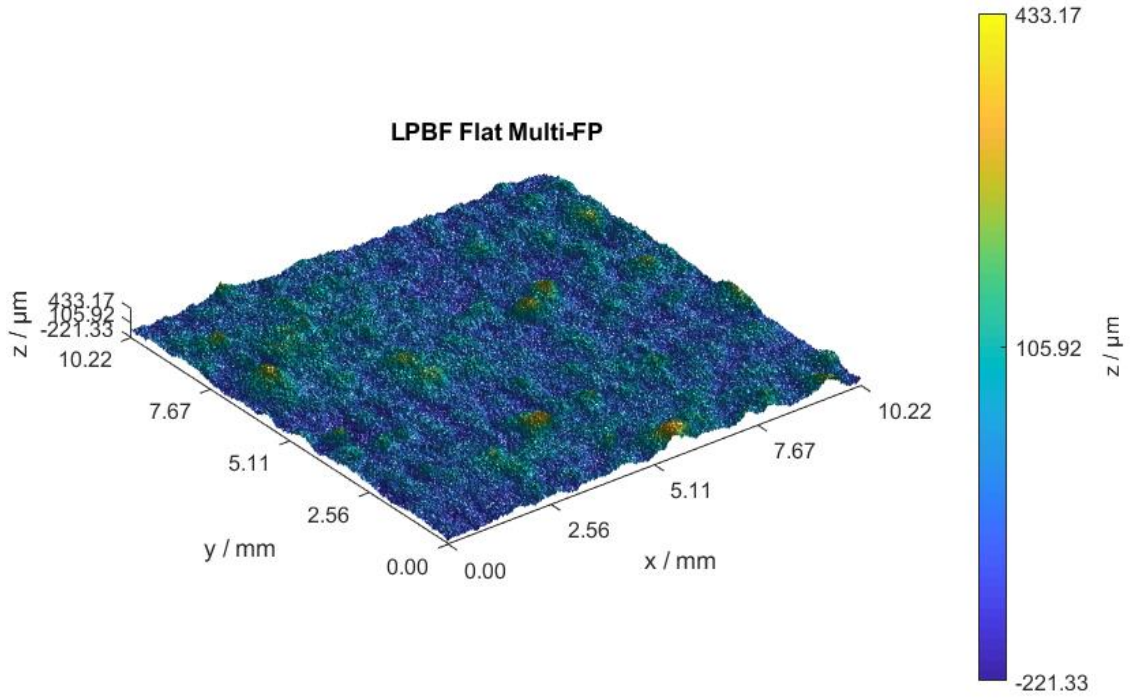

Figure 5.4.d Surface topography height map of the cropped region on the L-PBF flat top surface measured with multi-view FP.

In Figure 5.4.c, the single-view FP cropped measured topography from camera 4 of the FP system can be shown, taken approximately from the same surface region as the previous FV measurement. There is a higher amount of measurement noise, which were reduced with an 800 µm low pass filter (the filter was not applied in the figure). When compared to the FV measurement, there does seem to be clear topography similarities in relation to the surface features at larger scales, with many of the larger protruding formations (particles or spatter) clearly visible. It is only at the smaller scales in which the noise in the FP dataset decreases the reconstruction fidelity of the smallest particle features.

The multi-view FP cropped measured topography of the L-PBF flat can be shown in Figure 5.4.d, this dataset is made from adding the measured point clouds of the four camera-projector pairs together and applying a filter, as a result there is a balance between increasing point density adding points that might create a noisier datasets and smoothing that removes too much detail. When compared to the FV topography shown in Figure 5.4.b, the larger features can be clearly distinguished between the two topographies, but

there does appear to be a loss of fidelity in the FP data – even after data fusion is performed – that is likely due to the inherent resolution limits.

5.4.2 Comparison of individual features

Before looking at the larger regions of the surface, it is important to evaluate the ability to observe the particle features individually and whether their boundaries are effectively determined. From the larger surface region, a (3 × 3) mm region was cropped to evaluate a smaller topographic feature on the surface, this region is defined by the red square in Figure 5.4.b. Within the cropped regions, the differences between the FV and single-view FP measurement results can be visualised in terms of the volumetric difference between the two topographies.

Figure 5.4.e (a) shows the comparison between the FV measurement in grey and the single-view FP measurement in green. The FV measurement is relatively smooth and the FP measurement is noisier at high spatial frequencies across the cropped measurement region but does appear to match the FV topography at lower spatial frequencies, suggesting that a low-pass filter might be useful to improve the correspondence. A similar conclusion may be drawn by observing the topography cross-section marked by the orange line in

Figure 5.4.e (a) and shown in

Figure 5.4.e (b). However, the FP data does seem to underestimate the heights of the tops of the protruding formations (spatter and particles) in comparison to the FV measurement data. Looking at the agreement between the two topographies we see that the same particles/spatter features are found in both topographies even though the FP measurement has a visible high frequency noise component.

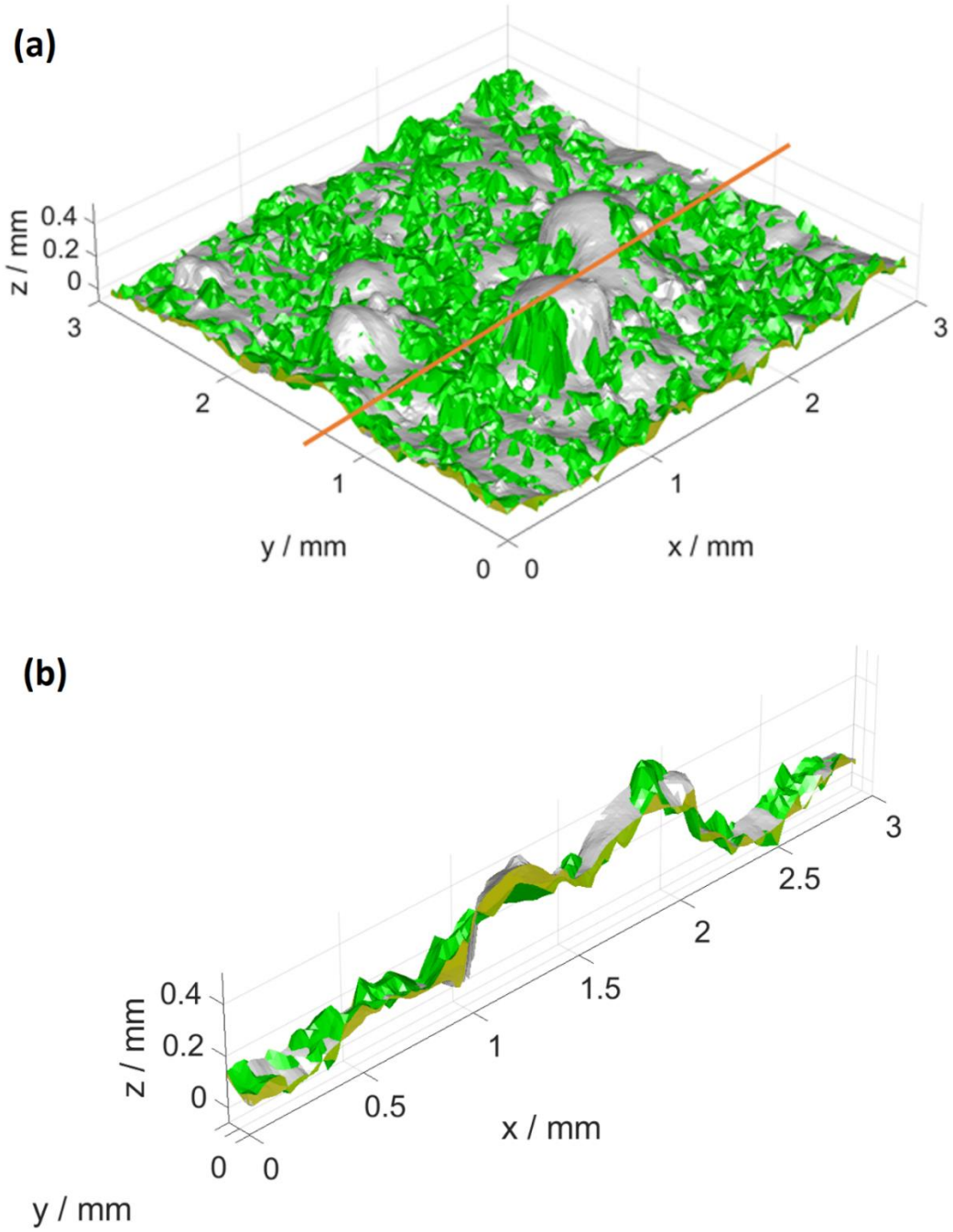

Figure 5.4.e Volume differences for (a) cropped (3 × 3) mm region for an example single-view FP topography (green) and against the FV reference topography (grey) with (b) a cross section (0.1 mm width) along the dominant feature shown. The yellow shows the volumetric difference between the two topographies.

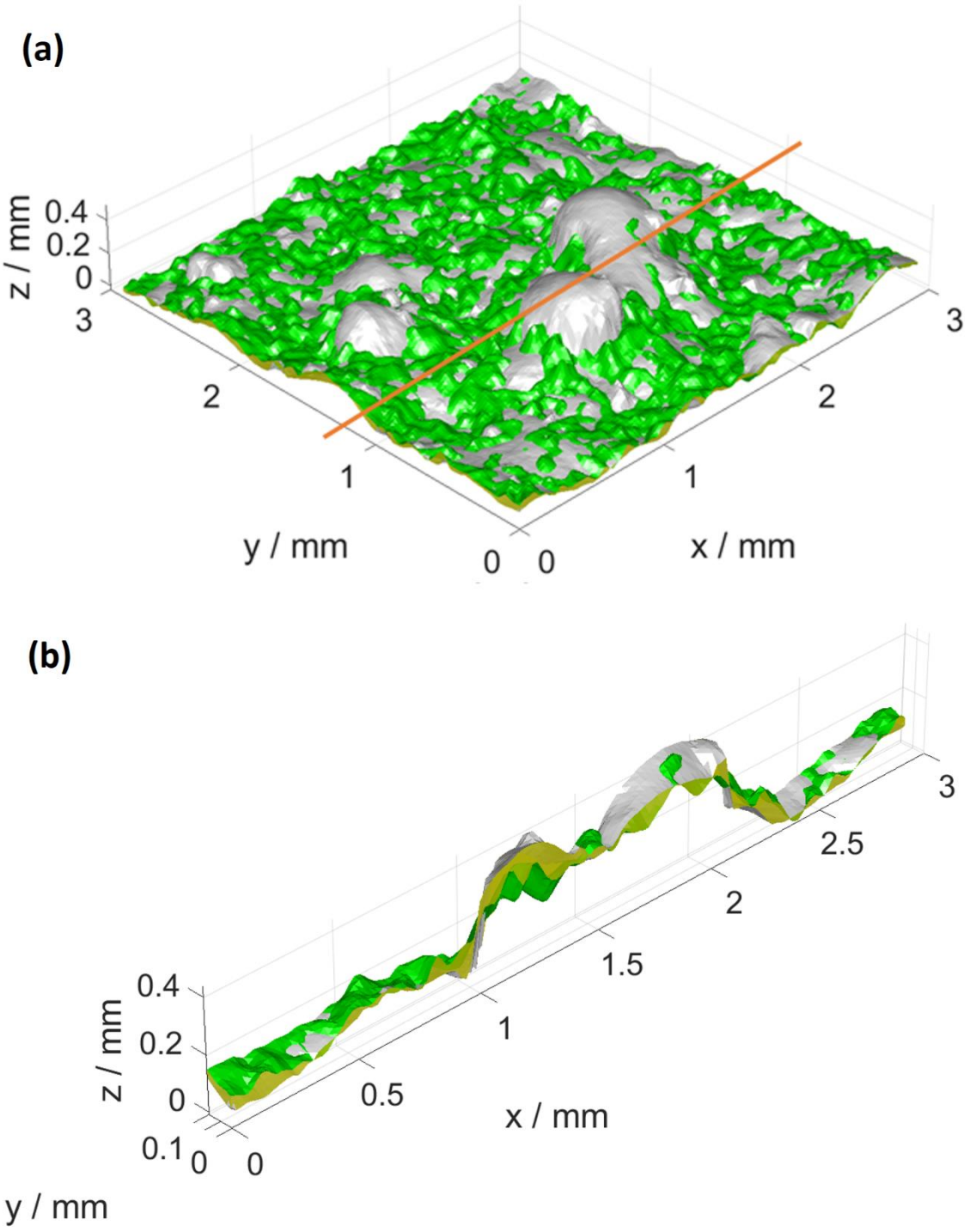

Figure 5.4.f Volume differences for (a) cropped (3 × 3) mm region for multi-view FP topography (green) and against the FV reference topography (grey) with (b) a cross section (0.1 mm width) along the dominant feature shown. The yellow shows the volumetric difference between the two topographies.

In Figure 5.4.f, the volumetric comparison between the measurements of the FV reference measurement (grey) and the multi-view FP measurement (green) is shown. To generate a multi-view FP point cloud, the single-view point clouds are simply aggregated without smoothing or resampling, leading to local high frequency noise. To reduce this high frequency component, the multi-view FP measurement is subjected to a low-pass filter. There is disagreement of the results over the whole topography in Figure 5.4.f (a) as in the single-view FP case, however in the multi-view case the spikes are clearly removed by the low-pass filter. For the cross section in Figure 5.4.f (b), there is disagreement over the heights of the top of the particles, which could be due to the multi-view FP data having the potential to be distorted by one or more of the single-view FP measurements. In terms of the features found on both topographies, there is a agreement on the larger features, and like with the single-view FP topography, there is increased noise in the FP measurement which obscures some of the smaller features.

5.4.3 Whole surface evaluation

5.4.3.1 FBC results

The FBC procedure outlined in section 5.3.4 was applied to all topographies, with the output segmentation mask for the reference FV data shown in Figure 5.4.g. On this mask, the algorithm seems to have been able to segment all the largest features and many of the smallest particles on the surface. Whilst the FV result is here taken as the reference, there will be limitations in how successful the segmentation algorithm is able to determine these feature boundaries which might be improved later. However, it is only the smallest particles that are either not being identified or partially identified.

For the segmentation mask for a FP single-view system (Figure 5.4.h), the segmentation algorithm is also able to identify many of the same features as shown in the reference segmentation mask, however the effect of the noisier measurement data means that the feature boundaries are not well defined and some of the smaller features are not discernible from the background.

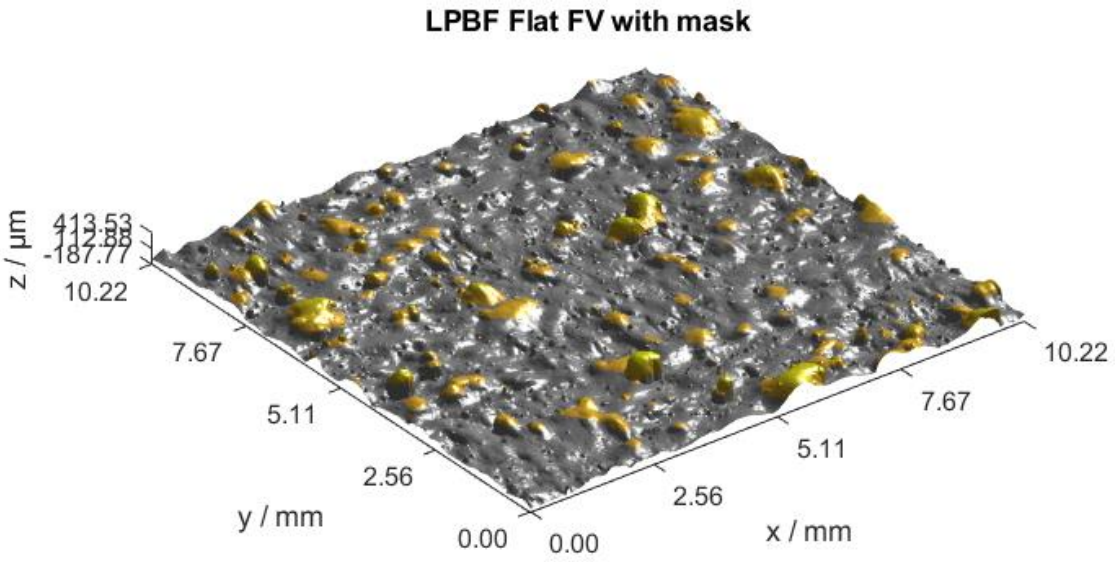

Figure 5.4.g Segmentation mask for the L-PBF flat surface measured with FV. Yellow indicates feature points determined through the segmentation approach.

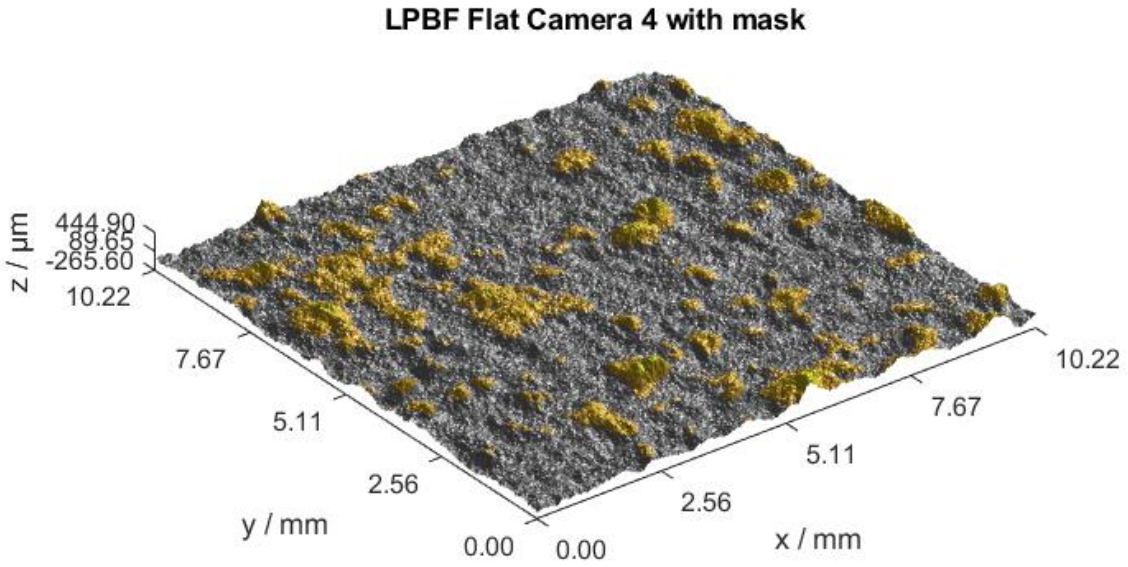

Figure 5.4.h Segmentation mask for the L-PBF flat surface measured with the single-view (camera 4) FP. Yellow indicates feature points determined through the segmentation approach.

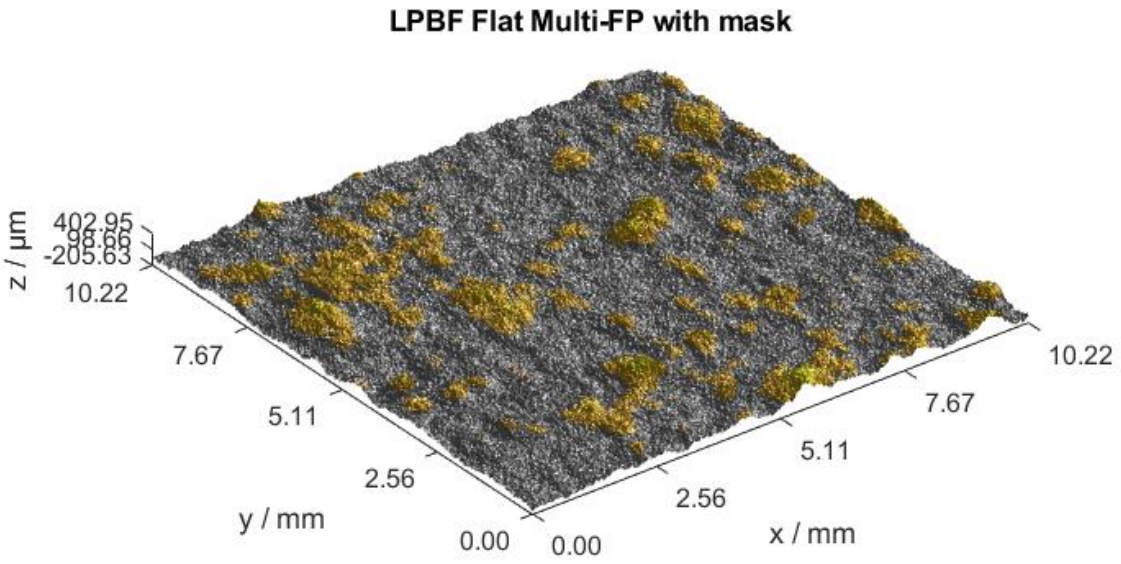

Figure 5.4.i Segmentation mask for the L-PBF flat surface measured with the multi-view FP. Yellow indicates feature points determined through the segmentation approach.

Figure 5.4.i shows the segmentation mask for the multi-view FP measured topography, whilst this is made from the combination of all the camera-projector pairs, it is still limited by the resolution of the FP system when compared to FV. As a result of this reduced resolution, the smallest features are still not detected by FBC when compared to the FV measurement.

5.4.3.2 Comparison of FBC results

Using binary classification testing with the FV segmentation result as a reference 'truth', the differences in feature segmentation can be visualised to compare the accuracy of same segmentation approach on similar features found by both segmentation masks, as well as to generate quantitative metrics. Figure 5.4.j shows the results of the single-view FP (camera four) segmentation result compared the FV segmentation result on the overlaid FV measurement. From the result it can be see that many of the larger particles are found also in the FP segmentation, shown as the large amounts of true positives, indicated in yellow in the figure. The FP measurements frequently over estimates boundaries in the FP result where big particles are close together (this can be seen in the detection masks for all camera measurements in Appendix A2), which is represented by the swathes of light blue that often connect particles together (light blue is used to indicate false positives, i.e. features recognised as such by FP, which are not labelled as features in the

FV result). Some of the smaller particles are not identified by the FP segmentation (false negatives, shown as red regions on the surface), with some of boundaries of small features also not completely identified – also false negatives, resulting in red regions around a yellow centre. It is also clear that there are missing particles that can be seen as not identified by either the FV or the FP (coloured in grey) – so there is a limitation of this segmentation method in identifying the very smallest features. Most of the discrepancies between the two results are due to the higher measurement noise in the FP topography, meaning it is likely that smaller particles, points around the slope of the particles, or particles with lower relative height aren't as clearly defined and are therefore not identified in the FP segmentation result. When comparing particles that are identified as features on both topographies – that is, the true positive features – there are some particles that are approximately 200 μm in diameter that are detected. Many of the smallest particles (< 100 μm diameter) aren't identified on the reference surface as features, so there is room to improve the segmentation approach.

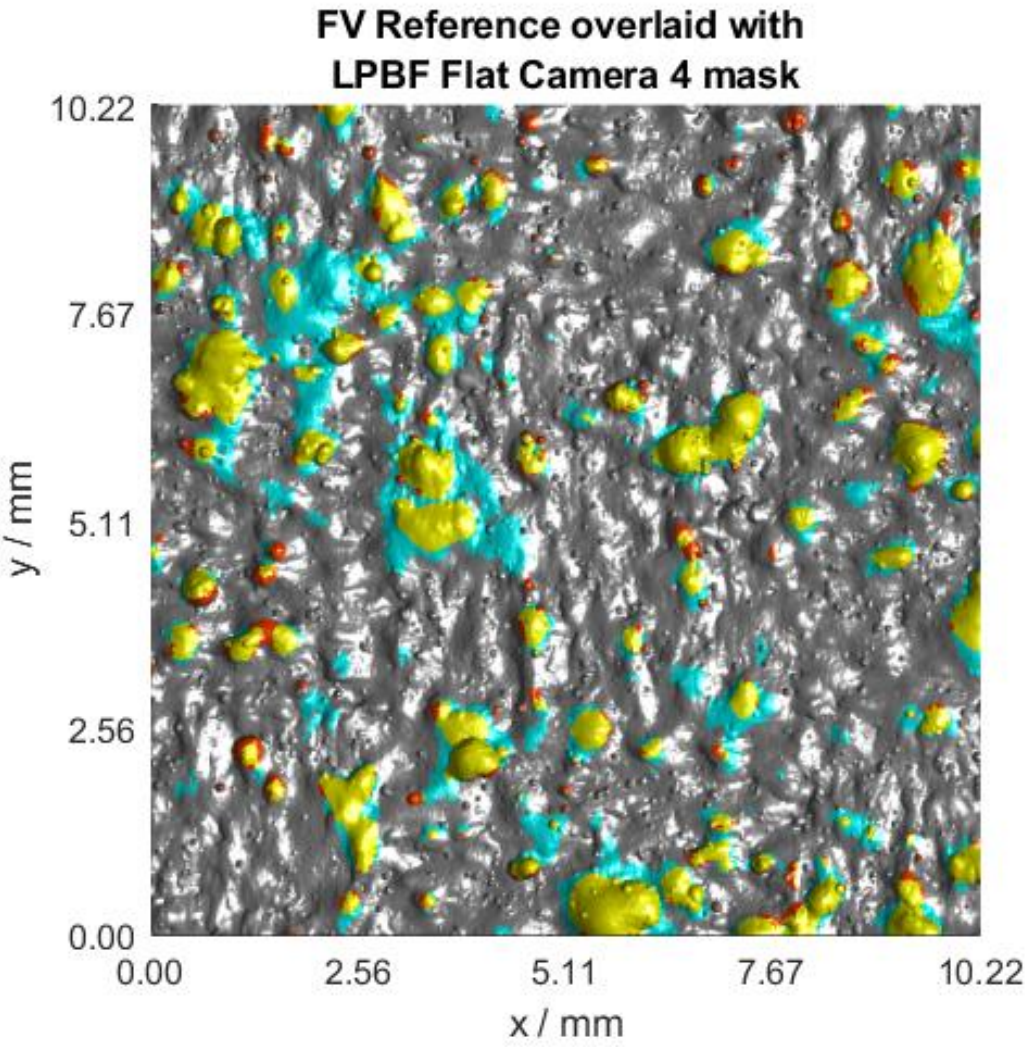

Figure 5.4.j Binary classification results of the single-view FP (camera four) segmentation masks compared to the FV reference. Yellow indicates matched feature points (true positives), red shows missing feature points (false negatives) and blue shows the excess feature points (false positives) all between the reference and measurement segmentation results.

For the multi-FP comparison in Figure 5.4.k, we see much of the same results as for the single-view FP comparison, but with some small improvements. With the measurement noise reduced for the multi-view FP topography, there is a lower number of missing points (red points) around the boundaries of particles than in the single-view FP case. In some cases, while there are still connected regions where lots of particles are present, the outer boundaries appear much smaller reducing the number of excess points (light blue) however, at the same time there are some regions where more points have been

determined as features in the multi-view FP result meaning there are more matching points and less missing points, but also excess points connecting other clusters of features together. There are still some points that haven't been identified at all in the multi-view FP segmentation result, which suggests there is an inherent limit to the size and scale of features that are detectable. As with the example for the single-view camera, the particles identified as features on both topographies are approximately of the size of 200 μm in diameter. Many smaller particles (< 100 μm diameter) weren't identified on the reference surface as features, however, improvements to the segmentation algorithm might not be sufficient to separate the feature from noise on the noisier multi-view FP topography. From observing all the FBC detection masks for both FV and FP measurements (Appendix A2) and the deviation maps of the FP measurements from the FV standard (Appendix A1) it is apparently that all the FP measurements have difficulty with clearly identifying the edges of features on the surface. As previously seen from the line profile presented in Figure 4.3.g, high frequency features measured over the surface have a tendency to be skewed depending on the position of the camera perspective, which appears to be particular exaggerated in cameras 1 and 3 for these measurements. For the larger features on the surface, this is mostly averaged out from the data fusion of the multi-view FP data, as the skewing from each perspective is averaged out from the others. This results in the larger particle boundaries being noisier around the perimeter on the multi-view FP data than the single-view FP data, but more closely matching the FV in terms of position and area. In some regions however, individual point clouds from a single camera can have a disproportionate effect on the multi-view, which results in features being overestimated by the multi-view measurement in comparison to some of the single view perspectives.

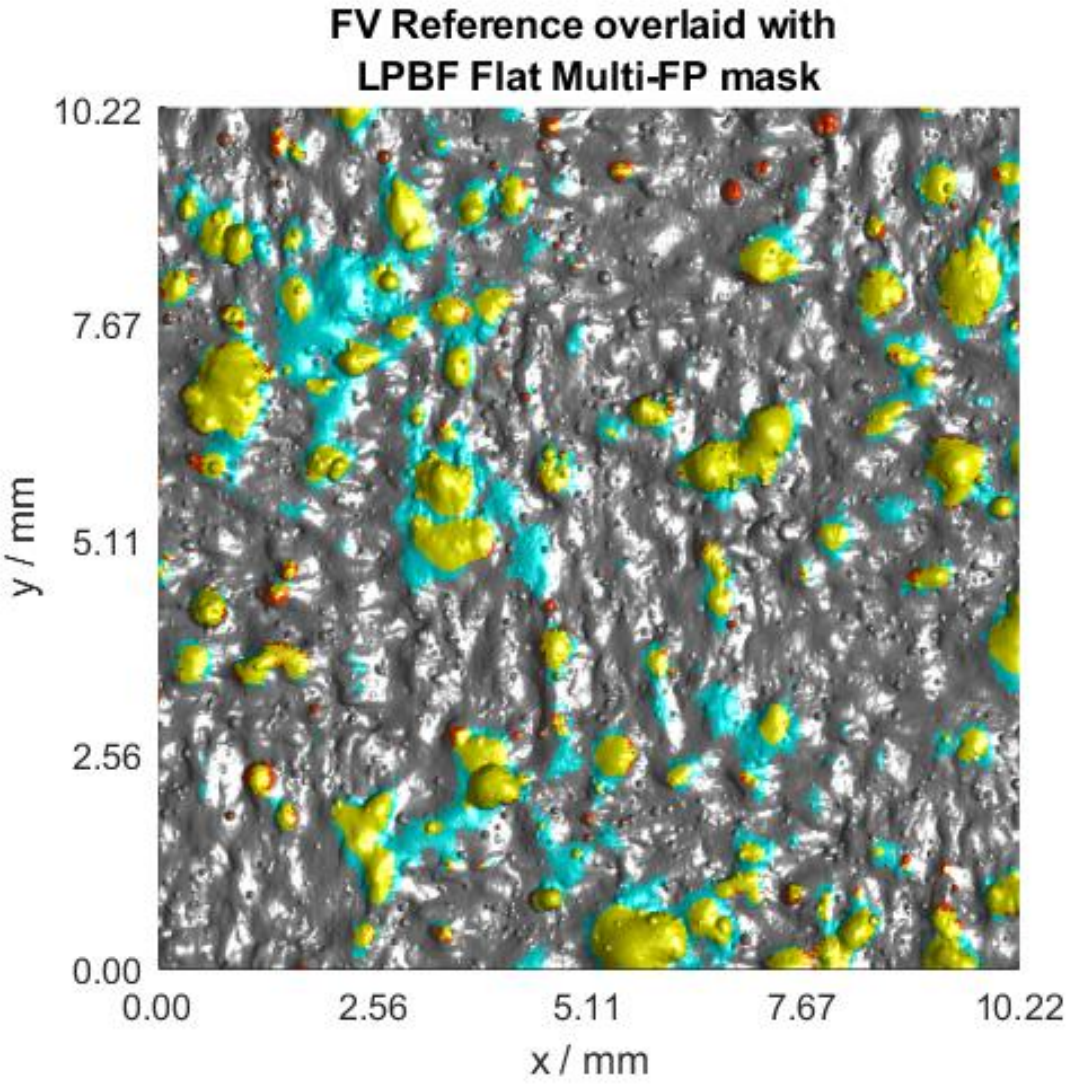

Figure 5.4.k Binary classification results of the multi-view FP segmentation masks compared to the FV reference. Yellow indicates matched feature points (true positives), red shows missing feature points (false negatives) and blue shows the excess feature points (false positives) all between the reference and measurement segmentation results.

Number of detected features, median feature area and maximum feature area for all measurements are given in Table 10. From these numbers it can be seen that the FBC detects more particles on the multi-view FP measurement, which more closely aligns with the number of particles detected on the FV measurement. The median feature is also lower on multi-view FP, meaning that more smaller features are being detected. This is further confirmed by the histogram plots in Figure 5.4.l that show the number of particles detected per particle area. On the smaller end of the particle sizes the histograms of the

multi-view FP data more closely resembles the histogram for the FV data, where the single view FP measurements have more particles spread amongst the size ranges. Although it is worth noting that these smaller particles that have been detected in the multi-view FP measurement are somewhat due to the particle boundary noise caused by the fusion of the four point clouds, and are not necessarily the same smaller particles that the FV system is capable of measuring.

Table 10. number of features detected, median feature area and maximum feature area for each measurement.

Ti-flat sample	**FV**	**Multi-view FP**	**Single-view FP**			
			Cam1	Cam2	Cam3	Cam4
Number of features detected	141	123	106	98	95	105
Median feature area /μm^2	41600	25200	52000	53600	61600	60800
Maximum feature area /μm^2	839600	5131600	6477600	4017600	6367600	4360000

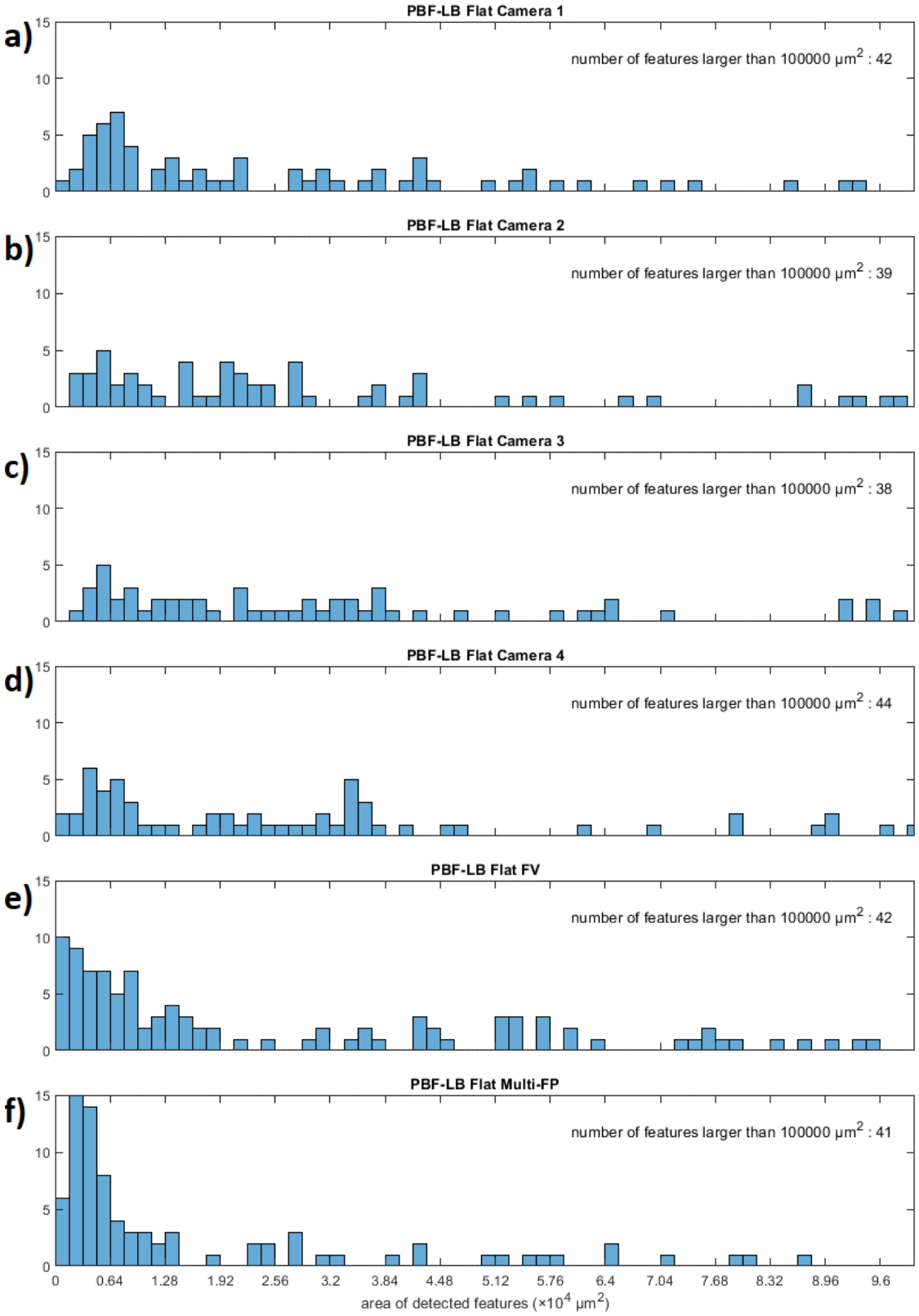

Figure 5.4.l Histograms of featured detected by area for each of the measurements. Minimum quantifiable area is 400 µm^2 due to the 20 µm lateral resampling of all data sets.

From the binary classification results shown on the topographies, the metrics for balanced accuracy, precision, recall and specificity can be computed for each comparison of each single-view FP measurement and the multi-view FP measurement to the FV reference. There is a reasonably high balanced accuracy result for all single-view results, with a slight increase of performance for the multi-view FP result – with the average results of recall and specificity being also high. There are fluctuations between all single-view FP systems but no apparent significant differences. The precision score is relatively low, suggesting that there is a large proportion of excess feature points when compared to the true positives. This is evident in the visual topographies when looking at the excess points around closely located true feature points, however these excess feature points appear to agglomerate and over-define the boundaries of feature – which is likely a result of reduced resolution in the FP measurement data. To improve precision, the FP measurement will require increased resolution to better define the edge of the particles which will then benefit the segmentation algorithm in determining the feature boundaries. The specificity score is high, implying a small number of excess feature (false positive) points as a proportion to all negative points. The reason for this high score relates to the localisation of false positives around existing features – so while there are excess points, they are not dominant across the whole surface. The recall metric is the highest scoring metric, which is the proportion of correctly identified feature points. This can be seen in the earlier figures (Figure 5.4.j & Figure 5.4.k) as low amount of missing feature points in red scattered across the surface. Improvements to this score will likely come at a cost to precision, as to reduce missing feature points will require the segmentation algorithm to increase its prediction of regions containing (true) matched feature points will mean that many overpredictions are made – which will affect its balanced accuracy.

Across all metrics but precision, the multi-view FP system scored higher than all single-view FP results, suggesting that the use of multiple views is beneficial in increasing the quality of information in the resultant topography. The high score for most metrics for all single-view FP systems suggests a reasonably well positioned location for measurement with improvements more likely attained through more advanced instrumentation.

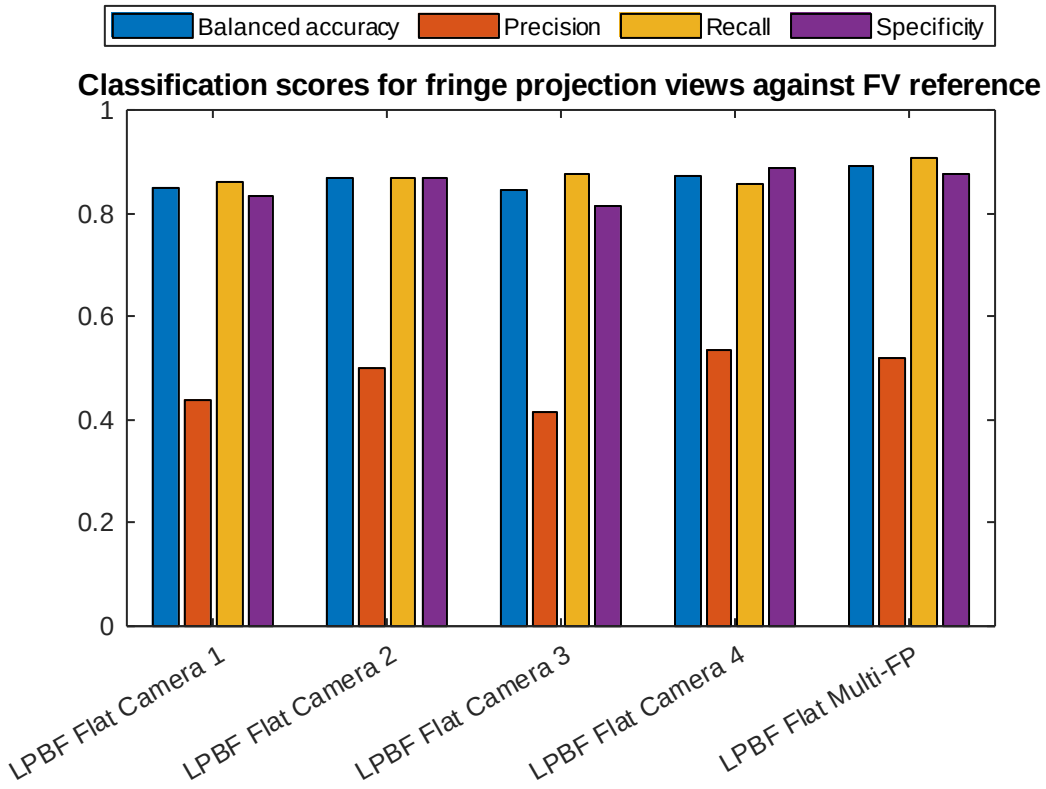

Figure 5.4.m Binary classification metrics for the various single-view FP and the multi-view FP segmentation masks when compared to the FV reference segmentation masks.

5.5 Feature based characterisation discussion

Whilst particle and spatter features were considered, there is no real limitation to using feature-based segmentation to target other features of interest, perhaps such as the weld tracks or even pores on the surface. The only requirement to achieve segmentation would be manual configuration of the FBC process to adapt the algorithms to isolate these different features. However, the analysis method outlined in this work could still be applied to validate and verify the segmentation methods on the same surface measured with the different technologies.

Between the two techniques, it is clear that the factors that influence measurement uncertainty (difference in the topographic resolution among the most significant) lead to increased error and uncertainty found on the measurements of the FP system when compared to the FV measurement system, with there being additional differences between the measured topographies in terms of spatial frequency components. These differences

in measurement uncertainty would also become clear in any measurement parameter computed on the surfaces. The noise component on the FP measurement is rather dominant and is close to the scale of the individual particles so there is need for improvement in the instrumentation of the FP system if it is to be used for this form of analysis.

In general, the ability to evaluate the errors between feature-based parameters or dimensional properties is not so important as the use of in-situ assessment is mostly required to instantly detect issues that might generally affect the build, which does not require highly accurate datasets that closely match 'true surface'.

The presented comparison method does require a reference. In this work, the reference is biased to the FV data where the resolution is sufficiently higher than FP. This analysis might benefit from use of a manual segmentation mask applied to the FV measurement data as in earlier work [230].

5.6 Feature based characterisation conclusions

The same L-PBF surface has been measured with two different measurement technologies, resulting in an FV reference measurement, four single-view FP measurements and a single multi-camera FP measurement. The same segmentation method was applied to all measurements which was then compared to qualify and quantify the differences between the features identified on the FV reference and all the FP measurements. The following conclusions can be drawn from this work:

- The specific segmentation approach results in low precision and high specificity and recall for all measurement datasets compared to the reference, implying that the FP method over-estimates regions containing true features by a far margin, which might be suitable for a quick assessment of particles.
- FP in the tested configuration is more than capable of resolving larger agglomerated spatter/particle features present on a PBF surface, however clearly limited at observing individual particles from the process.
- Generally, spatter/particle features can be resolved and segmented from the FP data and that features could be characterised down to a size of approximately 200 microns.

- FBC performance can be assessed and improvements can be suggested based on the use of classification scores and visualisation of the matched features between topographies.

6 Discussion and concluding remarks

The aim of the work that has been presented in this thesis was to develop an in-situ monitoring system for metal PBF capable of measuring and identifying manufacturing defects over the entire powder bed. The achieve this goal, a suitable method of measurement has been identified, an out of machine prototype has been developed and tested, and a potential methodology for processing the data and identifying defects has been explored.

6.1 Multi-view fringe projection system findings

As an in-situ inspection system for AM, multi-view FP appears to be well suited due to its non-contact nature and rapid acquisition rates. The system that has been designed can collect all of images needed for a measurement within 1.1 seconds, using 18 frames per camera, using the hardware selected and software synchronisation between the cameras and the projector. The limiting factor in the acquisition of the data comes from the frame rate of the cameras used, and in theory could be decreased further with higher framerate cameras and hardware synchronisation with the projector. Data collected from the system so far has shown that multi-view FP has the potential to be a valuable tool in the detection of layer-wise surface features and defects generated during the metal PBF process.

6.1.1 System resolution and repeatability

The resolving capabilities of the multi-view FP system has been assessed in this work through two main methods of analysis, point cloud point spacing, and repeatability of the measurements. Although these two factors are not synonymous with resolution, and do not fully describe the systems resolving capabilities, they are related to the systems performance and do provide an insight into where the systems limitations may lie. Three different hardware configurations of the multi-view FP system have been tested through this work:

1. Projector: 4K Optoma UHD550X, Cameras: 18 MP Canon DSLRs.
2. Projector: 4K Optoma UHD550X, Cameras: Basler ace acA572–17um.
3. Projector: DLP Lightcrafter 6500, Cameras: Basler ace acA572–17um.

With each of the new hardware configurations the FoV of the projectors and cameras also varied due to different lenses between models, and differences in how the hardware was positioned within the system. Between hardware versions 1 and 2, the projector remained the same but was not moved. Between versions 2 and 3, the camera model remained the same, but their positions were changed to achieve a smaller FoV on the measurement area.

6.1.1.1 Fringe projection point spacing

Mean point spacing was assessed using data from all three versions of the system, with the mean point spacing of the multi-view data being 59 µm, 74 µm and 35 µm respectively. Although the resolution of the cameras being used between versions 1 and 2 improved, the FoV was increased, which resulted in a higher mean point spacing. The FoV between versions 1 and 3 is more comparable, and in these two systems a significant improvement in point spacing is observed, although this can be attributed to not only improved cameras, but also a shift to an industrial machine vision projector over the original cinematic one. Examples of each of the systems FoV can be seen in Figure 3.3.b (version 1), Figure 4.2.d (version 2) and Figure 5.3.a (version 3). In all cases the mean point spacing of the multi-view FP was roughly half that of the single-view counterpart, equating to four times as many points over an areal measurement.

In the context of system resolution, the mean point spacing acts as an effective lateral sampling rate when measuring mostly flat surfaces, as would be measured in-situ on a metal PBF system, although unlike other surface measurement systems these points are not positioned on an equispaced grid that is normal to the substrate. Known common features that occur during the metal PBF process include weld tracks (nominally 100 µm in width), elongated pores (50 µm to 500 µm), balling (up to 500 µm in width and potentially the length of the build) [25], unfused powder (100 µm to 150 µm) [195] and lattice deviations (up to 500 µm) [26]. To be able to measure these features on the surface, enough data points must be taken across the feature that they can be clearly resolvable from nominal. With the best point spacing achieved being 35 µm, it is unlikely that features down to 100 µm or less would be resolvable as only 2 or 3 points would be measured taken over the length of the feature. As more points would be measured over larger than 100 µm, they would be more easily resolved. As mentioned in section 3.1.2,

the target for the system was to resolve features under 500 µm in size, which is achievable with the demonstrated point spacing of all version of the system. The lateral sampling of the FP system is heavily dependent on the FoV of the cameras and the size of the CDD pixel array in the camera, meaning that smaller features would be better resolved on PBF systems that have smaller build areas when using the same hardware. For PBF systems with larger build areas, higher spec cameras with larger CCD pixel arrays would likely be beneficial.

6.1.1.2 Measurement repeatability

Repeatability of measurements was assessed on versions 2 and 3 of the system by running 5 measurements on the same sample, in the same position. Repeatability has been quantified by calculating 95% CI sizes across the surface for both the multi-view point clouds and each single-view perspective. From the data taken on version 2 of the system, the multi-view FP data had a mean CI size of 101 µm, and the four single-view data sets had a mean CI of 42 µm between them. For version 3, the mean CIs were 117 µm and 80 respectively. These numbers make the multi-view system appear to be less reliable than the single-view counterparts, however, when compared against a higher resolution FV measurement of the same sample, the multi-view system has a lower mean deviation over the surface in comparison to the single-view measurements (multi-view and single-view mean deviations being 67 µm and 83 µm for version 2 and 27 µm and 32 µm for version 3, respectively). Data from version 3 of the system is far more inline than version 2 when compared to the measurements taken from the FV system, which could be attributed to the stability of the updated projector. However, it is much more likely to stem from the difference in sample used on the two versions of the system. Where the sample from version 2 has surface form that lead to areas of potential occlusion from the different perspectives, the sample used for version 3 was flat in form, with only features resulting from the L-PBF process present on the surface. From the data taken on both versions of the system, the multi-view approach appears to have a higher level of accuracy in measuring the surface, with a lower level of precision. This decrease in precision is most likely due to the multi-view point cloud being a combination of the individual single-view perspectives, meaning that errors from the single view perspectives are combined all combined into the multi-view point cloud, causing a resultant averaging affect over the measured regions, but a greater level of measurement noise.

An apparent issue with the multi-view data fusion approach is the significant impact that inaccuracies of an individual or multiple point cloud from the separate perspectives can have on the overall combined point cloud. This has been seen in all three versions of the system, with a point cloud having to be removed from the multi-view dataset in Chapter 3, skewing of the wave features profiles being clearly visible in individual point clouds in in Chapter 4 (Figure 4.3.g), and a similar skewing affect causing smaller features to agglomerate in the FBC of Chapter 5 (seen in Appendix A where skewing is present from the deviation maps in all four cameras, but is significantly more present in cameras 1 and 3, resulting in detected features being significantly skewed and oversized in comparison to cameras 2 and 4). Due to the data fusion method being an alignment of the four individual point clouds, these individual perspective errors propagate through into the multi-view point cloud. Optimisation of camera positions for the highest quality data and smarter data fusion methods may need to be developed to help reduce errors caused by the skewing of high frequency features by differing perspectives.

With the system CIs being up to 100 µm in height, there would likely be some difficulty in measuring features that protrude from the powder bed layer around this amount or less. However, these CI results are without any noise or data processing other than a statistical outlier removal to the raw point clouds. The CIs could potentially be decreased with further noise removal or smoothing filters being applied to the data. With the mean variation from FV data being as low as 27 µm and an adequate noise removal or smoothing operation carried out on the data, it's possible that the system could reliably measure smaller variations in height across the surface. Measurement noise in FP data is also partially dependent on the relative angle of FP with respect to the camera's perspective [249]. Optimisation of both hardware positions and projected fringe angle could reduce measurement noise in the individual perspectives point clouds, which would result in a lower level of noise in the multi-view point cloud. However, with the spatial limitations present in a PBF system, and the simultaneous optimisation of four different camera projector pairs, this would not be a trivial task.

6.1.2 Feature based characterisation suitability

FBC has been explored as a potential method of identifying features and defects using the multi-view FP method. With an adequate feature identification method on an in-process

monitoring system, the potential for automatic defect flagging becomes a possibility which would be essential for commercial manufacturing defect prevention. Automatic feature identification would also be beneficial in research applications for tying features on the surface to processing phenomenon with relative ease compared to manual data processing.

This first attempt at the use of FBC for multi-view FP data has proved promising, with results showing that surface particles of 200 µm in size can be consistently highlighted by the chosen algorithm, but as particles approach a size of 100 µm or less the success rate of detection begins to drop off. This means that the system has achieved it's specified target of identifying sub 500 µm features, but there is still room for improvement if the identification of smaller features such as weld tracks, unfused powder and smaller pores is desirable. This limit on the size of detectible features falls in line with the mean point spacing calculated from the data collected, as if there are not enough sampled points across a feature of interest, then it's shape, size and position will not be resolved well enough for a detection algorithm to pick up on it. As a low pass filter was applied, the high frequency noise of the multi-view FP data was reduced in comparison to the single-view data. This reduced noise, in combination with the higher lateral sampling due to a denser overall point cloud, made the FBC algorithm able to better define the edges of detected particles compared to the single-view data. This could be seen in how the single-view data was more likely to overestimate the size of particles, or to group near particles together, although this still happened with the multi-view dataset, but to a lesser extent.

The successful identification of features present on the FP data when compared to a higher resolution FV measurement prove that the data collected from the FP system contains valuable information that can be extracted through automated data processing algorithms. Whilst particle and spatter features were considered, there is no real limitation to using feature-based segmentation to target other features of interest, perhaps such as the weld tracks or even pores on the surface assuming that the resolution of the system is able to measure them. The only requirement to achieve segmentation would be manual configuration of the FBC process to adapt the algorithms to isolate these different features. However, the analysis method outlined in this work could still be applied to

validate and verify the segmentation methods on the same surface measured with the different technologies.

6.2 Future work on the multi-view fringe projection method

6.2.1 Data processing for multi-view fringe projection system

Real-time and efficient big data analysis represents a key issue for the development of closed-loop control [140,154,250] and/or in-situ defect correction and removal techniques. The lack of consolidated real-time implementations still represents one of factors contributing to the existing gap between the wide research in this field and industrially adopted solutions. This is a field where several research efforts and industrial developments are currently required.

The data processing used through the work presented in this thesis has generally been a slow and manual process. The raw point clouds had a SOR filter applied in CloudCompare [251], before having a fine alignment of the four point clouds in Polyworks Inspector [229] and finally a conversion to height map format, followed by FBC algorithm, in Matlab [224]. This data pipeline in labour intensive and time consuming, making it unrealistic for use in a real manufacturing system, which could potentially be taking a measurement every layer of a build. For an in-situ measurement system such as this to work as part of a functional automatic detection method, these steps must be combined into a single, robust piece of software that performs the data processing immediately after the point clouds have been generated. Most of the work presented has been with minimal data filtering or smoothing, meaning that a lot of noise is still present in the final surface measurement. For the system to perform its best for a given application, data filtering methods should be chosen to give optimal measurement performance so that features of interest can be better measured once identified.

For future work, FBC methods need to be developed to work at higher speeds or even to provide real time segmentation and analysis to allow for their implementation in-situ. FBC work has been performed on height maps converted from the raw point cloud format output from the FP system. This has only been performed on small regions of interest rather than the entire point cloud for the sake of comparisons against a FV system, which natively outputs height map data. The conversion from point cloud to height map is a

computationally demanding process than requires a significantly amount of time even for the small regions used in these studies, and this time would scale poorly as the area of measurement increases. Both for processing time improvements, and to minimise information lost from the resampling process, it would be better if a FBC designed for use on point cloud data were applied. Feature detection methods have been applied to point clouds for a variety of applications such as sharp edge detection [252,253], terrain analysis with tree and building detection for UAV data [254] and subtle feature extraction, such as weld seems over large parts [255,256]. Other future work would explore the accuracy in height extraction rather than lateral particle size, so that features can also be characterised based on height, this could enable the detection large particles/structures that might damage the wiper blade within the PBF process.

Another approach might be to explore machine learning for feature detection, using FBC-produced masks as training data to allow for an increase speed in feature detection, where there can still be an external additional verification step using the principles of comparison and validation applied in this work. Machine learning has been applied to point cloud data for object detection and segmentation, both on raw point clouds and on volumetric grid data sets converted from point clouds [257,258]. These algorithms have successfully been trained to identify geometries that are relatively complex in comparison to those expected on a L-PBF, such as office furniture, buildings and people [259], and have even been used for real-time object detection with applications like autonomous driving in mind [260].

An issue that has arisen from the current system is the size of the data collected per measurement. For each single measurement, four individual point clouds are collected which range from 400MB to 800MB for the data sets used in this thesis. With a lower estimate, this means 1.6GB of raw data per measurement without any data processing or conversions being carried out. On a real L-PBF machine, build layers are typically less than 100 µm in height, meaning that over a 100 mm tall build over 1000 layers are processed. If the in-situ monitoring strategy was to perform a measurement every single layer then this would mean that 1.6TB of raw data would be gathered over only 100 mm of height. For one of research applications this could be acceptable to allow further understand of the metal PBF process, but in a commercial environment it would be

unrealistic and extremely expensive to store this amount of data for every build. To target this issue, different data handling methods must be assessed to reduce the saved data to an acceptable size, such as raw point cloud compression, selective sampling strategies (measuring every n layers, or using the FP system as a high resolution investigative measurement once another monitoring system has flagged a potential issue) or data processing pipelines that identify and store the location and sizes of features of interest only, and deleting all non-significant regions of the point cloud. For these strategies to be successfully developed, further work into the relationship between process generated features and part quality must be performed so that the process can be tailored to target only features of significance with an adequate sampling rate.

Throughout this thesis all data present has been of sampled placed in the central region of the powder bed region. As mentioned in section 3.1.2, the depth of focus of the cameras will have an impact on the data quality due to the angular perspective of each camera in the corner of the system. Although the central region of the powder bed would be in focus for all 4 of the cameras, each of the corners of the powder bed will only be in focus for 2 of the cameras. This would result in a loss of resolution/data quality from the centre to the corners of the powder bed that has not been explored in this work. For this system to be robust for full powder bed monitoring then one of the following must be done:

1. The camera position optimised to achieve an in focus image from all cameras across the entire powder bed without obstructing the PBF systems function.
2. The cameras fitted with different optics, such as tilt lens, to achieve a plane of focus that is not normal to the cameras line of sight.
3. Further analysis on the impact of varying focus across the powder bed to determine the limitations of the current configuration as parts are built away from the central region.

6.2.2 Implementation in a real PBF system

Although the system described in this thesis is intended for in-situ monitoring on metal PBF systems, it has currently only been built and tested as an out-of-machine lab prototype. Future work needed on the system involves integrating the hardware into a real PBF machine to collect in-situ data. The ground work for this has been laid out by Remani et al. [261], who will be continuing on the project within the Manufacturing Metrology

Team at the University of Nottingham. Remani et al. also plan to use co-axial meltpool imaging and full field IR imaging of the powder bed to cross correlate data between the three monitoring systems to gain a greater understanding of the manufacturing process. The integration design has the machine vision cameras within the build chamber, surrounded by metal enclosures and replaceable UV filters in front of the lenses to protect them from harm during the lasing process. The projector is mounted above the build chamber, with an optically flat mirror reflecting the projection inside through a window in the build chamber ceiling.

The multi-view FP method has also been commercialised as a product for Taraz as their IM1 FP for AM system that can be configured as an integrated or free standing FP system [262].

6.3 Potential future applications

As research on in-process monitoring of additive systems continues, there is a clear trend towards developing a greater understanding of the influence input parameters may have on the build quality and final part properties. Many authors has explored how varying process parameters impact the build already assessing energy density levels per printed slice [38,39,68,69,79,80,178], thermal history throughout the build [95,96,99–101,179], process by-products [116,121,126,129,180,181], in-situ X-ray video imaging [130,132,182], meltpool characteristics [139,150,153,160,164,183] and acoustic emissions [98,133–136,177]. All these methods have shown that there are correlations between in-process data and the outcome of the part being built. Complex part geometries have also been assessed to determine how in-process signals correlate to the success of fabrication. These include the presence of presence of anomalies within the printed slice [37,49–51,55,69] and thermal histories [100,109,112,191] and meltpool properties [153–155] over thing walls and critical geometrical features. Understanding how the manufacturing system behaves over these geometries is essential as these kind of complex features and parts are one of the key benefits of AM over other conventional fabrication methods. Understanding these relationships is key to ensuring that metal PBF processes are manufacturing the highest quality parts possible. Having a more in-depth knowledge of what features and signals may contribute to a part failure once in service also allows for a catalogue features to be made by their severity of their impact on part functionality.

This would mean that for a given part with a specific function, a list of features can be labelled as true defects as they would be known to cause failure in service, where as other features would be known to has no impact on the parts function and can be ignored.

Once the additive process is better understood, a significant overarching aim that is apparent in the currently available literature is the ability to control the process in real-time and make corrective measures once a potential defect is identified. Methods of maintaining control over the process has been explored through a range of approaches such as distortion of CAD models to account for predictable thermos-mechanical effects [263–265], real-time high frequency adaptive control of the meltpool through the monitoring of co-axial signals [140,154,266], and remelting of the previous layer where defects have been detected as a corrective measure [84,97,142,267–269]. These preliminary studies into the application of control systems lay the foundation for future systems to that can adapt and correct all part threatening defects as they occur during the manufacturing process. A system of such design would require a wealth of prior information about defect formation and severity that could be applied when automatically analysing the data from a wide range of in-situ sensors.

A high resolution, full powder bed topographical measurement system that's capable of measuring and automatically highlighting features down to 100 µm in size would add a valuable new perspective to the already growing wealth of information being output on the subject. Systems such as the NIST Additive Manufacturing Metrology Testbed [157,270–272] are already being developed to obtained as much data as possible from the metal PBF process in the interest of further bettering the process parameters and sensors required for optimum part quality. In combination with the tools that have already been developed, the current understanding of in-processing manufacturing events and their impact on the final parts quality can expand even further.

6.4 Concluding remarks

In this thesis, the design, development and testing of a high-resolution topographical measurement system has been presented for use as a layer-by-layer monitoring system in metal-PBF manufacturing systems. This measurement system uses FP with four camera-projector pairs to obtain a multi-view point cloud of the entire powder bed area. An out-

of-machine prototype has been designed based on the spatial limitations of a Renishaw AM250 L-PBF system and has been tested in three different hardware configurations throughout the development process. FBC algorithms have also been applied to the data collected from the system on a representative metal PBF sample to explore to possibility of using the multi-view FP system for automatic defect detection on in-process measurements of the powder bed. From the work that has been carried out, the following conclusions have been drawn:

- FP is a suitable method for acquiring full powder bed topographical measurements, while still capturing high frequency information such as small particles on the surface, at an acquisition rate that would not significantly impact manufacturing times (~1.1 s of image capture per measurement).
- Adopting a multi-view FP approach grants several benefits over a single camera-projector pairing including a higher lateral sampling, improved measurement accuracy, measurement redundancy and greater surface coverage while not impacting the acquisition rate due to simultaneous capture of the hour cameras. However, some issues have been observed with the data fusion approach applied, which allows for in-accurate and bad quality data from a single camera perspective to significantly impact the final multi-view point cloud, resulting in some measurement errors carrying forward.
- The multi-view FP system is able to accurately and repeatably measure high frequency information well enough that individual particles down to approximately 200 µm in lateral size can be detected by a FBC algorithm with substantial agreement against a higher resolution FV measurement of the same sample. This would allow for features ranging from 200 µm to 500 µm in lateral size such as larger pores, balling [25], and lattice deviations [26] to be reliably detected, while further improvements would be required to consistently detect sub 200 µm features such as weld tracks and unfused powder [25].

References

[1] ISO and ASTM 2015 52900: Standard Terminology for Additive Manufacturing – General Principles – Terminology *ISO/ASTM International* 1–9

[2] Bourell D, Kruth J P, Leu M, Levy G, Rosen D, Beese A M and Clare A 2017 Materials for additive manufacturing *CIRP Annals - Manufacturing Technology* **66** 659–81

[3] Renishaw Plc. Metal additive manufacturing 1 1–24

[4] Gibson I, Rosen D and Stucker B 2015 *Additive manufacturing technologies: 3D printing, rapid prototyping, and direct digital manufacturing* (Springer US)

[5] Huang Y, Leu M C, Mazumder J and Donmez A 2014 Additive Manufacturing: Current State, Future Potential, Gaps and Needs, and Recommendations *Journal of Manufacturing Science and Engineering* **137** 014001

[6] Baumers M, Holweg M and Rowley J 2016 The economics of 3D printing : A total cost perspective: *The enabling role of 3D Printing in redistributed manufacturing: a total cost model* 1–15

[7] Yim S and Rosen D 2012 Build Time and Cost Models for Additive Manufacturing Process Selection *Proceedings of the ASME 2012 International Design Engineering Technical Conferences & Computers and Information in Engineering Conference* 1–8

[8] Bornoff R, Parry J and Law C 2015 An Additive Design Heatsink Geometry Topology Identification and Optimisation Algorithm *2015 31st Thermal Measurement, Modeling & Management Symposium (SEMI-THERM)* 303–8

[9] Elmadih W, Syam W P, Maskery I, Chronopoulos D and Leach R 2019 Mechanical vibration bandgaps in surface-based lattices *Additive Manufacturing* **25** 421–9

[10] Sing S L, An J, Yeong W Y and Wiria F E 2016 Laser and electron-beam powder-bed additive manufacturing of metallic implants: A review on processes, materials and designs *Journal of Orthopaedic Research* **34** 369–85

[11] Gibson I, Rosen D and Stucker B 2015 *Additive manufacturing technologies: 3D printing, rapid prototyping, and direct digital manufacturing* (Springer Science+Business Media)

[12] Gao W, Haitjema H, Fang F Z, Leach R K, Cheung C F, Savio E and Linares J M 2019 On-machine and in-process surface metrology for precision manufacturing *CIRP Annals* **68** 843–66

[13] Leach R K, Bourell D, Carmignato S, Donmez A, Senin N and Dewulf W 2019 Geometrical metrology for metal additive manufacturing *CIRP Annals* **68** 677–700

[14] Bidare P, Maier R R J, Beck R J, Shephard J D and Moore A J 2017 An open-architecture metal powder bed fusion system for in-situ process measurements *Addit. Manuf.* **16** 177–85

[15] Leung C L A, Marussi S, Atwood R C, Towrie M, Withers P J and Lee P D 2018 In situ X-ray imaging of defect and molten pool dynamics in laser additive manufacturing *Nature Communications* **9** 1–9

[16] Zhao C, Fezzaa K, Cunningham R W, Wen H, De Carlo F, Chen L, Rollett A D and Sun T 2017 Real-time monitoring of laser powder bed fusion process using high-speed X-ray imaging and diffraction *Scientific Reports* **7** 1–11

[17] Frazier W E 2014 Metal Additive Manufacturing: A Review *J. of Materi Eng and Perform* **23** 1917–28

[18] Gibson I, Rosen D and Stucker B 2015 *Additive Manufacturing Technologies: 3D Printing, Rapid Prototyping, and Direct Digital Manufacturing* (New York: Springer-Verlag)

[19] Levy G N, Schindel R and Kruth J P 2003 RAPID MANUFACTURING AND RAPID TOOLING WITH LAYER MANUFACTURING (LM) TECHNOLOGIES, STATE OF THE ART AND FUTURE PERSPECTIVES *CIRP Annals* **52** 589–609

[20] Tapia G and Elwany A 2014 A Review on Process Monitoring and Control in Metal-Based Additive Manufacturing *Journal of Manufacturing Science and Engineering* **136**

[21] Mani M, Lane B M, Donmez M A, Feng S C, Moylan S P and Jr R R F 2015 Measurement science needs for real-time control of additive manufacturing powder bed fusion processes *NIST Pubs*

[22] Spears T G and Gold S A 2016 In-process sensing in selective laser melting (SLM) additive manufacturing *Integr Mater Manuf Innov* **5** 16–40

[23] Everton S K, Hirsch M, Stravroulakis P, Leach R K and Clare A T 2016 Review of in-situ process monitoring and in-situ metrology for metal additive manufacturing *Mater. Des.* **95** 431–45

[24] Grasso M and Colosimo B M 2017 Process defects and in situ monitoring methods in metal powder bed fusion: a review *Meas. Sci. Technol.* **28** 044005

[25] Li R, Liu J, Shi Y, Wang L and Jiang W 2012 Balling behavior of stainless steel and nickel powder during selective laser melting process *Int J Adv Manuf Technol* **59** 1025–35

[26] Echeta I, Feng X, Dutton B, Leach R and Piano S 2020 Review of defects in lattice structures manufactured by powder bed fusion *Int J Adv Manuf Technol* **106** 2649–68

[27] Grasso M, Remani A, Dickins A, Colosimo B M and Leach R K 2021 In-situ measurement and monitoring methods for metal powder bed fusion: an updated review *Meas. Sci. Technol.* **32** 112001

[28] Dickins A, Widjanarko T, Lawes S, Stavroulakis P and Leach R 2018 Design of a multi-sensor in-situ inspection system for additive manufacturing *ASPE/euspen Advancing Precision in Additive Manufacturing* ASPE/euspen Advancing Precision in Additive Manufacturing (Berkeley, CA, USA)

[29] Townsend A, Racasan R and Blunt L 2018 Surface-specific additive manufacturing test artefacts *Surf. Topogr.: Metrol. Prop.* **6** 024007

[30] Dickins A, Widjanarko T, Sims-Waterhouse D, Thompson A, Lawes S, Senin N, Senin N, Leach R and Leach R 2020 Multi-view fringe projection system for surface topography measurement during metal powder bed fusion *JOSAA* **37** B93–105

[31] Dickins A, Widjanarko T, Lawes S D A and Leach R 2019 Sensor fusion approach for in-situ measurement of metal laser powder bed fusion *Proc. Int. Symp. Solid Freeform Fabrication* (Austin, TX, USA)

[32] Leach R 2020 *Integrated metrology 10-year roadmap for advanced manufacturing* (Catapult High Value Manufacturing)

[33] Leach R and Carmignato S 2020 *Precision Metal Additive Manufacturing* (CRC Press)

[34] Grasso M, Gallina F and Colosimo B M 2018 Data fusion methods for statistical process monitoring and quality characterization in metal additive manufacturing *Procedia CIRP* **75** 103–7

[35] Steed C A, Halsey W, Dehoff R, Yoder S L, Paquit V and Powers S 2017 Falcon: Visual analysis of large, irregularly sampled, and multivariate time series data in additive manufacturing *Computers & Graphics* **63** 50–64

[36] Chandrasekar S, Coble J B, Yoder S, Nandwana P, Dehoff R R, Paquit V C and Babu S S 2020 Investigating the effect of metal powder recycling in electron beam powder bed fusion using process log data *Addit. Manuf.* **32** 100994

[37] Yoder S L, Morgan S, Kinzy C, Barnes E, Kirka M, Paquit V C, Nandwana P, Plotkowski A, Dehoff R R and Babu S S 2018 Characterization of topology optimized Ti-6Al-4V components using electron beam powder bed fusion *Addit. Manuf.* **19** 184–96

[38] Aminzadeh M and Kurfess T R 2019 Online quality inspection using Bayesian classification in powder-bed additive manufacturing from high-resolution visual camera images *J Intell Manuf* **30** 2505–23

[39] Lu Q Y, Nguyen N V, Hum A J W, Tran T and Wong C H 2020 Identification and evaluation of defects in selective laser melted 316L stainless steel parts via in-situ monitoring and micro computed tomography *Additive Manufacturing* **35** 101287

[40] Caltanissetta F, Grasso M, Petrò S and Colosimo B M 2018 Characterization of in-situ measurements based on layerwise imaging in laser powder bed fusion *Addit. Manuf.* **24** 183–99

[41] Kleszczynski S, zur Jacobsmuhlen J, Sehrt J T and Witt G 2012 Error detection in laser beam melting systems by high resolution imaging *Proceedings of the Solid Freeform Fabrication Symposium* Solid Freeform Fabrication Symposium (SFF) (Austin, TX, USA)

[42] zur Jacobsmuhlen J, Kleszczynski S, Schneider D and Witt G 2013 High resolution imaging for inspection of laser beam melting systems International Instrumentation and Measurement Technology Conference (I2MTC) (Minneapolis, MN, USA: IEEE) pp 707–12

[43] zur Jacobsmuhlen J, Witt G, Kleszczynski S and Merhof D 2015 Elevated region area measurement for quantitative analysis of laser beam melting process stability *Proceedings of the Solid Freeform Fabrication Symposium* Solid Freeform Fabrication Symposium (SFF) (Austin, TX, USA)

[44] zur Jacobsmühlen J, Achterhold J, Kleszczynski S, Witt G and Merhof D 2019 In situ measurement of part geometries in layer images from laser beam melting processes *Prog Addit Manuf* **4** 155–65

[45] Foster B K, Reutzel E W, Nassar A R, Hall B T, Brown S W and Dickman C J 2015 Optical, layerwise monitoring of powder bed fusion *In Solid Free. Fabr. Symp. Proc* pp 295–307

[46] Gobert C, Reutzel E W, Petrich J, Nassar A R and Phoha S 2018 Application of supervised machine learning for defect detection during metallic powder bed fusion additive manufacturing using high resolution imaging. *Addit. Manuf.* **21** 517–28

[47] Abdelrahman M, Reutzel E W, Nassar A R and Starr T L 2017 Flaw detection in powder bed fusion using optical imaging *Additive Manufacturing* **15** 1–11

[48] Pagani L, Grasso M, Scott P J and Colosimo B M 2020 Automated layerwise detection of geometrical distortions in laser powder bed fusion *Addit. Manuf.* **36** 101435

[49] Scime L, Siddel D, Baird S and Paquit V 2020 Layer-wise anomaly detection and classification for powder bed additive manufacturing processes: A machine-agnostic algorithm for real-time pixel-wise semantic segmentation *Additive Manufacturing* **36** 101453

[50] Scime L and Beuth J 2018 A multi-scale convolutional neural network for autonomous anomaly detection and classification in a laser powder bed fusion additive manufacturing process *Addit. Manuf.* **24** 273–86

[51] Scime L and Beuth J 2018 Anomaly detection and classification in a laser powder bed additive manufacturing process using a trained computer vision algorithm *Additive Manufacturing* **19** 114–26

[52] Mahmoudi M, Ezzat A A and Elwany A 2019 Layerwise anomaly detection in laser powder-bed fusion metal additive manufacturing *J. Manuf. Sci. Eng.* **141** 031002

[53] Bamberg J, Zenzinger G and Ladewig A 2016 In-Process Control of Selective Laser Melting by Quantitative Optical Tomography 19th World Conference on Non-Destructive Testing (Munich, Germany)

[54] Schwerdtfeger J, Singer R F and Körner C 2012 In situ flaw detection by IR-imaging during electron beam melting *Rapid Prototyping Journal* **18** 259–63

[55] Yoder S L, Nandwana P, Paquit V C, Kirka M, Scopel A, Dehoff R R and Babu S S 2019 Approach to qualification using E-PBF in-situ process monitoring in Ti-6Al-4V *Addit. Manuf.* **28** 98–106

[56] Nandwana P, Kirka M M, Paquit V C, Yoder S and Dehoff R R 2018 Correlations between powder feedstock quality, in situ porosity detection, and fatigue behavior of Ti-6Al-4V fabricated by powder bed electron beam melting: a step towards qualification *JOM* **70** 1686–91

[57] Ridwan S, Mireles J, Gaytan S M, Espalin D and Wicker R B 2014 Automatic layerwise acquisition of thermal and geometric data of the electron beam melting process using infrared thermography *Proc. Int. Symp. Solid Freeform Fabrication* vol 343 (Austin, TX, USA)

[58] Rodriguez E, Medina F, Espalin D, Terrazas C A, Muse D, Henry C, MacDonald E and Wicker R B 2012 Integration of a thermal imaging feedback control system in electron beam melting Solid Freeform Frabication Symposium (Austin, TX, USA) pp 945–61

[59] Zhang B, Ziegert J, Farahi F and Davies A 2016 In situ surface topography of laser powder bed fusion using fringe projection *Addit. Manuf.* **12** 100–7

[60] Zhang B, Ziegert C J and Angela D 2016 In situ surface metrology of laser powder bed fusion using fringe projection 2016 Summer Topical Meeting Dimensional Accuracy and Surface Finish in Additive Manufacturing (Raleigh, NC, USA)

[61] Land W S, Zhang B, Ziegert J and Davies A 2015 In-situ metrology system for laser powder bed fusion additive process *Procedia Manuf.* **1** 393–403

[62] Zhang B, Land W S, Ziegert J and Davies A 2015 In situ monitoring of laser powder bed fusion additive manufacturing using digital fringe projection technique

Proceedings: ASPE 2015 Spring Topical Meeting ASPE Spring Topical Meeting: Achieving Precision Tolerances in Additive Manufacturing (North Carolina State University Raleigh, NC, USA)

[63] Kalms M, Narita R, Thomy C, Vollertsen F and Bergmann R B 2019 New approach to evaluate 3D laser printed parts in powder bed fusion-based additive manufacturing in-line within closed space *Additive Manufacturing* **26** 161–5

[64] Liu Y, Zhang Z, Blunt L, Saunby G, Dawes J, Blackham B, Rahman H A, Smith C, Gao F and Jiang X 2019 In-situ inspection system for additive manufacturing based on phase measurement profilometry *European Society for Precision Engineering and Nanotechnology, Conference Proceedings - 19th International Conference and Exhibition, EUSPEN 2019* 19th International Conference of the European Society for Precision Engineering and Nanotechnology (euspen) pp 324–7

[65] Liu Y, Blunt L, Zhang Z, Rahman H A, Gao F and Jiang X 2020 In-situ areal inspection of powder bed for electron beam fusion system based on fringe projection profilometry *Addit. Manuf.* **31** 100940

[66] Tan Phuc L and Seita M 2019 A high-resolution and large field-of-view scanner for in-line characterization of powder bed defects during additive manufacturing *Mater. Des.* **164** 107562

[67] Barrett C, MacDonald E, Conner B and Persi F 2018 Micron-level layer-wise surface profilometry to detect porosity defects in powder bed fusion of Inconel 718 *JOM* **70** 1844–52

[68] Fleming T G, Nestor S G L, Allen T R, Boukhaled M A, Smith N J and Fraser J M 2020 Tracking and controlling the morphology evolution of 3D powder-bed fusion in situ using inline coherent imaging *Additive Manufacturing* **32** 100978

[69] DePond P J, Guss G, Ly S, Calta N P, Deane D, Khairallah S and Matthews M J 2018 In situ measurements of layer roughness during laser powder bed fusion additive manufacturing using low coherence scanning interferometry *Mater. Des.* **154** 347–59

[70] Wong H, Garrard R, Black K, Fox P and Sutcliffe C 2020 Material characterisation using electronic imaging for Electron Beam Melting process monitoring *Manufacturing Letters* **23** 44–8

[71] Wong H, Neary D, Jones E, Fox P and Sutcliffe C 2019 Pilot capability evaluation of a feedback electronic imaging system prototype for in-process monitoring in electron beam additive manufacturing *Int. J. Adv. Manuf. Technol.* **100** 707–20

[72] Wong H, Neary D, Jones E, Fox P and Sutcliffe C 2019 Benchmarking spatial resolution in electronic imaging for potential in-situ Electron Beam Melting monitoring *Additive Manufacturing* **29** 100829

[73] Alldredge J, Slotwinski J, Storck S, Kim S, Goldberg A and Montalbano T 2018 In-situ monitoring and modeling of metal additive manufacturing powder bed fusion *AIP Conference Proceedings 1949* 44th Annual Review of Progress in Quantitative Nondestructive Evaluation vol 1 (Provo, UT, USA) p 020007

[74] Arnold C, Böhm J and Körner C 2019 In operando monitoring by analysis of backscattered electrons during electron beam melting *Adv. Eng. Mater.* 1901102

[75] Pobel C R, Arnold C, Osmanlic F, Fu Z and Körner C 2019 Immediate development of processing windows for selective electron beam melting using layerwise monitoring via backscattered electron detection *Materials Letters* **249** 70–2

[76] Lane B, Moylan S, Whitenton E P and Ma L 2016 Thermographic measurements of the commercial laser powder bed fusion process at NIST *Rapid Prototyping Journal* **22** 778–87

[77] Kleszczynski S, zur Jacobsmuhlen J, Rienarz B, Sehrt J T, Gerd W and Merhof D 2014 Improving process stability of laser beam melting systems *DDMC 2014, Fraunhofer Direct Digital Manufacturing Conference. Proceedings* Fraunhofer Direct Digital Manufacturing Conference (Berlin, Germany)

[78] Angelone R, Caggiano A, Teti R, Spierings A, Staub A and Wegener K 2020 Bio-Intelligent Selective Laser Melting System based on Convolutional Neural Networks for In-Process Fault Identification *Procedia CIRP* **88** 612–7

[79] Imani F, Chen R, Diewald E, Reutzel E and Yang H 2019 Deep learning of variant geometry in layerwise imaging profiles for additive manufacturing quality control *J. Manuf. Sci. Eng* **141** 111001

[80] Imani F, Chen R, Diewald E, Reutzel E and Yang H 2019 Image-guided variant geometry analysis of layerwise build quality in additive manufacturing *ASME 2019 14th International Manufacturing Science and Engineering Conference* 14th International Manufacturing Science and Engineering Conference (Erie, PA, USA: American Society of Mechanical Engineers Digital Collection)

[81] Grasso M, Valsecchi G and Colosimo B M 2020 Powder bed irregularity and hot-spot detection in electron beam melting by means of in-situ video imaging *Manuf. Lett.* **24** 47–51

[82] Gaikwad A, Imani F, Rao P, Yang H and Reutzel E 2019 Design Rules and In-Situ Quality Monitoring of Thin-Wall Features Made Using Laser Powder Bed Fusion ASME 2019 14th International Manufacturing Science and Engineering Conference (American Society of Mechanical Engineers Digital Collection)

[83] He P, Zhong K, Liu X, Zhou G, Wang C, Wei Q, Shi Y and Li Z 2019 A phase-guided method for extracting the contour of the fusion area in laser powder bed fusion *Seventh International Conference on Optical and Photonic Engineering (icOPEN 2019)* Seventh International Conference on Optical and Photonic

Engineering (icOPEN 2019) vol 11205 (International Society for Optics and Photonics) p 112051H

[84] Mireles J, Terrazas C, Gaytan S M, Roberson D A and Wicker R B 2015 Closed-loop automatic feedback control in electron beam melting *Int. J. Adv. Manuf. Technol.* **78** 1193–9

[85] Erler M, Streek A, Schulze C and Exner H 2014 Novel Machine and Measurement Concept for Micro Machining by Selective Laser Sintering International Solid Freeform Fabrication Symposium (Austin, TX, USA)

[86] Neef A, Seyda V, Herzog D, Emmelmann C, Schönleber M and Kogel-Hollacher M 2014 Low coherence interferometry in selective laser melting *Phys. Procedia* **56** 82–9

[87] Wong H 2020 Bitmap generation from computer-aided design for potential layer-quality evaluation in electron beam additive manufacturing *Rapid Prototyping Journal* **26** 941–50

[88] Ali A and Farson D 2002 Statistical Classification of Spectral Data for Laser Weld Quality Monitoring *Journal of Manufacturing Science and Engineering* **124** 323–5

[89] Williams R J, Piglione A, Rønneberg T, Jones C, Pham M-S, Davies C M and Hooper P A 2019 In situ thermography for laser powder bed fusion: Effects of layer temperature on porosity, microstructure and mechanical properties *Additive Manufacturing* **30** 100880

[90] Montazeri M and Rao P 2018 Sensor-Based Build Condition Monitoring in Laser Powder Bed Fusion Additive Manufacturing Process Using a Spectral Graph Theoretic Approach *Journal of Manufacturing Science and Engineering* **140** 091002

[91] Gaikwad A, Yavari R, Montazeri M, Cole K, Bian L and Rao P 2020 Toward the digital twin of additive manufacturing: Integrating thermal simulations, sensing, and analytics to detect process faults *IISE Transactions* **52** 1204–17

[92] Heigel J C, Lane B M and Levine L E 2020 In situ measurements of melt-pool length and cooling rate during 3D builds of the metal AM-bench artifacts *Integr. Mater. Manuf. Innov.* **9** 31–53

[93] Heigel J C, Lane B, Levine L, Phan T and Whiting J 2020 In situ thermography of the metal bridge structures fabricated for the 2018 additive manufacturing benchmark test series (AM-bench 2018) *J. RES. NATL. INST. STAN.* **125** 125005

[94] Lough C S, Escano L I, Qu M, Smith C C, Landers R G, Bristow D A, Chen L and Kinzel E C 2020 In-situ optical emission spectroscopy of selective laser melting *Journal of Manufacturing Processes* **53** 336–41

[95] Lough C S, Wang X, Smith C C, Landers R G, Bristow D A, Drallmeier J A, Brown B and Kinzel E C 2020 Correlation of SWIR imaging with LPBF 304L stainless steel part properties *Additive Manufacturing* **35** 101359

[96] Bartlett J L, Heim F M, Murty Y V and Li X 2018 In situ defect detection in selective laser melting via full-field infrared thermography *Addit. Manuf.* **24** 595–605

[97] Jalalahmadi B, Liu J, Rios J, Science S, Slotwinski J and Lab J H U A P 2019 In-process Defect Monitoring and Correction in Additive Manufacturing of Aluminum Alloys AHS International Forum 75 (AHS International)

[98] Plotnikov Y, Henkel D, Burdick J, French A, Sions J and Bourne K 2019 Infrared-assisted acoustic emission process monitoring for additive manufacturing *AIP Conference Proceedings* **2102** 020006

[99] Foster S J, Carver K, Dinwiddie R B, List III F, Unocic K A, Chaudhary A and Babu S S 2018 Process-defect-structure-property correlations during laser powder bed fusion of alloy 718: role of in situ and ex situ characterizations *Metall. Mater. Trans. A Phys. Metall. Mater. Sci.* **49** 5775–98

[100] Mohr G, Altenburg S J, Ulbricht A, Heinrich P, Baum D, Maierhofer C and Hilgenberg K 2020 In-situ defect detection in laser powder bed fusion by using thermography and optical tomography—comparison to computed tomography *Metals* **10** 103

[101] Paulson N H, Gould B, Wolff S J, Stan M and Greco A C 2020 Correlations between thermal history and keyhole porosity in laser powder bed fusion *Additive Manufacturing* **34** 101213

[102] Dinwiddie R B, Dehoff R R, Lloyd P D, Lowe L E and Ulrich J B 2013 Thermographic in-situ process monitoring of the electron-beam melting technology used in additive manufacturing *Thermosense: Thermal Infrared Applications XXXV* Thermosense: Thermal Infrared Applications XXXV vol 8705 (International Society for Optics and Photonics) p 87050K

[103] Rodriguez E, Mireles J, Terrazas C A, Espalin D, Perez M A and Wicker R B 2015 Approximation of absolute surface temperature measurements of powder bed fusion additive manufacturing technology using in situ infrared thermography *Addit. Manuf.* **5** 31–9

[104] Cordero P M, Mireles J, Ridwan S and Wicker R B 2017 Evaluation of monitoring methods for electron beam melting powder bed fusion additive manufacturing technology *Prog Addit Manuf* **2** 1–10

[105] Raplee J, Plotkowski A, Kirka M M, Dinwiddie R, Okello A, Dehoff R R and Babu S S 2017 Thermographic Microstructure Monitoring in Electron Beam Additive Manufacturing *Sci Rep* **7** 43554

[106] Dehoff R R, Kirka M M, Ellis E, Paquit V C, Nandwana P and Plotkowski A J 2019 *Electron Beam Melting Technology Improvements*

[107] Price S, Lydon J, Cooper K and Chou K 2015 Temperature Measurements in Powder-Bed Electron Beam Additive Manufacturing ASME 2014 International Mechanical Engineering Congress and Exposition (American Society of Mechanical Engineers Digital Collection)

[108] Grasso M and Colosimo B M 2019 A statistical learning method for image-based monitoring of the plume signature in laser powder bed fusion *Robot. Com-Int. Manuf.* **57** 103–15

[109] Yan H, Grasso M, Paynabar K and Colosimo B M 2020 Real-time Detection of Clustered Events in Video-imaging data with Applications to Additive Manufacturing *arXiv:2004.10977 [cs, stat]*

[110] Lee Y S, Kirka M M, Dinwiddie R B, Raghavan N, Turner J, Dehoff R R and Babu S S 2018 Role of scan strategies on thermal gradient and solidification rate in electron beam powder bed fusion *Additive Manufacturing* **22** 516–27

[111] Gong X, Cheng B, Price S and Chou K 2013 Powder-bed electron-beam-melting additive manufacturing: Powder characterization, process simulation and metrology 2013 ASME Early Career Technical Conference (ECTC) vol District F, Section 2 (Birmingham, AL, USA) pp 59–66

[112] Boone N, Zhu C, Smith C, Todd I and Willmott J R 2018 Thermal near infrared monitoring system for electron beam melting with emissivity tracking *Additive Manufacturing* **22** 601–5

[113] Price S, Cooper K and Chou K 2012 Evaluations of temperature measurements by near-infrared thermography in powder-based electron-beam additive manufacturing *Proceedings of the Solid Freeform Fabrication Symposium* Solid Freeform Fabrication Symposium (Austin, TX, USA) p 13

[114] Price S, Cooper K and Chou K 2014 Evaluations of temperature measurements in powder-based electron beam additive manufacturing by near-infrared thermography *IJRAPIDM* **4** 1

[115] Anwar A B and Pham Q-C 2018 Study of the spatter distribution on the powder bed during selective laser melting *Additive Manufacturing* **22** 86–97

[116] Bidare P, Bitharas I, Ward M G, Attallah M M and Moore A J 2018 Fluid and particle dynamics in laser powder bed fusion *Acta Mater.* **142** 107–20

[117] Yin J, Wang D, Yang L, Wei H, Dong P, Ke L, Wang G, Zhu H and Zeng X 2020 Correlation between forming quality and spatter dynamics in laser powder bed fusion *Additive Manufacturing* **31** 100958

[118] Tan Z, Fang Q, Li H, Liu S, Zhu W and Yang D 2020 Neural network based image segmentation for spatter extraction during laser-based powder bed fusion processing *Optics & Laser Technology* **130** 106347

[119] Barrett C, Carradero C, Harris E, Rogers K, MacDonald E and Conner B 2019 Statistical analysis of spatter velocity with high-speed stereovision in laser powder bed fusion *Prog. Addit. Manuf.* **4** 423–30

[120] Guo Q, Zhao C, Escano L I, Young Z, Xiong L, Fezzaa K, Everhart W, Brown B, Sun T and Chen L 2018 Transient dynamics of powder spattering in laser powder bed fusion additive manufacturing process revealed by in-situ high-speed high-energy x-ray imaging *Acta Materialia* **151** 169–80

[121] Repossini G, Laguzza V, Grasso M and Colosimo B M 2017 On the use of spatter signature for in-situ monitoring of laser powder bed fusion *Addit. Manuf.* **16** 35–48

[122] Eschner E, Staudt T and Schmidt M 2020 Correlation of spatter behavior and process zone formation in powder bed fusion of metals *CIRP Annals* **69** 209–12

[123] Eschner E, Staudt T and Schmidt M 2019 3D particle tracking velocimetry for the determination of temporally resolved particle trajectories within laser powder bed fusion of metals *Int. J. Extrem. Manuf.* **1** 035002

[124] Barrett C, Carradero C, Harris E, Mcknight J, Walker J, Macdonald E and Conner B 2018 Low cost , high speed stereovision for spatter tracking in laser powder bed fusion *Proceedings of the Solid Freeform Fabrication Symposium* Solid Freeform Fabrication (SFF) (Austin, TX, USA) pp 2122–34

[125] Zheng Y, Zhang X, Wang S, Li Q, Qin H and Li B 2020 Similarity evaluation of topography measurement results by different optical metrology technologies for additive manufactured parts *Opt. Laser Eng.* **126** 105920

[126] Zhang Y, Fuh J Y H, Ye D and Hong G S 2019 In-situ monitoring of laser-based PBF via off-axis vision and image processing approaches *Addit. Manuf.* **25** 263–74

[127] Ye D, Zhu K, Fuh J Y H, Zhang Y and Soon H G 2019 The investigation of plume and spatter signatures on melted states in selective laser melting *Optics & Laser Technology* **111** 395–406

[128] Taheri Andani M, Dehghani R, Karamooz-Ravari M R, Mirzaeifar R and Ni J 2018 A study on the effect of energy input on spatter particles creation during selective laser melting process *Addit. Manuf.* **20** 33–43

[129] Grasso M, Demir A G, Previtali B and Colosimo B M 2018 In situ monitoring of selective laser melting of zinc powder via infrared imaging of the process plume *Robot. Com-Int. Manuf.* **49** 229–39

[130] Young Z A, Guo Q, Parab N D, Zhao C, Qu M, Escano L I, Fezzaa K, Everhart W, Sun T and Chen L 2020 Types of spatter and their features and formation mechanisms in laser powder bed fusion additive manufacturing process *Additive Manufacturing* **36** 101438

[131] Leung C L A, Marussi S, Towrie M, Atwood R C, Withers P J and Lee P D 2019 The effect of powder oxidation on defect formation in laser additive manufacturing *Acta Materialia* **166** 294–305

[132] Zhao C, Fezzaa K, Cunningham R W, Wen H, De Carlo F, Chen L, Rollett A D and Sun T 2017 Real-time monitoring of laser powder bed fusion process using high-speed X-ray imaging and diffraction *Sci. Rep.* **7** 1–11

[133] Wasmer K, Le-Quang T, Meylan B and Shevchik S A 2019 In situ quality monitoring in am using acoustic emission: a reinforcement learning approach *J. Mater. Eng.* **28** 666–72

[134] Shevchik S A, Masinelli G, Kenel C, Leinenbach C and Wasmer K 2019 Deep Learning for In Situ and Real-Time Quality Monitoring in Additive Manufacturing Using Acoustic Emission *IEEE Transactions on Industrial Informatics* **15** 5194–203

[135] Ye D, Hong G S, Zhang Y, Zhu K and Fuh J Y H 2018 Defect detection in selective laser melting technology by acoustic signals with deep belief networks *Int. J. Adv. Manuf. Technol.* **96** 2791–801

[136] Kouprianoff D, Luwes N, Yadroitsava I and Yadroitsev I 2018 Acoustic Emission Technique for Online Detection of Fusion Defects for Single Tracks during Metal Laser Powder Bed Fusion *Proceedings of the 29th Annual International Solid Freeform Fabrication Symposium* (Austin, TX, USA)

[137] Mitchell J A, Ivanoff T A, Dagel D, Madison J D and Jared B 2020 Linking pyrometry to porosity in additively manufactured metals *Additive Manufacturing* **31** 100946

[138] Hooper P A 2018 Melt pool temperature and cooling rates in laser powder bed fusion *Additive Manufacturing* **22** 548–59

[139] Forien J-B, Calta N P, DePond P J, Guss G M, Roehling T T and Matthews M J 2020 Detecting keyhole pore defects and monitoring process signatures during laser powder bed fusion: A correlation between in situ pyrometry and ex situ X-ray radiography *Addit. Manuf.* **35** 101336

[140] Renken V, von Freyberg A, Schünemann K, Pastors F and Fischer A 2019 In-process closed-loop control for stabilising the melt pool temperature in selective laser melting *Prog. Addit. Manuf.* **4** 411–21

[141] Yang Z, Lu Y, Yeung H and Krishnamurty S 2019 Investigation of deep learning for real-time melt pool classification in additive manufacturing *15th International*

Conference on Automation Science and Engineering (CASE) 15th International Conference on Automation Science and Engineering (CASE) (Vancouver, BC, Canada: IEEE) pp 640–7

[142] Demir A G, De Giorgi C and Previtali B 2018 Design and implementation of a multisensor coaxial monitoring system with correction strategies for selective laser melting of a maraging steel *J. Manuf. Sci. Eng* **140** 041003

[143] Clijsters S, Craeghs T, Buls S, Kempen K and Kruth J-P 2014 In situ quality control of the selective laser melting process using a high-speed, real-time melt pool monitoring system *Int J Adv Manuf Technol* **75** 1089–101

[144] Craeghs T, Clijsters S, Yasa E, Bechmann F, Berumen S and Kruth J-P 2011 Determination of geometrical factors in Layerwise Laser Melting using optical process monitoring *Opt. Laser Eng.* **49** 1440–6

[145] Berumen S, Bechmann F, Lindner S, Kruth J-P and Craeghs T 2010 Quality control of laser- and powder bed-based Additive Manufacturing (AM) technologies *Physics Procedia* **5**

[146] Doubenskaia M, Pavlov M, Grigoriev S N, Tikhonova E and Smurov I 2012 Comprehensive Optical Monitoring of Selective Laser Melting *J. Laser Micro Nanoen.* **7** 236–43

[147] Pavlov M, Doubenskaia M and Smurov I 2010 Pyrometric analysis of thermal processes in SLM technology *Physics Procedia* **5** 523–31

[148] Jayasinghe S, Paoletti P, Sutcliffe C, Dardis J, Jones N and Green P 2020 Automatic Quality Assessments of Laser Powder Bed Fusion Builds from Photodiode Sensor Measurements

[149] Okaro I A, Jayasinghe S, Sutcliffe C, Black K, Paoletti P and Green P L 2019 Automatic fault detection for laser powder-bed fusion using semi-supervised machine learning *Addit. Manuf.* **27** 42–53

[150] Alberts D, Schwarze D and Witt G 2017 In situ melt pool monitoring and the correlation to part density of inconel® 718 for quality assurance in selective laser meltin *Proc. Int. Symp. Solid Freeform Fabrication* p 14

[151] Nadipalli V K, Andersen S A, Nielsen J S and Pedersen D B 2019 Considerations for interpreting in-situ photodiode sensor data in pulsed mode laser powder bed fusion *Proceedings of the Joint Special Interest Group meeting between euspen and ASPE Advancing Precision in Additive Manufacturing (2019)* Joint Special Interest Group meeting between euspen and ASPE Advancing Precision in Additive Manufacturing (The European Society for Precision Engineering and Nanotechnology) pp 66–9

[152] Bisht M, Ray N, Verbist F and Coeck S 2018 Correlation of selective laser melting-melt pool events with the tensile properties of Ti-6Al-4V ELI processed by laser powder bed fusion *Addit. Manuf.* **22** 302–6

[153] Kolb T, Elahi R, Seeger J, Soris M, Scheitler C, Hentschel O, Tremel J and Schmidt M 2020 Camera signal dependencies within coaxial melt pool monitoring in laser powder bed fusion *Rapid Prototyp. J.* **26** 100–6

[154] Vasileska E, Demir A G, Colosimo B M and Previtali B 2020 Layer-wise control of selective laser melting by means of inline melt pool area measurements *Journal of Laser Applications* **32** 022057

[155] Demir A G, Mazzoleni L, Caprio L, Pacher M and Previtali B 2019 Complementary use of pulsed and continuous wave emission modes to stabilize melt pool geometry in laser powder bed fusion *Optics & Laser Technology* **113** 15–26

[156] Fisher B A, Lane B, Yeung H and Beuth J 2018 Toward determining melt pool quality metrics via coaxial monitoring in laser powder bed fusion *Manufacturing Letters* **15** 119–21

[157] Lane B and Yeung H 2019 Process Monitoring Dataset from the Additive Manufacturing Metrology Testbed (AMMT): "Three-Dimensional Scan Strategies" *J. RES. NATL. INST. STAN.* **124** 124033

[158] Craeghs T, Bechmann F, Berumen S and Kruth J-P 2010 Feedback control of layerwise laser melting using optical sensors *Phys. Procedia* **5** 505–14

[159] Craeghs T, Clijsters S, Kruth Jean-P, Bechmann F and Ebert Marie-C 2012 Detection of process failures in layerwise laser melting with optical process monitoring *Phys. Procedia* **39** 753–9

[160] Zhirnov I, Mekhontsev S, Lane B, Grantham S and Bura N 2020 Accurate determination of laser spot position during laser powder bed fusion process thermography *Manufacturing Letters* **23** 49–52

[161] Lane B, Heigel J, Ricker R, Zhirnov I, Khromschenko V, Weaver J, Phan T, Stoudt M, Mekhontsev S and Levine L 2020 Measurements of melt pool geometry and cooling rates of individual laser traces on IN625 bare plates *Integr Mater Manuf Innov* **9** 16–30

[162] Scime L and Beuth J 2019 Melt pool geometry and morphology variability for the Inconel 718 alloy in a laser powder bed fusion additive manufacturing process *Additive Manufacturing* **29** 100830

[163] Bruna-Rosso C, Demir A G and Previtali B 2018 Selective laser melting finite element modeling: Validation with high-speed imaging and lack of fusion defects prediction *Materials & Design* **156** 143–53

[164] Yuan B, Giera B, Guss G, Matthews I and McMains S 2019 Semi-Supervised Convolutional Neural Networks for In-Situ Video Monitoring of Selective Laser Melting *2019 IEEE Winter Conference on Applications of Computer Vision (WACV)*

[165] Kanko J A, Sibley A P and Fraser J M 2016 In situ morphology-based defect detection of selective laser melting through inline coherent imaging *J. Mater. Process Technol.* **231** 488–500

[166] Schmeiser F, Krohmer E, Schell N, Uhlmann E and Reimers W 2020 Experimental observation of stress formation during selective laser melting using in situ X-ray diffraction *Additive Manufacturing* **32** 101028

[167] Uhlmann E, Krohmer E, Hohlstein F and Reimers W 2017 Development of an experimental test setup for in situ strain evaluation during selective laser melting *Proc. Int. Symp. Solid Freeform Fabrication* (Austin, TX, USA) p 9

[168] Calta N P, Wang J, Kiss A M, Martin A A, Depond P J, Guss G M, Thampy V, Fong A Y, Weker J N, Stone K H, Tassone C J, Kramer M J, Toney M F, Van Buuren A and Matthews M J 2018 An instrument for in situ time-resolved X-ray imaging and diffraction of laser powder bed fusion additive manufacturing processes *Rev. Sci.* **89** 055101

[169] Lhuissier P, Bataillon X, Maestre C, Sijobert J, Cabrol E, Bertrand P, Boller E, Rack A, Blandin J-J, Salvo L and Martin G 2020 In situ 3D X-ray microtomography of laser-based powder-bed fusion (L-PBF)—A feasibility study *Additive Manufacturing* **34** 101271

[170] Hehr A, Norfolk M, Kominsky D, Boulanger A, Davis M and Boulware P 2020 Smart Build-Plate for Metal Additive Manufacturing Processes *Sensors* **20** 360

[171] Dunbar A J, Denlinger E R, Gouge M F and Michaleris P 2016 Experimental validation of finite element modeling for laser powder bed fusion deformation *Addit. Manuf.* **12** 108–20

[172] Guo Q, Zhao C, Qu M, Xiong L, Escano L I, Hojjatzadeh S M H, Parab N D, Fezzaa K, Everhart W, Sun T and Chen L 2019 In-situ characterization and quantification of melt pool variation under constant input energy density in laser powder bed fusion additive manufacturing process *Additive Manufacturing* **28** 600–9

[173] Rieder H, Dillhoefer A, Spies M, Bamberg J and Hess T 2014 Online monitoring of additive manufacturing processes using ultrasound European Conference on Non-Destructive Testing (ECNDT) (Prague, Czech Republic)

[174] Rieder H, Spies M, Bamberg J and Henkel B 2016 On-and offline ultrasonic inspection of additively manufactured components World Conference on Non-Destructive Testing (Munich, Germany)

[175] Gold S A and Spears T G 2018 Acoustic monitoring method for additive manufacturing processes

[176] Scott S P and Sutcliffe C 2015 Additive manufacturing apparatus and method

[177] Eschner N, Weiser L, Häfner B and Lanza G 2020 Classification of specimen density in laser powder bed fusion (l-pbf) using in-process structure-borne acoustic process emissions *Addit. Manuf.* **34** 101324

[178] Lu Q Y, Nguyen N V, Hum A J W, Tran T and Wong C H 2019 Optical in-situ monitoring and correlation of density and mechanical properties of stainless steel parts produced by selective laser melting process based on varied energy density *Journal of Materials Processing Technology* **271** 520–31

[179] Montazeri M, Nassar A R, Dunbar A J and Rao P 2020 In-process monitoring of porosity in additive manufacturing using optical emission spectroscopy *IISE Trans.* **52**

[180] Yang D, Li H, Liu S, Song C, Yang Y, Shen S, Lu J, Liu Z and Zhu Y 2020 In situ capture of spatter signature of SLM process using maximum entropy double threshold image processing method based on genetic algorithm *Optics & Laser Technology* **131** 106371

[181] Zheng H, Li H, Lang L, Gong S and Ge Y 2018 Effects of scan speed on vapor plume behavior and spatter generation in laser powder bed fusion additive manufacturing *J. Manuf.* **36** 60–7

[182] Leung C L A, Marussi S, Atwood R C, Towrie M, Withers P J and Lee P D 2018 In situ X-ray imaging of defect and molten pool dynamics in laser additive manufacturing *Nat. Commun.* **9** 1355

[183] Kwon O, Kim H G, Ham M J, Kim W, Kim G-H, Cho J-H, Kim N I and Kim K 2018 A deep neural network for classification of melt-pool images in metal additive manufacturing *J. Intell. Manuf.* **31** 375–86

[184] Martin A A, Calta N P, Hammons J A, Khairallah S A, Nielsen M H, Shuttlesworth R M, Sinclair N, Matthews M J, Jeffries J R, Willey T M and Lee J R I 2019 Ultrafast dynamics of laser-metal interactions in additive manufacturing alloys captured by in situ X-ray imaging *Materials Today Advances* **1** 100002

[185] Bobel A, Hector L G, Chelladurai I, Sachdev A K, Brown T, Poling W A, Kubic R, Gould B, Zhao C, Parab N, Greco A and Sun T 2019 In situ synchrotron X-ray imaging of 4140 steel laser powder bed fusion *Materialia* **6** 100306

[186] Ye D, Hsi Fuh J Y, Zhang Y, Hong G S and Zhu K 2018 In situ monitoring of selective laser melting using plume and spatter signatures by deep belief networks *ISA Trans.* **81** 96–104

[187] Zhang Y, Hong G S, Ye D, Zhu K and Fuh J Y H 2018 Extraction and evaluation of melt pool, plume and spatter information for powder-bed fusion AM process monitoring *Mater. Des.* **156** 458–69

[188] Zhang Y, Soon H G, Ye D, Fuh J Y H and Zhu K 2019 Powder-bed fusion process monitoring by machine vision with hybrid convolutional neural networks *IEEE Trans. Ind. Informat.* **16** 5769–79

[189] Lough C S, Wang X, Landers R G, Bristow D A and Kinzel E C 2019 In-Situ Local Part Qualification of SLM 304L Stainless Steel through Voxel based Processing of SWIR Imaging Data *Proceedings of the 30th Annual Solid Freeform Fabrication Symposium (2019, Austin, TX)* Solid Freeform Fabrication Symposium (Austin, TX, USA)

[190] Colosimo B M and Grasso M 2020 Chapter 13: On-machine measurement, monitoring and control, in Precision Metal Additive Manufacturing *Precision Metal Additive Manufacturing* (Boca Raton, FL: CRC Press)

[191] Colosimo B M and Grasso M 2018 Spatially weighted PCA for monitoring video image data with application to additive manufacturing *Journal of Quality Technology* **50** 391–417

[192] Ye Z, Liu C, Tian W and Kan C 2020 A deep learning approach for the identification of small process shifts in additive manufacturing using 3D point clouds *Proc. Manuf.* **48** 770–5

[193] Li Z, Liu X, Wen S, He P, Zhong K, Wei Q, Shi Y and Liu S 2018 In situ 3D monitoring of geometric signatures in the powder-bed-fusion additive manufacturing process via vision sensing methods *Sensors* **18** 1180

[194] Southon N, Stavroulakis P, Goodridge R and Leach R 2018 In-process measurement and monitoring of a polymer laser sintering powder bed with fringe projection *Mater. Des.* **157** 227–34

[195] Everton S K, Hirsch M, Stavroulakis P I, Leach R K and Clare A T 2016 Review of in-situ process monitoring and in-situ metrology for metal additive manufacturing *Materials and Design* **95** 431–45

[196] Zhang B 2017 *In situ fringe projection profilometry for laser power bed fusion process* (Charlotte, NC, USA: The University of North Carolina at Charlotte)

[197] Liu Y, Zhang Z, Blunt L, Saunby G, Dawes J, Blackham B, Rahman H A, Smith C, Gao F and Jiang X 2018 In-situ areal inspection of powder bed for electron beam fusion AM system based on fringe projection *Proceedings - 2018 ASPE and euspen Summer Topical Meeting: Advancing Precision in Additive Manufacturing* ASPE and euspen Summer Topical Meeting on Advancing Precision in Additive Manufacturing (Berkeley, CA, USA) pp 259–64

[198] Nguyen H, Nguyen D, Wang Z, Kieu H and Le M 2015 Real-time, high-accuracy 3D imaging and shape measurement *Appl. Opt., AO* **54** A9–17

[199] Jiang C, Jia S, Dong J, Bao Q, Yang J, Lian Q and Li D 2015 Multi-frequency color-marked fringe projection profilometry for fast 3D shape measurement of complex objects *Opt. Express, OE* **23** 24152–62

[200] Zhang S 2018 High-speed 3D shape measurement with structured light methods: A review *Optics and Lasers in Engineering* **106** 119–31

[201] Stavroulakis P I and Leach R K 2016 Invited Review Article: Review of post-process optical form metrology for industrial-grade metal additive manufactured parts *Review of Scientific Instruments* **87** 041101

[202] Pawley J B 2006 Points, Pixels, and Gray Levels: Digitizing Image Data *Handbook Of Biological Confocal Microscopy* ed J B Pawley (Boston, MA: Springer US) pp 59–79

[203] Song L, Gao Y, Zhu X, Guo Q and Xi J 2016 A 3D measurement method based on multi-view fringe projection by using a turntable *Optoelectron. Lett.* **12** 389–94

[204] Ernst R, Weckenmann A and Velgan R 2003 *Local Wall Thickness Measurement of Formed Sheet Metal Using Fringe Projection Technique*

[205] Genovese K and Pappalettere C 2006 Whole 3D shape reconstruction of vascular segments under pressure via fringe projection techniques *Optics and Lasers in Engineering* **44** 1311–23

[206] Du H, Chen X, Xi J, Yu C and Zhao B 2017 Development and Verification of a Novel Robot-Integrated Fringe Projection 3D Scanning System for Large-Scale Metrology *Sensors* **17** 2886

[207] Rao R M, Radhakrishna D and S U 2018 Development of a Robot-mounted 3D Scanner and Multi-view Registration Techniques for Industrial Applications *Procedia Computer Science* **133** 256–67

[208] Wang M, Yin Y, Deng D, Meng X, Liu X and Peng X 2017 Improved performance of multi-view fringe projection 3D microscopy *Opt. Express, OE* **25** 19408–21

[209] Shaheen A, Sims-Waterhouse D, Bointon P, Piano S and Leach R 2019 Automated characterisation of multi-view fringe projection system for three- dimensional measurement of additively manufactured parts euspen/ASPE Advancing Precision in Additive Manufacturing (Nantes, France)

[210] Gdeisat M, Qudeisat M, AlSaʹd M, Burton D, Lilley F and Ammous M M M 2016 Simple and accurate empirical absolute volume calibration of a multi-sensor fringe projection system *Optics and Lasers in Engineering* **80** 32–44

[211] Land W S, Zhang B, Ziegert J and Davies A 2015 In-Situ Metrology System for Laser Powder Bed Fusion Additive Process *Procedia Manufacturing* **1** 393–403

[212] Zhang B, Ziegert J, Farahi F and Davies A 2016 In situ surface topography of laser powder bed fusion using fringe projection *Additive Manufacturing* **12** 100–7

[213] Li Z, Liu X, Wen S, He P, Zhong K, Wei Q, Shi Y and Liu S 2018 In Situ 3D Monitoring of Geometric Signatures in the Powder-Bed-Fusion Additive Manufacturing Process via Vision Sensing Methods *Sensors (Basel)* **18**

[214] Southon N, Stavroulakis P, Goodridge R and Leach R 2018 In-process measurement and monitoring of a polymer laser sintering powder bed with fringe projection *Materials & Design* **157** 227–34

[215] Liu Y, Zhang Z, Blunt L, Saunby G, Dawes J, Blackham B, Rahman H A, Smith C, Gao F and Jiang X 2018 In-situ areal inspection of powder bed for electron beam fusion AM system based on fringe projection *Proceedings - 2018 ASPE and euspen Summer Topical Meeting: Advancing Precision in Additive Manufacturing* (American Society for Precision Engineering, ASPE) pp 259–64

[216] Liu Y, Blunt L, Zhang Z, Rahman H A, Gao F and Jiang X 2020 In-situ areal inspection of powder bed for electron beam fusion system based on fringe projection profilometry *Additive Manufacturing* **31** 100940

[217] Newton L, Senin N, Smith B, Chatzivagiannis E and Leach R K 2019 Comparison and validation of topography segmentation methods for feature-based characterisation of metal powder bed fusion surfaces *Surface Topography: Metrology and Properties* **Submitted** 3–7

[218] Lou S, Jiang X, Sun W, Zeng W, Pagani L and Scott P J 2019 Characterisation methods for powder bed fusion processed surface topography *Precision Engineering* **57** 1–15

[219] Senin N, Thompson A and Leach R 2018 Feature-based characterisation of signature topography in laser powder bed fusion of metals *Meas. Sci. Technol.* **29** 045009

[220] Lou S, Pagani L, Zeng W, Jiang X and Scott P J 2020 Watershed segmentation of topographical features on freeform surfaces and its application to additively manufactured surfaces *Precision Engineering* **63** 177–86

[221] Zhang S 2016 *High-speed 3D imaging with digital fringe projection techniques* (CRC Press)

[222] Shaheen A, Sims-Waterhouse D, Bointon P, Piano S and Leach R K 2019 Automated characterisation of multi-view fringe projection system for three-dimensional measurement of additively manufactured parts *Conference Proc. Euspen/ASPE Advancing Precision in Additive Manufacturing* (Nantes, France)

[223] Istvan D 2019 digiCamControl

[224] MathWorks 2020 MATLAB

[225] Helmi F 2011 Focus Variation Instruments *Optical Measurement of Surface Topography* ed R K Leach (Berlin Heidelberg: Springer-Verlag)

[226] Giusca C L, Claverley J D, Sun W, Leach R K, Helmli F and Chavigner M P J 2014 Practical estimation of measurement noise and flatness deviation on focus variation microscopes *CIRP Annals* **63** 545–8

[227] Alburayt A, Syam W P and Leach R 2018 Lateral scale calibration for focus variation microscopy *Meas. Sci. Technol.* **29** 065012

[228] Girardeau-Montaut D 2019 *CloudCompare*

[229] InnovMetric Software 2019 *Polyworks|Inspector™ 2019 IR2 64-bit (build 2869)*

[230] Newton L, Senin N, Smith B, Chatzivagiannis E and Leach R 2019 Comparison and validation of surface topography segmentation methods for feature-based characterisation of metal powder bed fusion surfaces *Surf. Topogr.: Metrol. Prop.* **7** 045020

[231] Besl P J and McKay N D 1992 A method for registration of 3-D shapes *IEEE Transactions on Pattern Analysis and Machine Intelligence* **14** 239–56

[232] Zhang Z 1994 Iterative point matching for registration of free-form curves and surfaces *Int J Comput Vision* **13** 119–52

[233] Tsung-Pao Fang and Piegl L A 1995 Delaunay triangulation in three dimensions *IEEE Computer Graphics and Applications* **15** 62–9

[234] Thompson A, Senin N, Giusca C and Leach R 2017 Topography of selectively laser melted surfaces: A comparison of different measurement methods *CIRP Annals* **66** 543–6

[235] Senin N, Thompson A and Leach R K 2017 Characterisation of the topography of metal additive surface features with different measurement technologies *Meas. Sci. Technol.* **28** 095003

[236] Pastre M-A de, Thompson A, Quinsat Y, Albajez J A, Senin N and Leach R K 2020 Polymer powder bed fusion surface texture measurement *Meas. Sci. Technol.* **31**

[237] Everton S K, Hirsch M, Stravroulakis P, Leach R K and Clare A T 2016 Review of in-situ process monitoring and in-situ metrology for metal additive manufacturing *Materials & Design* **95** 431–45

[238] Bell S 2013 *Measurement Good Practice Guide No. 11 (Issue 2)* (National Physical Laboratory)

[239] Digital Surf 2019 *MountainsMap® Premium v7.4.9053*

[240] Newton L, Senin N, Gomez C, Danzl R, Helmli F, Blunt L and Leach R 2019 Areal topography measurement of metal additive surfaces using focus variation microscopy *Additive Manufacturing* **25** 365–89

[241] Baumgartl H, Tomas J, Buettner R and Merkel M 2020 A deep learning-based model for defect detection in laser-powder bed fusion using in-situ thermographic monitoring *Prog. Addit. Manuf.* **5** 277–85

[242] Senin N and Blunt L 2013 Characterisation of individual areal features *Characterisation of Areal Surface Texture* ed R Leach (Springer-Verlag Berlin Heidelberg) pp 179–216

[243] Jiang X, Senin N, Scott P J and Blateyron F 2021 Feature-based characterisation of surface topography and its application *CIRP Annals* **70** 681–702

[244] Lou S, Jiang X, Sun W, Zeng W, Pagani L and Scott P J 2019 Characterisation methods for powder bed fusion processed surface topography *Precis. Eng.* **57** 1–15

[245] Newton L, Senin N, Chatzivagiannis E, Smith B and Leach R 2020 Feature-based characterisation of Ti6Al4V electron beam powder bed fusion surfaces fabricated at different surface orientations *Additive Manufacturing* **35** 101273

[246] Liu Y, Yang Y, Mai S, Wang D and Song C 2015 Investigation into spatter behavior during selective laser melting of AISI 316L stainless steel powder *Mater. Des.* **87** 797–806

[247] Newton L, Senin N, Gomez C, Danzl R, Helmli F, Blunt L and Leach R 2019 Areal topography measurement of metal additive surfaces using focus variation microscopy *Addit. Manuf.* **25** 365–89

[248] InnovMetric Software 2019 Polyworks|Inspector^{TM} 2019

[249] Wang Y and Zhang S 2013 Optimal fringe angle selection for digital fringe projection technique *Appl. Opt., AO* **52** 7094–8

[250] Colosimo B M, Grossi E, Caltanissetta F and Grasso M 2020 Penelope: A Novel Prototype for In Situ Defect Removal in LPBF *JOM* **72** 1332–9

[251] Girardeau-Montaut D 2019 CloudCompare

[252] Weber C, Hahmann S and Hagen H 2011 Methods for Feature Detection in Point Clouds *Visualization of Large and Unstructured Data Sets - Applications in Geospatial Planning, Modeling and Engineering (IRTG 1131 Workshop)* OpenAccess Series in Informatics (OASIcs) vol 19, ed A Middel, I Scheler and H Hagen (Dagstuhl, Germany: Schloss Dagstuhl–Leibniz-Zentrum fuer Informatik) pp 90–9

[253] Weber C, Hahmann S and Hagen H 2010 Sharp Feature Detection in Point Clouds *SMI 2010 - Shape Modeling International Conference* (Aix-en-Provence, France: IEEE) pp 175–86

[254] Zeybek M and Şanlıoğlu İ 2019 Point cloud filtering on UAV based point cloud *Measurement* **133** 99–111

[255] Wang X, Zhang X, Ren X, Li L, Feng H, He Y, Chen H and Chen X 2020 Point cloud 3D parent surface reconstruction and weld seam feature extraction for robotic grinding path planning *Int J Adv Manuf Technol* **107** 827–41

[256] Yang Y, Fang H, Fang Y and Shi S 2020 Three-dimensional point cloud data subtle feature extraction algorithm for laser scanning measurement of large-scale irregular surface in reverse engineering *Measurement* **151** 107220

[257] Zhang J, Zhao X, Chen Z and Lu Z 2019 A Review of Deep Learning-Based Semantic Segmentation for Point Cloud *IEEE Access* **7** 179118–33

[258] Bello S A, Yu S, Wang C, Adam J M and Li J 2020 Review: Deep Learning on 3D Point Clouds *Remote Sensing* **12** 1729

[259] Landrieu L and Simonovsky M 2018 Large-Scale Point Cloud Semantic Segmentation With Superpoint Graphs Proceedings of the IEEE Conference on Computer Vision and Pattern Recognition pp 4558–67

[260] Yang B, Luo W and Urtasun R 2018 PIXOR: Real-Time 3D Object Detection From Point Clouds Proceedings of the IEEE Conference on Computer Vision and Pattern Recognition pp 7652–60

[261] Remani A, Williams R, Thompson A, Dardis J, Jones N, Hooper P and Leach R 2021 Design of a multi-sensor measurement system for in-situ defect identification in metal additive manufacturing *Proc. euspen/ASPE Advancing Precision in Additive Manufacturing* euspen/ASPE Advancing Precision in Additive Manufacturing (Virtual)

[262] Taraz Metrology 2021 Measurement systems *Taraz Metrology*

[263] Druzgalski C L, Ashby A, Guss G, King W E, Roehling T T and Matthews M J 2020 Process optimization of complex geometries using feed forward control for laser powder bed fusion additive manufacturing *Additive Manufacturing* **34** 101169

[264] Wang Q, Michaleris P (Pan), Nassar A R, Irwin J E, Ren Y and Stutzman C B 2020 Model-based feedforward control of laser powder bed fusion additive manufacturing *Additive Manufacturing* **31** 100985

[265] Yeung H and Lane B 2020 A residual heat compensation based scan strategy for powder bed fusion additive manufacturing *Manufacturing Letters* **25** 56–9

[266] Kruth J-P, Mercelis P, Van Vaerenbergh J and Craeghs T 20070901 Feedback control of selective laser melting *Proceedings of the 3rd International Conference on Advanced Research in Virtual and Rapid Prototyping* (TAYLOR & FRANCIS LTD) pp 521–7

[267] Heeling T and Wegener K 2018 The effect of multi-beam strategies on selective laser melting of stainless steel 316L *Additive Manufacturing* **22** 334–42

[268] Demir A G and Previtali B 2017 Additive manufacturing of cardiovascular CoCr stents by selective laser melting *Materials & Design* **119** 338–50

[269] Mireles J, Ridwan S, Morton P A, Hinojos A and Wicker R B 2015 Analysis and correction of defects within parts fabricated using powder bed fusion technology *Surf. Topogr.: Metrol. Prop.* **3** 034002

[270] Lane B M, Mekhontsev S, Grantham S E, Vlasea M, Whiting J G, Yeung H, Fox J C, Zarobila C J, Neira J E, McGlauflin M L, Hanssen L M, Moylan S P, Donmez M A and Rice J P 2016 Design, developments, and results from the NIST additive manufacturing metrology testbed (AMMT) *Proceedings of the Solid Freeform Fabrication Symposium* Solid Freeform Fabrication Symposium (SFF) (Austin, TX, USA)

[271] Lane B M, Grantham S E, Yeung H, Zarobila C J and Fox J C 2017 Performance characterization of process monitoring sensors on the NIST Additive Manufacturing Metrology Testbed *Proceedings of the Solid Freeform Fabrication Symposium* Solid Freeform Fabrication Symposium (SFF) (Austin, TX, USA)

[272] Yeung H, Hutchinson K and Lin D 2021 Design and Implementation of Laser Powder Bed Fusion Additive Manufacturing Testbed Control Software (University of Texas at Austin)

Appendix A

A.1 Deviation maps from measurements in chapter 5

This appendix presents deviation maps the multi-view and all single-view fringe projection datasets relative to the FV measurement. These deviation maps are from the data used in chapter 5 of the thesis.

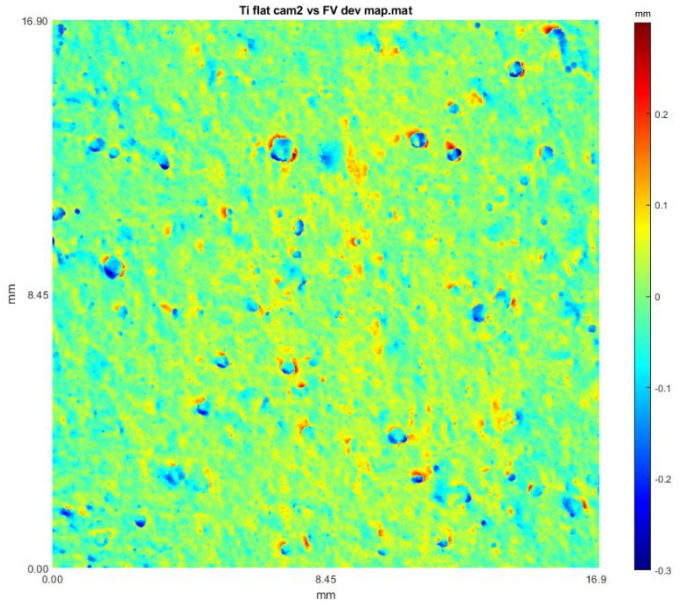

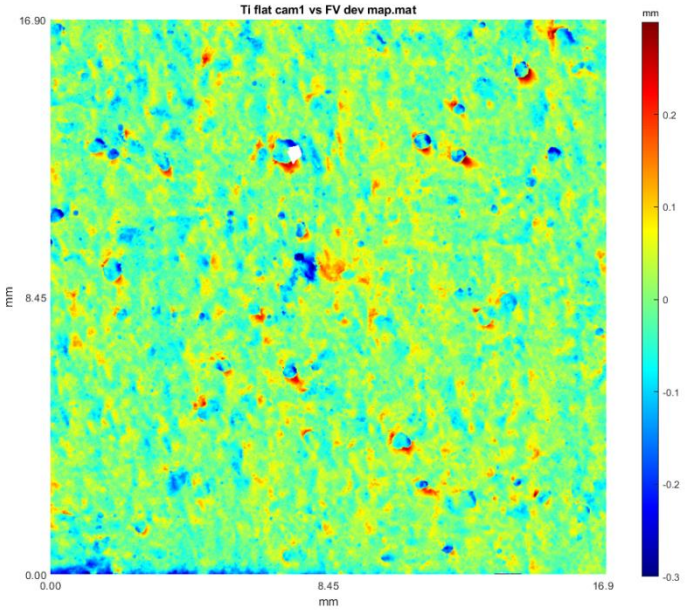

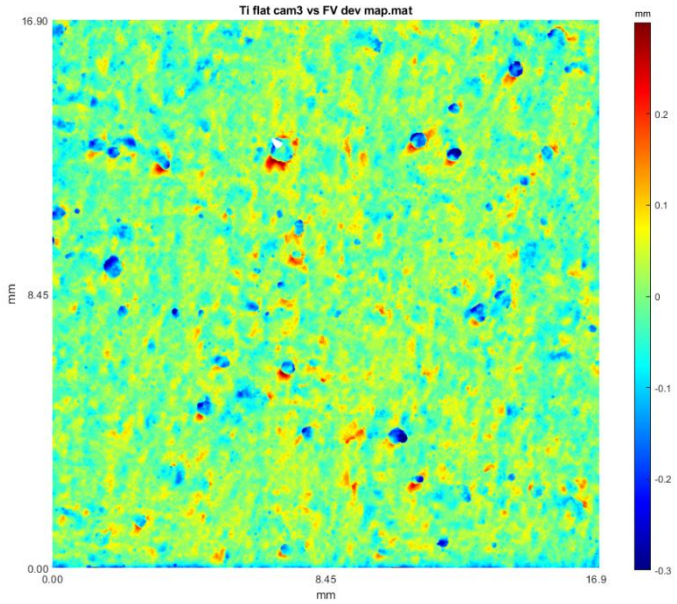
Ti flat cam3 vs FV dev map.mat
16.90
8.45
0.00
mm
0.00
8.45
16.9
mm
mm
0.2
0.1
0
-0.1
-0.2
-0.3

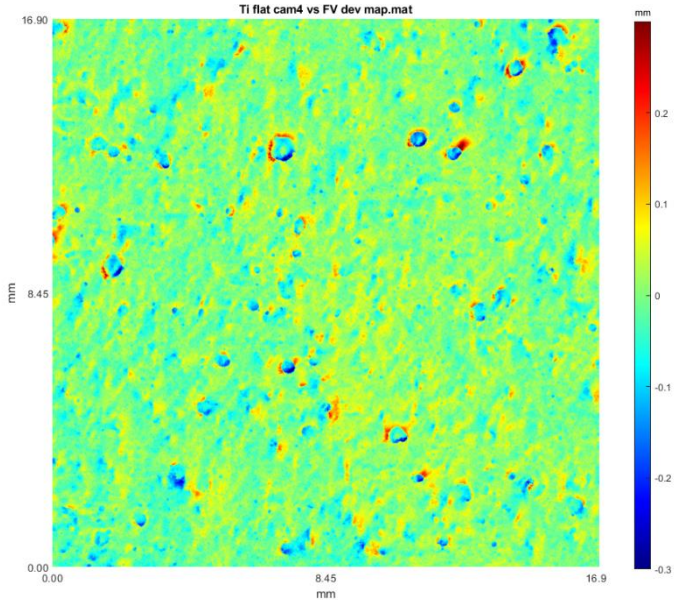
Ti flat cam4 vs FV dev map.mat
16.90
8.45
0.00
mm
0.00
8.45
16.9
mm
mm
0.2
0.1
0
-0.1
-0.2
-0.3

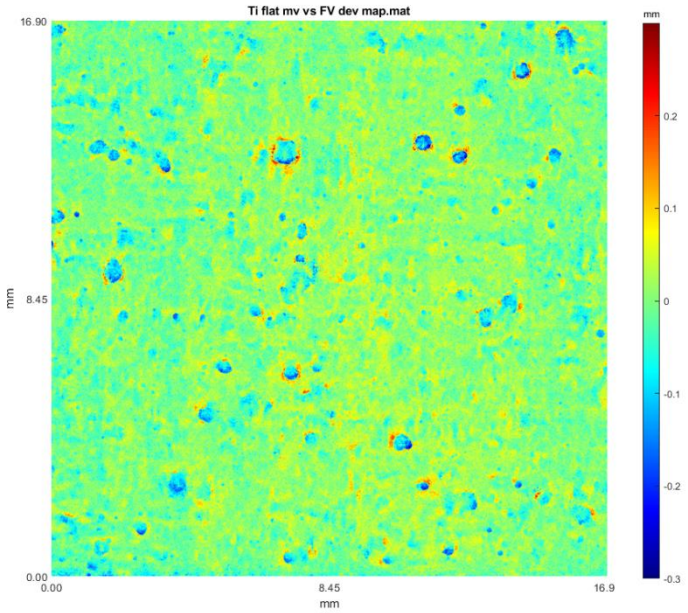
Ti flat mv vs FV dev map.mat
16.90
8.45
0.00
mm
0.00
8.45
16.9
mm
mm
0.2
0.1
0
-0.1
-0.2
-0.3

A.2 FBC detection maps from measurements in chapter 5

This appendix presents the FBC particle detection maps for the FV, multi-view and all single-view fringe projection datasets. These FBC detections maps are from the data used in chapter 5 of the thesis.

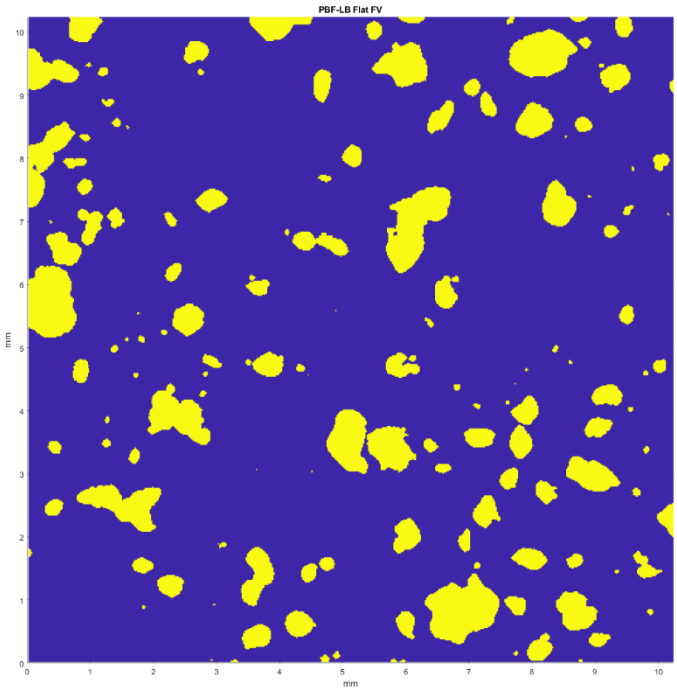

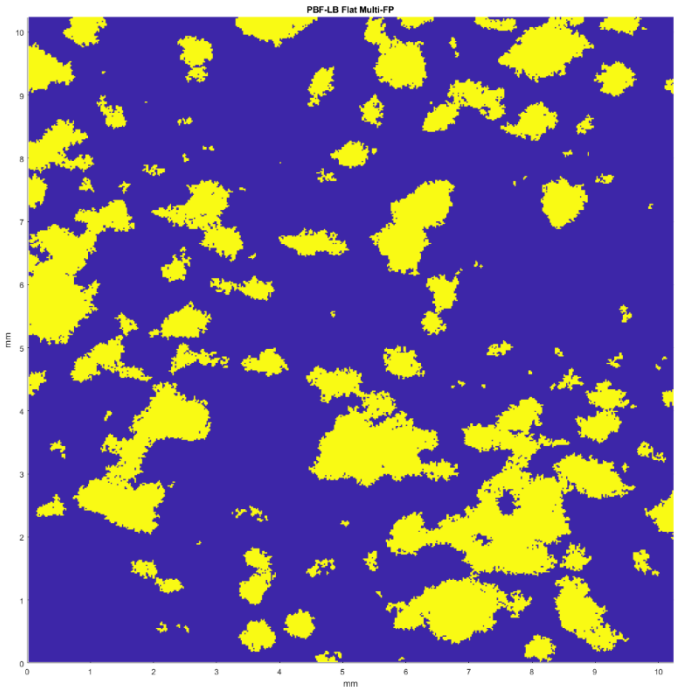

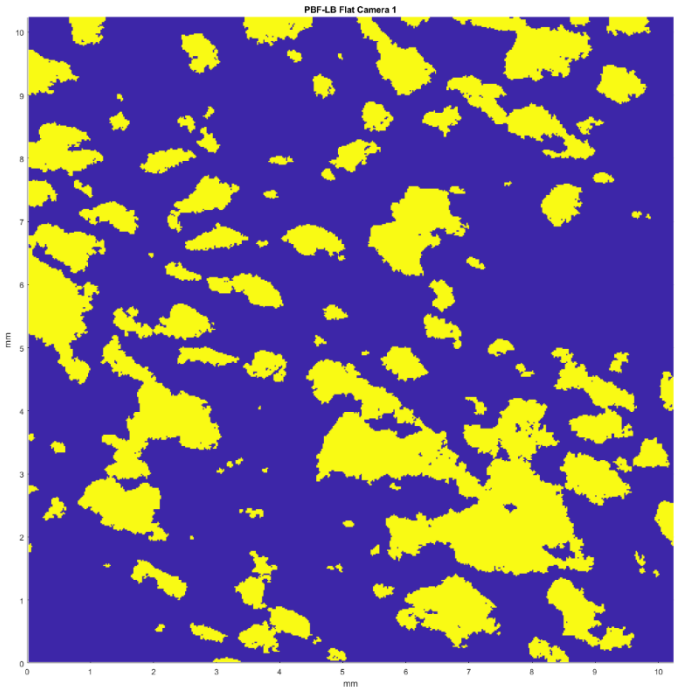
PBF-LB Flat Camera 1
mm
mm

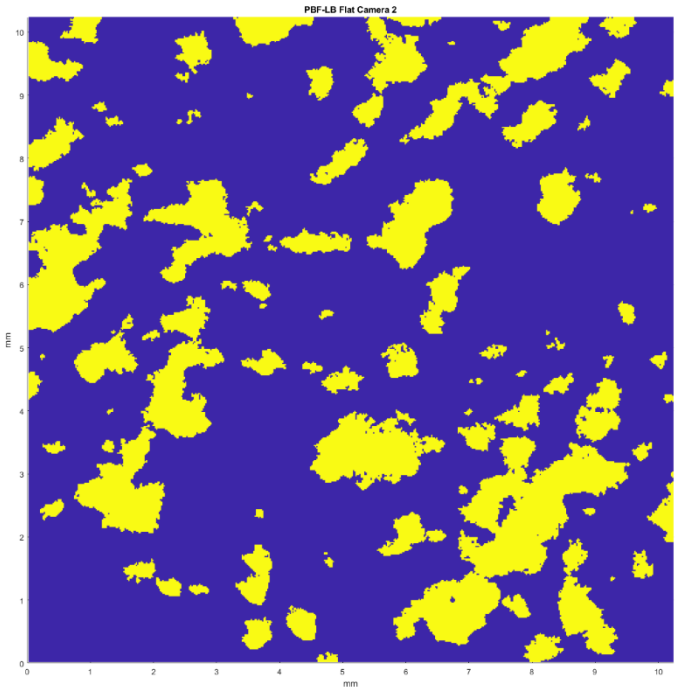
PBF-LB Flat Camera 2
mm
mm

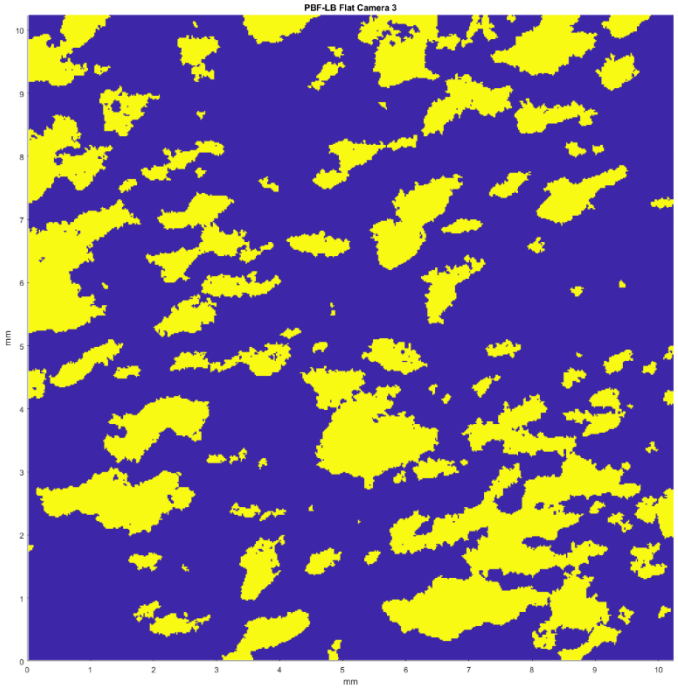
PBF-LB Flat Camera 3
mm
mm

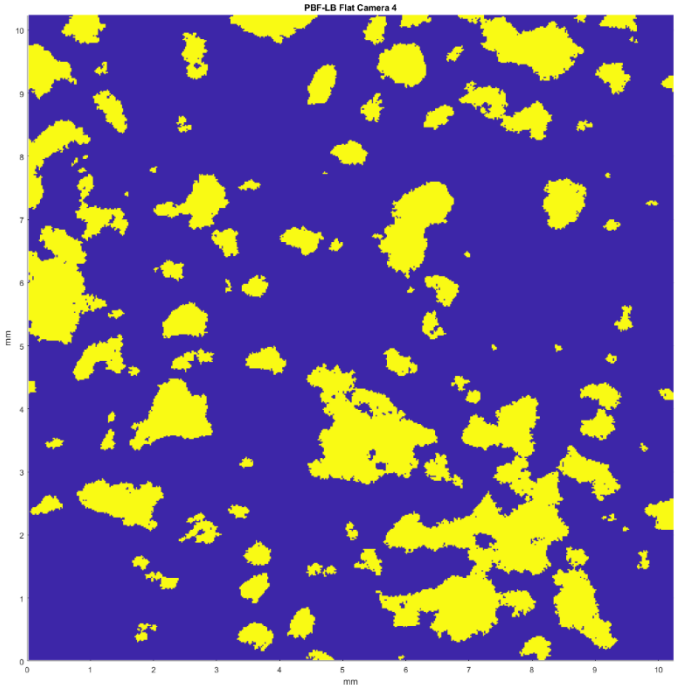
PBF-LB Flat Camera 4
mm
mm